

Chemical effects of magnetic nanoparticles on heavy metal removal

Diana Salah Raie Ahmed

A thesis submitted for the degree of

Doctor of Philosophy

Physics and Astronomy Department

October 2022

Mami, I did it!

Dadi, Rest in peace!



Declaration

I, Diana Salah Raie Ahmed, confirm that the work presented in this thesis is my own. Where information has been derived from other sources, I confirm that this has been indicated in the thesis.

Abstract

The safe removal of hexavalent chromium (Cr⁶⁺) from waste streams is in increasing demand because of environmental, economic and health considerations. The integrated adsorption and bio-reduction method can eliminate the carcinogenic Cr⁶⁺ and detoxify Cr⁶⁺ to the less toxic trivalent state (Cr³⁺). This work describes a synthetic protocol for achieving the best chemical composition of spherical and flower-like manganese ferrite (Mn_xFe_{3-x}O₄) nanostructures (NS) for Cr⁶⁺ adsorption. NS, with the highest adsorption performance, was selected to study its efficiency in the extracellular reduction of Cr⁶⁺ to Cr³⁺ by Shewanella oneidensis (S. oneidensis) MR-1. Mn_xFe_{3-x}O₄ NS were prepared by a polyol solvothermal synthesis process. They were characterised by powder X-Ray Diffraction, Transmission Electron Microscopy, X-ray Photoelectron Spectrometry (XPS), Dynamic Light Scattering and Fourier Transform-Infrared Spectroscopy. Inductively Coupled Plasma Atomic Emission Spectroscopy evaluated the elemental composition of Mn_xFe_{3-x}O₄ NS. Our results revealed that the oxidation state of the manganese precursor significantly affects the Cr^{6+} adsorption efficiency of Mn_xFe_{3-} $_xO_4$ NS. The best adsorption capacity for Cr^{6+} is 16.8 ± 1.6 mg Cr^{6+}/g by the spherical $Mn_{0.2}^{2+}Fe_{2.8}^{3+}O_4$ NPs at pH 7, which was 1.4 times higher than that by $Mn_{0.8}^{3+}Fe_{2.2}^{3+}O_4$ nanoflowers. A chemical redox reaction took place between the adsorbent surface of $Mn_{0.2}^{2+}Fe_{2.8}^{3+}O_4$ NPs and Cr^{6+} solution as was approved by XPS. The redox-based interaction was attributed to the relative excess of divalent manganese in $Mn_{0.2}^{2+}Fe_{2.8}^{3+}O_4$ NPs based on our XPS analysis. The lethal concentration of Cr⁶⁺ for S. oneidensis MR-1 was 60 mg/L. $Mn_{0.2}^{2+}Fe_{2.8}^{3+}O_4$ NPs improved the viability of S. oneidensis MR-1 by 3.3

times at the sub-lethal dose of Cr^{6+} (50 mg/L). The addition of $Mn_{0.2}^{2+}Fe_{2.8}^{3+}O_4$ NPs to *S. oneidensis* MR-1 enhanced Cr^{6+} bio-removal by 2.66 times compared to using bacteria alone and by 1.37 times of applying $Mn_{0.2}^{2+}Fe_{2.8}^{3+}O_4$ NPs. To gain insights into the enhancing impact of $Mn_{0.2}^{2+}Fe_{2.8}^{3+}O_4$ NPs on the microbial reduction of Cr^{6+} by *S. oneidensis* MR-1, the change of the morphology of *S. oneidensis* MR-1 cells in response to their treatment with a sub-lethal dose of Cr^{6+} was monitored using Scanning Electron Microscopy. The oxidation state of Cr was studied using XPS, which revealed that integrating both *S. oneidensis* MR-1 and $Mn_{0.2}^{2+}Fe_{2.8}^{3+}O_4$ NPs boosted the detoxification of the removed Cr^{6+} by 2.1 times by using *S. oneidensis* MR-1 alone and by 1.4 times by applying $Mn_{0.2}^{2+}Fe_{2.8}^{3+}O_4$ NPs alone. This has opened up a new route for research using nanomaterials for enhancing the bio-reduction of more Cr^{6+} using bacteria. This work provides a cost-effective method for Cr^{6+} removal with less Cr-containing sludge.

Impact statement

The carcinogenic hexavalent chromium (Cr⁶⁺) can leak from industrial effluents into the surface and groundwater. Also, mining activities are reasons for the contamination of water resources and soil. Such pollution occurs because of improper waste management and causes severe problems in developing countries. The contamination of drinking and irrigation water supplies by Cr⁶⁺ has been a leading cause of death for several years.

The present work aims to use manganese ferrite ($Mn_xFe_{3-x}O_4$) nanostructures (NS) to enhance the bio-detoxification of Cr^{6+} to a less toxic trivalent state (Cr^{3+}). *S. oneidensis* MR-1 bacteria are selected for the bio-reduction of Cr^{6+} . The contribution of this research was the evidence for the impact of chemical composition (doping level and oxidation state of Mn) and synthesis conditions (temperature and time) of $Mn_xFe_{3-x}O_4$ NS on the adsorption capacity of NS for Cr^{6+} .

The output of this study is crucial not only for finding the chemical composition of NS that showed the highest adsorption capacity for Cr^{6+} but also for minimising the doping level in $Mn_xFe_{3-x}O_4$ NS and identifying the best synthesis conditions will decrease the cost of NS production.

In this thesis, the integrated adsorption bio-reduction method improved the recovery of Cr⁶⁺ from water 2.66 times by using bacteria alone. Integrating both *S. oneidensis* MR-1 and nanoparticles boosted the detoxification of the removed Cr⁶⁺ by 2.1 times by using *S. oneidensis* MR-1 alone and by 1.4 NS alone. The present findings will

highlight the opportunities for research using nanomaterials for boosting the bioreduction of Cr^{6+} and other toxic heavy metals using bacteria.

This integrated technology is easy to use, cost-effective, and accessible for low-and middle-income countries. Most Cr-based industries, such as steel, metallurgy, plating, battery and tanning, are localised in developing countries. In emerging economies, the locations of some such high-polluting factories are very near the farms. Combining adsorption and bio-reduction can offer a potential method for managing Cr⁶⁺ removal from contaminated industrial effluents and sites where access to innovative technology, water or electric supplies is limited.

The remediation of the Cr-containing industrial effluents and the highly contaminated area around the mining sites create an opportunity for reusing the detoxified Cr as recycled resources. The treated water can be re-circulated in the same industry to save surface water. The productivity of crops, either quality or quantity, will be improved due to the limited concentration of heavy metals in irrigation water. More job opportunities will be created, which will have a positive effect on the national income and economy.

The findings in this PhD project provided a promising solution for an easy, fast and cheap technique for safely removing Cr⁶⁺ from wastewater by combining adsorption and bio-reduction. Onsite treatment of industrial effluents created an opportunity for reusing the treated wastewater in the same plant. Recycling the resources will reduce the consumption of surface water and the cost of manufacturing and stop the leakage of Cr⁶⁺ into the environment.¹

Preventing the outflow of pollutants from the industry into the environment reduces the risk of contaminating the soil, surface and underground water bodies with Cr^{6+} . Hence, the limited exposure of agriculture, farms, animals and humans to Cr^{6+} will reduce the pollution and health problems caused by Cr^{6+} . The presented approach allows for opportunities to impregnate waste with certain bacteria to improve bioremediation.

The practicality and cost-effectiveness of integrating nano-scaled materials and biological treatment for wastewater remediation attract attention. Furthermore, applying integrated adsorption and bio-reduction shows potential for removing heavy metals from many industries. This perspective will progressively affect productivity and the economy due to saving people healthcare and resources such as water, energy, and metals. The overall outcomes of this research will be published in peer-reviewed journals and presented as posters at conferences.

Publications, summer schools and awards

Publications

Articles

Diana S. Raie, Ioannis Tsonas, Melisa Canales, Stefanos Mourdikoudis, Konstantinos Simeonidis, Antonis Makridis, Dimitrios Karfaridis, Shanom Ali, Georgios Vourlias, Peter Wilson, Laurent Bozec, Lena Ciric, Nguyen T. K. Thanh. Enhanced detoxification of Cr⁶⁺ by *Shewanella oneidensis* via adsorption on spherical and flower-like manganese ferrite nanostructures. **Submitted in Nanoscale Advances**

Diana S. Raie, Ioannis Tsonas, Stefanos Mourdikoudis, Evangelia Delli, George Vourlias,
Lena Ciric, Nguyen T. K. Thanh. Safe removal of Cr⁶⁺ by manganese ferrite
nanoparticles and *Shewanella oneidensis*: A redox-based reaction. **In**preparation

Posters

<u>Diana S. Raie</u>, Ioannis Tsonas, Stefanos Mourdikoudis, Lena Ciric, Nguyen T. K. Thanh (2021) The effect of ageing during growth of magnetite nanoparticles on their peroxidase-like activity. ACS Spring 2021.

Diana S. Raie, <u>Stefanos Mourdikoudis</u>, Antonis Makridis, Lena Ciric, Nguyen T. K. Thanh (2022) Synthesis of flower-like manganese ferrite nanostructures for

enhancing chromium bio-reduction by *Shewanella oneidensis*. 13th International Conference on the Scientific and Clinical Applications of Magnetic Carriers.

<u>Diana S. Raie</u>, Ioannis Tsonas, Stefanos Mourdikoudis, Lena Ciric, Nguyen T. K. Thanh
(2022) Spherical and flower-like manganese ferrite nanostructures for enhancing chromium bio-reduction by *Shewanella oneidensis*. IEEE Around-the-Clock Around-the-Globe (AtC-AtG) Magnetics Conference.

Report

Diana SR Ahmed and A Strange (2019) Membrane Bioreactor of Electro-Conductive Nanocomposite for Hospital Wastewater Treatment. UCL Grand Challenges.

https://www.ucl.ac.uk/grand-challenges/case-studies/2019/apr/membrane-bioreactor-electro-conductive-nanocomposite-hospital-wastewater

Summer schools

- Laboratory of Excellence "Physics: Atoms, Light, Matter (PALM LabEx),
 2018
- Singapore Centre for Environmental Life Science Engineering (SCELSE),
 2019

Grant

Small Grant Challenge for Doctoral Student grant

Awards

- "Design with Impact" Third place from Engineering Without Boarders-UCL,
 UK
- "Transport of Goods" First place in Green Light: 180 Degrees Consulting
 Social Entrepreneurship Competition, from 180 Degrees Consulting UCL,
 UK
- Oliver Hare Altruism Award, from Olly's Future Foundation, UK (Runner up)

Table of contents

Abstract	5
Impact statement	7
Publications, summer schools and awards	10
Table of contents	13
Table of figures	17
List of abbreviations	25
List of tables	30
Acknowledgement	31
Chapter 1. Introduction	34
1.1 Economic and health considerations of Cr ⁶⁺	34
1.1.1 The oxidation states of Cr	35
1.1.2 Environmental and health hazards of Cr ⁶⁺	35
1.1.3 Exposure limits for Cr ⁶⁺	37
1.1.4 Sources of Cr ⁶⁺ pollution	37
1.1.5 Methods for safe removal of Cr ⁶⁺	39
1.2 Microbial reduction of Cr ⁶⁺ using <i>Shewanella oneidensis</i> MR-1	40
1.2.1 Non-pathogenicity and bio-safety	41
1.2.2 Simple growth conditions of <i>S. oneidensis</i> MR-1	41
1.2.3 Bacterial tolerance to a high concentration of Cr ⁶⁺	42
1.2.4 Versatile sites for the detoxification of Cr ⁶⁺ using <i>S. oneidensis</i> MR-1.	42
1.2.5 Multiple mechanisms for Cr ⁶⁺ reduction by <i>S. oneidensis</i> MR-1	46

1.2.6	6 Limitations for using <i>S. oneidensis</i> MR-1 to detoxify Cr^{6+}	47
1.3	Strategies for enhancing Cr ⁶⁺ Bio-reduction by <i>Shewanella</i>	49
1.3.	1 Biomass-related strategies	49
1.3.2	2 Microbial Fuel Cells (MFCs)	51
1.3.3	3 Pre-treatment of effluents	52
1.3.4	4 Chemical-assisted strategies	52
1.4 Res	search gap	58
1.5 Ain	n and objectives	60
1.6 The	esis outline	61
Chapte	er 2. Synthesis and characterisation of spherical and flower-like	manganese
ferrite	nanostructures	64
2.1	Introduction	64
2.2	Materials and methods	65
2.2.2	1 Chemicals for NS preparation and characterisation	65
2.2.2	2 Synthesis of Mn _x Fe _{3-x} O ₄ NS	65
2.2.3	3 Characterisation of Mn _x Fe _{3-x} O ₄ NS	67
2.2.4	4 Functionalisation of Mn _x Fe _{3-x} O ₄ NS	68
2.2.5	5 Statistical analysis	69
2.3 Res	sults and discussion	70
2.3.	1 Synthesis of nanomaterials	70
2.3.2	2 Characterization of Mn _x Fe _{3-x} O ₄ NPs	70
2.3.3	3 Characterisation of Mn _x Fe _{3-x} O ₄ NFs	81
2.3.4	4 Growth of the selected Mn _x Fe _{3-x} O ₄ NPs over time	86
234	5 Flemental analysis of Mn. Fe ₂ . O ₄ NS	92

	2.3.6 Functionalization of NPs and NFs	94
2.	4 Conclusion	99
C	hapter 3. The adsorption capacity of the prepared $Mn_xFe_{3-x}O_4$ NS for Cr^{6+}	100
3.	1 Introduction	100
3.	2 Materials and methods	101
	3.2.1 Chemicals	101
	3.2.2 Fe quantification in NS	101
	3.2.3 Cr ⁶⁺ quantification	101
	3.2.4 Cr ⁶⁺ removal by nano-adsorbents	102
	3.2.5 Statistical analysis of adsorption experiments	104
3.	3 Results and discussion	105
	3.3.1 Adsorption of Cr ⁶⁺ by NS	105
	3.3.2 Impact of time-dependent growth of the selected NPs on their Qe for Cr ⁶⁺ .	108
	3.3.3 Isotherm of Cr ⁶⁺ adsorption by the selected NPs	109
	3.3.4 The oxidation state of Mn and Fe in the selected Mn _x Fe _{3-x} O ₄ NPs	111
	3.3.5 Reduction of Cr ⁶⁺ by the selected Mn _x Fe _{3-x} O ₄ NPs	115
	3.3.6 The proposed mechanism of Cr ⁶⁺ adsorption by Mn _x Fe _{3-x} O ₄ NPs	120
3.	4 Conclusion	121
C	hapter 4. Enhancing the bio-detoxification efficiency of Shewanella oneidens	is
M	IR-1 for Cr ⁶⁺ by the selected Mn _x Fe _{3-x} O ₄ NPs	122
4.	1 Introduction	122
4.	2 Materials and methods	124
	4.2.1 For microbiological studies	124
	4.2.2 Sources of heaterin of interest	125

4.2.3 Molecular identification of the tested bacteria	125
4.2.4 Microbial viability under Cr ⁶⁺ stress	127
4.2.5 Integrated adsorption bio-reduction safe removal of Cr ⁶⁺	128
4.2.6 Statistical analysis	129
4.3 Results and discussion	130
4.3.1 Molecular identification of the tested <i>Shewanella</i>	130
4.3.2 The viability of the tested <i>Shewanella</i> under Cr ⁶⁺ stress in the presence of	the
selected Mn _x Fe _{3-x} O ₄ NPs	131
4.3.3 Bio-removal efficiency of Cr ⁶⁺ by combining the tested <i>Shewanella</i> strain	s and
the selected Mn _x Fe _{3-x} O ₄ NPs	138
4.3.4 Enhanced morphological response of <i>S. oneidensis</i> MR-1 to Cr^{6+} by the	
selected Mn _x Fe _{3-x} O ₄ NPs	141
4.3.5 Boosted respiration of Cr ⁶⁺ via S. oneidensis MR-1 by the selected Mn _x Fe	≥3-xO4
NPs	145
4.4 Conclusion	151
Chapter 5. Conclusion and Future Outlook	153
5.1 Summary	153
5.2 Conclusion	155
5.3 Future work	155
D.£	1/2

Table of figures

Figure	1: Representation of the enhancement strategy for the bio-reduction of Cr^{6+}	
	studied in the current project60	
Figure	2: Flowchart of the experimental activities in the current PhD63	
Figure	3. TEM images for the spherical (A) undoped Fe ₃ O ₄ NPs, (B) Mn _x Fe _{3-x} O ₄ of	
	precursor ratio $[Mn(acac)_2] / [Fe(acac)_3] = 0.33$, $(C) [Mn(acac)_3] / [Fe(acac)_3]$	
	= 0.33 prepared at 200 °C as reaction temperatures, (D) undoped Fe ₃ O ₄ NPs and	
	(E & F) $Mn_xFe_{3-x}O_4$ NPs prepared with the same precursor ratio but at 250 °C.	
	71	
Figure	4: TEM images of spherical $Mn_xFe_{3-x}O_4$ nanoparticles (NPs) prepared by	
	solvothermal method at 250 °C. The precursor concentration ratio of (A-E)	
	$[Mn(acac)_2]/[Fe(acac)_3]$ and $(F-J)[Mn(acac)_3]/[Fe(acac)_3]$ respectively were	
	0.14, 0.6, 1, 1.66 and 372	
Figure	5: Impact of reaction temperatures (200 vs 250 °C) on (A) D _{TEM} of Mn _x Fe _{3-x} O ₄	
	NPs prepared from $0 \le [Mn(acac)_{2 \text{ or } 3}] / [Fe(acac)_{3}] \le 3$. (B) Polydispersity index	
	(PDI) of NPs diameters varied with precursor concentration ratios (0 \leq	
	$[Mn(acac)_{2 \text{ or } 3}] / [Fe(acac)_{3}] \le 3)$ calculated from TEM73	

Figure	9: XRD patterns of TEG (A) before and (B) after thermal treatment at 250 $^{\circ}$ C for
	6 h in the autoclave79
Figure	10: Polydispersity index (PDI) of D_{XRD} varied with precursor concentration ratios
	calculated from XRD at the most intense peak of (311) at annealing temperature
	(200 vs 250 °C)80
Figure	11: TEM images and histograms for D_{TEM} of NFs prepared from [Mn(acac) ₃]/
	$[Fe(acac)_3] = (A \& B) \ 1 \& 3 \ at \ synthesis \ temperature \ 200 \ ^{\circ}C, \ respectively \ (C) \ 7$
	at synthesis temperature 250 °C82
Figure	12: XRD patterns of $Mn_xFe_{3-x}O_4$ NFs prepared from $[Mn(acac)_3]$ / $[Fe(acac)_3]$
	ratio equal to (A) 1 and (B) 3 at 200 °C, (C) 7 at 250 °C. A secondary phase-
	matched MnCO3 (Reference ICDD PDF card no. 00-044-1472) was found for
	NFs prepared from a precursor equal to 7 at 250 °C. No detected peaks matched
	Mn ₃ O ₄ (PDF card no. 01-080-0382)84
Figure	13: XRD patterns of a produced sample where [Mn(acac) ₂] / [Fe(acac) ₃] was 7.
	Reference JCPDS card no. 00-044-1472, 00-029-0713, for MnCO ₃ , FeOOH,
	respectively85
Figure	14: TEM images of the growth of spherical Fe ₃ O ₄ NPs over a time range of 2-24
	h at a reaction temperature of 250 °C. DTEM is an average of 500 measured
	particles87

Figure 15: TEM images of $Mn_xFe_{3-x}O_4$ NPs prepared from $[Mn(acac)_2]$ / $[Fe(acac)_3]$
equal to 0.33 over a time range of 2-24h where 500 particles were measured per
each tested time point88
Figure 16: XRD diffractograms of Fe ₃ O ₄ NPs prepared at 250 °C for reaction time (2 h
-24 h). XRD patterns were matched to reference Fe ₃ O ₄ (PDF card no 01-089-
0688)
Figure 17: XRD patterns of $Mn_xFe_{3-x}O_4$ NPs prepared by $[Mn(acac)_2]$ / $[Fe(acac)_3]$ =
0.33 at 250 °C for synthesis time (2 h-24 h) during. The horizontal arrow pointed
out the shifting in the peak of 311 towards the reference Fe ₃ O ₄ (PDF card no 01-
089-0688) from the lower diffraction angle of MnFe ₂ O ₄ (PDF card no 00-010-
0319) in response to the increase in reaction time, which is represented by the
vertical arrow90
Figure 18: Synthesis time-dependent (A) $D_{TEM}(B) D_{XRD}(C)$ PDI of particle diameter and
crystal size of Fe_3O_4 NPs and $Mn_xFe_{3-x}O_4$ NPs prepared from $[Mn(acac)_2]$ /
[Fe(acac) ₃] equal to 0.33 and both NPs were thermally treated at 250 °C for
synthesis time ranged from 2 h to 24 h91
Figure 19: Elemental analysis of $Mn_xFe_{3-x}O_4$ NS (A) prepared at temperatures 200 °C
and 250 °C for 6 h. (B) that were prepared using $[Mn(acac)_2]$ / $[Fe(acac)_3]$ =
0.33 at synthesis temperature 250 °C for synthesis time 2-24 h. * $P < 0.05$ and
** $P < 0.01$ in comparison to $Mn_x^{3+}Fe_{3-x}^{3+}O_4$ NPs of similar precursor ratios. 93

Figure 20: Impact of variation in ratios between [Mn(acac) _{2 or 3}] / [Fe(acac) ₃] in Mn _x Fe	23-
$_xO_4$ NS and synthesis temperature (200 vs 250 °C) on D_{HD} of citrate-coated NI	P_{S}
and NFs. ** p < 0.01 showed the statistical confidence levels when comparing the	he
size with Fe ₃ O ₄ NPs synthesised at 250 °C9)4
Figure 21: An increase in D_{HD} of citrate coated (A) Fe $_3O_4$ NPs and (B) Mn $_{0.2}$ Fe $_{2.8}O_4$ NI	P_S
prepared at a temperature of 250 $^{\circ}$ C over synthesis time 2-24 h9) 5
Figure 22: Impact of variation in [Mn(acac) _{2 or 3}] / [Fe(acac) ₃] and synthesis temperatu	re
(200 vs 250 °C) on ζ -potential of NPs and NFs coated by citrate9	€
Figure 23: FTIR of TEG and selected TEG coated (A) Fe $_3O_4$ NPs prepared at 250 °C fo	or
6h of synthesis time (B) Mn _x Fe _{3-x} O ₄ NPs prepared at 250 °C for 6h of synthes	is
time where $[Mn(acac)_{2 \text{ or } 3}]$ / $[Fe(acac)_{3}]$ was 0.33 (C) $[Mn(acac)_{3}]$ / $[Fe(acac)_{3}]$	3]
was 3, (D) $Mn_{0.8}^{3+}Fe_{2.2}^{3+}O_4$ NFs [Mn(acac) ₃] / [Fe(acac) ₃] was 3 and (E) Mn ₃ C) 4
NPs9) 7
Figure 24: FTIR spectra of tri-sodium citrate alone, (A) Fe ₃ O ₄ NPs prepared at 250 $^{\circ}$	°C
for 6h of synthesis time, $Mn_xFe_{3-x}O_4$ NPs prepared at 250 °C where (1	B)
$[Mn(acac)_2]/[Fe(acac)_3]$ and $(C)[Mn(acac)_3]/[Fe(acac)_3]$ were 0.33, for 6h	of
synthesis time (D) $[Mn(acac)_3]$ / $[Fe(acac)_3]$ was 3, (E) $Mn_{0.8}^{3+}Fe_{2.2}^{3+}O_4$ Ni	Fs
$[Mn(acac)_3]/[Fe(acac)_3]$ was 3 and (F) Mn_3O_4 NPs. and all samples were coate	₽d
by cityata	20

Figure	25: Adsorption capacity (Qe) for Cr^{6+} by (A) $Mn_xFe_{3-x}O_4$ NS (B) Fe_3O_4 and
	$Mn_x^{2+}Fe_{3-x}^{3+}O_4 NPs ([Mn(acac)_2]/[Fe(acac)_3] = 0.33) $ on their Qe for Cr^{6+} , (both
	NPs were prepared at 250 °C for ageing time 2-24 h). * $P < 0.05$ and ** $P < 0.01$
	in relation Fe ₃ O ₄ NP which was prepared at 250 °C for 6 h106
Figure	26: Adsorption isotherm for Cr^{6+} and linearisation of Cr^{6+} adsorption fitted by
	Langmuir model for (A) Fe_3O_4 , (B) $Mn_{0.2}^{+2}Fe_{2.8}^{+3}O_4$ and (C) Mn_3O_4 NPs 110
Figure	27: XPS spectra of $Mn_xFe_{3-x}O_4$ NPs where orange and blue represent
	$Mn_{0.2}^{2+}Fe_{2.8}^{3+}O_4$ and $Mn_x^{3+}Fe_{3-x}^{3+}O_4$ respectively
Figure	28: High-resolution XPS spectra of (A, B) Mn 2p, (C, D) Fe 2p; for $Mn_{0.2}^{2+}Fe_{2.8}^{3+}O_4$
	$(A, C) \ and M n_x^{3+} F e_{3-x}^{3+} O_4 \ NPs \ (B, D).$ 114
Figure	29: XPS spectrum of $Mn_{0.2}^{2+}Fe_{2.8}^{3+}O_4$ NPs treated by Cr^{6+}
Figure	30: For $Mn_{0.2}^{2+}Fe_{2.8}^{3+}O_4$ NPs treated by Cr^{6+} , high-resolution XPS spectra of (A)
	Mn 2p and (B) Fe 2p (C) Cr 2p
Figure	31: Scheme for Cr^{6+} adsorption-reduction by NPs. Redrawn from Xie et al. ²¹³ and
	Johnston and Chrysochoou. ²¹² 121
Figure	32: Gating strategy for identifying the live and dead cell bacterial populations
	acquired by flow cytometry

Figure	33: Viability of the tested Shewanella strains in response to (A) Cr^{6+} , (B) Fe_3O_4
	$NPs, (C) Mn_{0.2}^{2+} Fe_{2.8}^{3+} O_4 NPs $ and $(D) Mn_3 O_4 NPs$
Figure	34: In the presence of the tested agents: (A) the viability of tested Shewanella
	under a sublethal dose of Cr^{6+} , (B) the removal of Cr^{6+} by Shewanella strains. *
	$P < 0.05$ and ** $P < 0.01$ in relation to the impact of $Mn_{0.2}^{2+}Fe_{2.8}^{3+}O_4$ NPs in each
	data set separately136
Figure	35: SEM micrographs of (A) untreated S. oneidensis MR-1 cells (B & C) treated
	cells by Cr^{6+} alone & $Mn_{0.2}^{2+}Fe_{2.8}^{3+}O_4$ NPs alone; respectively (D) treated cells by
	both Cr^{6+} and $Mn_{0.2}^{2+}Fe_{2.8}^{3+}O_4$ NPs
Figure	36: After being incubated with S. oneidensis MR-1, (A) XPS spectra of
	$Mn_{0.2}^{2+}Fe_{2.8}^{3+}O_4NPs$ (B) high-resolution XPS spectrum of Fe 2p145
Figure	37: XPS spectra of Cr^{6+} after being (A) incubated with S. oneidensis MR-1 alone
	and (B) treated by both S. oneidensis MR-1 and $Mn_{0.2}^{2+}Fe_{2.8}^{3+}O_4$ NPs147
Figure	38: High-resolution XPS spectra of Cr 2 p after incubating Cr^{6+} with (A) S .
	oneidensis MR-1 alone, (B) S. oneidensis MR-1 in the presence of
	$Mn_{0.2}^{2+}Fe_{2.8}^{3+}O_4NPs.$ 148
Figure	39: The possible mechanisms of Cr^{6+} reduction by S. oneidensis MR-1 to Cr^{3+} .
	Redrawn from ¹⁵⁶

Figure 40: Possible synergistic scenarios o	f S. oneidensis MR-1 and $Mn_{0.2}^{2+}Fe_{2.8}^{3+}O_4$ NP.
on Cr ⁶⁺ reduction. Redrawn from. ¹⁵⁰	⁶ 150

List of abbreviations

ATR: Attenuated Total Reflection (ATR)

ATSDR: Agency for Toxic Substances and Disease Registry

BE: Binding Energy

BLAST: Basic Local Alignment Search Tool (BLAST)

COPR: Chromite ore processing residue

CymA: Cytoplasmic membrane-anchored tetraheme *c*-type cytochrome

DET: Direct Electron Transfer

D_{HD}: Hydrodynamic size

DLS: Dynamic Light Scattering

dmsEFA: DMSO reductase system

DMSO: dimethyl sulfoxide

DPC: Diphenylcarbazide

D_{TEM}: Particle diameter

D_{XRD}: Crystal size

EPS: Extracellular polymeric substances

EU: European Union

Fcc: Face-centred cubic

FDA: Food and Drug Administration

Fe(acac)₃: Iron(III) acetylacetonate

FMO: Fluorescence minus one

FTIR: Fourier transform infrared

FWHM: Full Width Half Maximum

IARC: International Agency for Research on Cancer

ICDD PDF: International Centre for Diffraction Data Powder Diffraction File

ICP-AES: Inductively Coupled Plasma Atomic Emission Spectrometery

K₁: Binding sites' affinity

MET: Mediated Electron Transfer

MFCs: Microbial Fuel Cells

MIC: Minimum Inhibitory Concentration

Mn(acac)₂: Manganese(II) acetylacetonate

Mn(acac)₃: Manganese(III) acetylacetonate

mtr: metal reducing

mtrA: metal-reducing protein A

mtrB: metal-reducing protein B

mtrC: metal-reducing protein C

mtrD: metal-reducing protein D

mtrE: metal-reducing protein E

mtrF: metal-reducing protein F

NAD(P)H: Nicotinamide Adenine Dinucleotide Phosphate

NADH: Nicotinamide Adenine Dinucleotide

NCBI: National Center for Biotechnology Information

NFs: Nanoflowers

NPs: Nanoparticles

NS: Nanostructures

OD: Optical density

P: probability

PBS: Phosphate buffer saline

PCR: Polymerase chain reaction

PECs: periplasmic electron carriers

Qe: Adsorption capacity

Q_{max}: Maximum adsorption

ROS: Reactive Oxygen Species

SEM: Scanning Electron Microscopy

SO: Sequence Ontology

TCA: Tricarboxylic acid

TEG: Tetra-ethylene glycol

TEM: Transmission Electron Microscopy

WHO: World Health Organization

XPS: X-ray photoelectron spectroscopy

XRD: X-ray powder diffraction

ZVI: Zero-valent iron

 ζ -potential: Zeta potential

List of tables

Table 1: Summary of 311 peak positions and crysta	d size $(D_{XRD})^a$ determined by XRD of
$Mn_xFe_{3-x}O_4$ NPs prepared at 250 °C	75
Table 2: Calculated linear parameters for Cr^{+6} and	sorption on NPs fitted by Langmuir
model for isotherm	111
Table 3: Quantitative variation in the length an	d diameter of S. oneidensis MR-1
bacterial cells in response to the tested treat	ment143

Acknowledgement

Doing PhD studies during the COVID time was a challenging journey that I would have never been able to complete without the help of supportive people I met along the way. Therefore, I would like to thank all of them and recognise their value added to this journey.

I am expressing my sincere gratitude to my supervisors, Professor Nguyen T. K. Thanh and Dr Lena Ciric, whose expertise, support and supervision made it possible for me to work on a project I am interested in. I appreciate Professor Peter Wilson for hosting me in his lab. Dr Laurent Bozec for helping me to gain funding and supporting me.

I was lucky to be granted two priceless gifts: Dr Stefanos Mourdikoudis and Dr Melisa Canales. Dr Mourdikoudis is a senior Post-Doctoral researcher in Thanh's team who was always available to help me. Dr Canales, the lab manager of Ciric's lab, was supported throughout my studies.

In addition, I would like to thank Dr Stephen Nesbitt, the lab manager of Healthcare Biomagnetics Laboratories at the Royal Institution of Great Britain. Also, I appreciate Dr Shanom Ali for his guidance in microbiology.

I would like to thank Mr Ioannis Tsonas for his help in some particle synthesis and data analysis during his master's degree. I thank Ana Alvarez Prendes for participating in the data analysis of some TEM images during her master's degree as a dry project. Also, it was an excellent opportunity for me to take part in the training of Ms

Rachel Duan. Mr Thithawat Trakoolwilaiwan is acknowledged for the ICP-AES analysis, and Shanom Ali for helping me in the microbiology work.

I appreciate Konstantinos Simeonidis, Evangelia Delli, Antonis Makridis and Dimitrios Karfaridis from the Department of Physics, Aristotle University of Thessaloniki, Greece, for carrying out XPS characterisation, processing data and correcting my interpretation of the data. In addition, professor Georgios Vourlias at the University of Thessaloniki is thanked for providing resources for XPS characterisation. Finally, Dr Linh Nguyen and Dr Nicola Mordan at UCL Eastman Dental Institute were appreciated for using Scanning Electron Microscopy property.

I would like to thank Professor Jeffrey A. Gralnick, Professor of Plant and Microbial Biology at the University of Minnesota, for providing me with *Shewanella oneidensis* JG1486 and JG3355, which were used as biological controls during my studies. Also, I appreciate the efforts of Prof. Quentin Pankhurst at UCL for helping me to receive the bacteria from USA.

I acknowledge funding from Newton Mosharafa scholarship given to the Egyptian Petroleum Research Institute. I thank UCL Grand Challenges and UCL Small Grant for funding. Adam Strange was admitted for participation in writing UCL Small Grant application.

Last but not least, I would like to thank my mother, who has always supported me all my life. No words are enough to express my appreciation for all the care and confidence my mother gave me, always believing in me even in the most challenging moments. My siblings Doaa, Alaa and Nabil, thank you so much for undoubtfully believing in me. Thank you.

Chapter 1. Introduction

The contamination of air, soil and water by heavy metals is a hazard to human health and the environment. Any metallic element with a density greater than 5 g/cm³ is described as heavy metal. They show toxicity even at low concentrations.² The threat of heavy metals was attributed to being non-degradable.³

Among many heavy metals, chromium (Cr) is a common environmental pollutant in several industries. The toxicity of Cr to humans depends on its oxidation state. ^{2–5} World Health Organization (WHO) reported that occupational respiratory carcinogens, including hexavalent chromium (Cr⁶⁺), had impacted 0.1 million deaths globally. ⁶ The leaking of Cr⁶⁺ into irrigating water can damage crop yield. ^{2,3} Due to the hazards mentioned above of Cr⁶⁺, developing cost-effective methods for removing such heavy metals from water is an urgent need, mainly because of the global water and food shortage crisis. Integrating adsorption and bio-reduction is a promising way for Cr⁶⁺ removal. ^{7–11} Therefore, the present PhD aims to enhance the microbial reduction of Cr⁶⁺ to a less toxic trivalent form (Cr³⁺) using nano-adsorbents.

1.1 Economic and health considerations of Cr6+

Cr is ranked as the twenty-first most abundant element and is found as chromite.² According to the United States Geological Survey, the total worldwide mine production volume of Cr is 41 million metric tons in 2022.¹² The leading producers of Cr are South Africa (18 million metric tons), Kazakhstan and Turkey (7 million metric tons), India (3

million metric tons), and Finland (2.3 million metric ton), while all other countries produced only 4.4 million metric ton.¹²

1.1.1 The oxidation states of Cr

Cr, as a chemical element of atomic number 24, has the electron configuration [Ar] 3d⁵ 4s^{1,3} Cr has two common stable oxidation states, the highly toxic carcinogenic Cr⁶⁺ and less toxic and insoluble trivalent (Cr³⁺) of electron configuration [Ar] 3d³ 4s⁰. The solubility of Cr⁶⁺ is higher than Cr³⁺, and it is commonly present in nature as oxyanion as chromates or di-chromates, which is analogous to the structure sulfate and phosphate. This structural similarity facilitates its absorption by biological cells and increases its toxicity.² The natural oxidants may convert Cr³⁺ to Cr⁶⁺.^{2,3} The zero-valent Cr (Cr⁰) is used in iron alloys as stainless steel. The divalent (Cr²⁺) form of an electron configuration [Ar] 3d⁴ 4s⁰, can be easily oxidised into Cr³⁺.² The oxidation states of 1+, 2+ and 5+ Cr are rare.²

1.1.2 Environmental and health hazards of Cr6+

In 2019, the Agency for Toxic Substances and Disease Registry (ATSDR) considered Cr the 17^{th} on the substance priority list. The danger of Cr to human health and plants depends on its oxidation state and its concentrations. For example, a concentration ≥ 0.2 mg/mL of Cr⁶⁺ can cause DNA damage, but Cr³⁺ at ≥ 1.0 mg/mL can do such nucleic acid impairment. Because Cr⁶⁺ is a carcinogenic contaminant, it will be the principal focus of the following sections.

A. Human health

Cr⁶⁺ can cause liver damage, ulcer, pulmonary congestion,¹⁵ neurotoxicities,¹⁶ skin irritation¹⁵ and cancer.⁵ The International Agency for Research on Cancer (IARC) has ranked Cr as No.1 carcinogen.¹⁷ Cr⁶⁺ enters the cell and is reduced by ascorbate, glutathione, and cysteine to Cr⁵⁺, Cr⁴⁺, and Cr³⁺. Because of the weak membrane permeability capacity, Cr³⁺ cannot cross the cell membrane, entrapping it within the cell. But Cr³⁺ can cause many pf genetic problems. Both Cr⁵⁺ and Cr⁴⁺ are highly reactive and cause oxidative stress and cytotoxicity.²

B. Animal Health

The toxicity of Cr to animals depends on its oxidation state¹⁸ and concentration.¹⁹ Cr³⁺ activates insulin receptors and improves farm animal productivity.¹⁸ Cr⁶⁺ damages the kidney, liver, and gastrointestinal tract of chickens.²⁰ Exposure to high concentrations of waterborne Cr⁶⁺ decreases the growth rate and quality of fish; however, the low concentration of Cr⁶⁺ improves the productivity of fish.¹⁹

C. Plants and Agriculture

Terrestrial plants such as cereals, pulses, vegetables, forages, and trees were affected by both Cr³⁺ and Cr⁶⁺, also Cr⁶⁺ damages aquatic plants.^{2,21} The toxicity symptoms of Cr in plants include inhibition of germination besides the growth of roots and seedlings.^{2,21} Some plants were hyper-accumulators and tolerant of Cr.^{2,21} Still, these plants should be highly concerned about avoiding the food chain contamination for humans and animals by eating these crops directly or indirectly as animal feed.²

1.1.3 Exposure limits for Cr⁶⁺

In the European Union (EU), around 900 k workers are exposed to Cr^{6+} at work. U.S. Environmental Protection Agency (EPA) reported the permissible limit of Cr^{6+} in drinking water to be 0.05 mg/L, supported by WHO guidelines. Directive EU 2017/2398 defined the Occupational Exposure Limits for the ambient air concentration of Cr^{6+} to 0.005 mg/m³,²⁴ while 0.025 mg/m³ of Cr^{6+} in welding, plasma-cutting or similar processes applies until January 2025.

However, soil, water, and the air around tannery industries, mining, disposed of chromite ore processing residue (COPR) and metallurgy sites have exceeded the limits of $Cr^{6+}.^{25}$ In 2019, the concentration of Cr in the River Clyde catchment, within some areas in the city of Glasgow, is 0.05 mg/L to 0.971 mg/L,²⁶ which is higher than the international exposure limits.^{22,23} The source of Cr in Glasgow is the disposed of COPR for Cr works over 1830–1968.²⁶ The concentration of Cr^{6+} in tannery effluents in Egypt was quantified as 788 ± 3.5 mg/L.²⁷ Untreated effluents from some industries are released into rivers, polluting the irrigating and drinking water.²⁵

1.1.4 Sources of Cr⁶⁺ pollution

A. Industrial wastes

The release of Cr in the environment was attributed to mining activities,²⁸ leakages from industrial sites and improper waste treatment associated with industrial processes.²⁹ Cr is a common environmental pollutant from several industries such as wood preservation,³⁰ leather tanning,³¹ steel production,^{32,33} wool dyeing,³⁴ painting,³⁵

refractories,³³ lasers,³⁶ and electroplating,³⁷ among others. Leaking of Cr⁶⁺ from petrol stations,³⁸ filling materials of wastewater treatment pipelines,³⁸ residues of fertilisers and pesticides³⁸ and dispersed fly ash of coal used in some thermal power stations.³⁹ The residues of incinerated Cr-containing waste and Cr-comprising ash⁴⁰ were listed as a hazardous source of the heavy metal contaminants.^{41,42}

B. End-of-life products

Unwanted, used products such as wood,³⁰ leather,^{43,44} electronic wastes⁴⁵ and other products are introduced as an additional source for Cr leakage in the environment.^{30,43–45} Construction and demolition wood can be used in power generation, but the metal content in wood, such as arsenic and Cr, limits its recycling.³⁰ Disposing of end-of-life Cr-tanned leather products is often done by incineration or landfill due to the presence of Cr.^{43,44} The global production of electronic left-over is 57.4 million metric tons annually.⁴⁶ Around 60.2% of the electronic wastes were metallic contents which involved Cr.⁴⁶ In the recycling sites of electronic wastes, the concentration of Cr in the breast milk of breastfeeding women was 16 times higher than those of residents in unpolluted areas.⁴⁷ Higher levels of blood Cr were found in children from the electronic waste-polluted regions.⁴⁷

C. Geogenic sources

Various Cr-bearing minerals release natural Cr into the surroundings.^{29,38} However, Egypt was not listed among the top five Cr-producing countries,¹² groundwater³⁸ and River Nile water⁴⁸ were reported to be contaminated by Cr.⁴⁸ The total

Cr was quantified to be 0.26 mg/L,³⁸ which was 5.2 times the recommended limits by EPA and WHO,^{22,23} while the concentration of Cr⁶⁺ only ranged from 0.012 to 0.058 mg/L.³⁸ The sources of Cr were suggested to be desert sites rich in Cr, petrol stations and wastewater treatment plants.³⁸ In Sarigkiol (a Greek City), Cr⁶⁺ was quantified in the groundwater as 0.12 mg/L.³⁹ The source of such Cr was suggested to be due to rocks,^{39,49} and dispersed fly ash from power plants.³⁹ So, water-rock interaction was assumed to be a source of underground water contamination and other human-made polluting activities.^{38,39}

1.1.5 Methods for safe removal of Cr⁶⁺

Safe removal of Cr⁶⁺ from water and wastewater should involve the recovery (elimination) step and detoxification (reduction into Cr³⁺ as a less toxic form). Various technologies have been developed to tackle the presence of Cr⁶⁺. Some common technologies are outlined below, which can be grouped into physical, chemical and biological styles.

A. Physical and chemical methods for Cr^{+6} removal

There are several methods for removing Cr⁺⁶ from wastewater based on physical separation, such as membranes⁵⁰ or using chemicals for coagulation.⁵¹ Also, photocatalysis,⁵² electrochemical treatment,⁵¹ adsorption^{53,54} showed high efficiency in Cr⁶⁺ remediation. Physical and chemical methods are described as simple, fast, and efficient for metal elimination. Still, both suffer from increased energy and raw materials consumption, which leads to increased treatment costs and low treatment efficiency.⁵⁵

Besides, the chemical method is not applicable for removing low concentrations of Cr⁶⁺ from the wastewater, and using high-concentration chemicals will cause secondary waste.^{56,57}

B. Bio-remediation of Cr^{+6}

Biological methods for removing Cr⁶⁺ benefit from the natural process of the growing living organisms at the treatment site.⁵⁷ Some plants accumulated Cr in their roots, poorly translocated to aerial parts. However, the efficiency of Phyto-remediation of Cr, the time required for harvesting plants to recover Cr from roots and re-growing plants again restricted their usage for Cr recovery from contaminated industrial effluents.²¹ Some living organisms can survive in places with relatively severe heavy metal pollution, such as tanning sewage⁵⁸ and coal mine effluents.^{3,59,60} These microorganisms can be isolated to detoxify such environmental pollutants. Using bacteria for bio-remediation was preferred due to their efficiency and their short lifetime.^{3,58-60}

1.2 Microbial reduction of Cr⁶⁺ using Shewanella oneidensis MR-1

Cr-resistant bacteria have been reported to detoxify Cr⁶⁺ to less toxic Cr³⁺. According to the chemical properties of the bacterial cell wall, Gram stain can classify bacteria into two major groups, Gram-positive and negative. Some bacteria, such as *Mycobacterium tuberculosis*, do not respond to Gram stains.⁶¹

Gram-positive bacteria achieve high Cr sorption mainly due to the high content of anionic polymers in cell walls. *Bacillus* species, as Gram-positive bacteria, are among

Cr-resistant bacteria.³ Gram-negative bacteria are resistant to Cr, such as *Pseudomonas* aeruginosa, Geobacter sulfurreducens, Serratia marescens, S. oneidensis MR-1, Alcaligenes faecal and Klebsiella oxytoca.⁶² The lipopolysaccharide in Gram-negative bacteria facilitates binding Cr with the cell surface.⁶²

The bio-safety of bacteria is an essential criterion for selecting biological agents for technology. *P. aeruginosa* showed resistance to Cr⁶⁺, but they are not favoured for biotechnology due to pathogenicity. ⁶³ So, *S. oneidensis* MR-1 was selected for the present study as Gram-negative metal-reducing bacteria, ^{9,64–67} because of the reasons discussed below.

1.2.1 Non-pathogenicity and bio-safety

All *Shewanella* genus species belong to the family *Shewanellaceae*, ⁶⁸ which was recognised for the first in 2004. *Shewanella* genus involved Gram-negative, motile with a polar flagellum and rod-shaped with positive oxidase and catalase reaction. ^{68,69} This genus involved pathogenic bacteria such as *S. algae*, ⁶⁹ while *S. oneidensis* MR-1 bacteria were non-pathogenic species. ⁷⁰ So, *S. oneidensis* MR-1 bacteria were recommended for many biotechnological applications.

1.2.2 Simple growth conditions of *S. oneidensis* MR-1

S. oneidensis MR-1 are facultative anaerobic bacteria. They can survive and grow under aerobic and anaerobic conditions. As a bacterial genus, Shewanella approved its ability to respire oxygen⁷¹ and other inorganic and organic materials under anaerobic conditions. Because of the less positive redox potentials of these terminal electron

acceptors compared to oxygen, the energy gain for the organisms and microbial growth rate is usually considerably lower than aerobic respiration.⁷²

1.2.3 Bacterial tolerance to a high concentration of Cr⁶⁺

The isolated microorganisms from highly contaminated media expressed tolerance to pollutants.⁵⁸ *S. oneidensis* MR-1 can respire Cr⁶⁺ at a concentration of 20 mg/L under anaerobic conditions.⁹ The minimum inhibition concentration of Cr⁶⁺ to *Shewanella* was reported to be 65 mg/L.⁷³ While the anaerobic ammonium oxidation process could tolerate 2 mg/L of Cr⁺⁶ after acclimation, 5 mg/L stress significantly inhibited anaerobic ammonium oxidation bacterial activity.⁷⁴ The capability of *S. oneidensis* MR-1 to resist Cr⁺⁶ was attributed to the contribution of different mechanisms to this function. The chromate efflux pump in *S. oneidensis* MR-1 extrudes Cr⁶⁺ from the cell cytoplasm.⁷⁵ The reduction of the highly soluble Cr⁶⁺ into less soluble Cr³⁺ either outside the cell.⁶⁷ or inside the cell.⁶⁶

1.2.4 Versatile sites for the detoxification of Cr⁶⁺ using *S. oneidensis* MR-1

The reduction of the highly soluble Cr^{6+} into less soluble Cr^{3+} either outside the cell.⁶⁷ or inside the cell.⁶⁶

A. Intracellular reduction of Cr^{6+}

Inside the cells, *S. oneidensis* MR-1 can reduce Cr^{6+} to Cr^{3+} under aerobic⁷⁶ and anaerobic conditions, ^{76–80} but the mechanism is slightly different. ⁷⁶ The redox potential of Cr^{6+} (1.33 V vs Standard Hydrogen Electrode, SHE) has been reported to be slightly

higher than the redox potential of oxygen (1.23 V).⁸¹ Under anaerobic conditions, Cr^{6+} is a favourable electron acceptor for bacteria in respiration as bacteria gain energy.⁸¹ But, a possible competition between oxygen and Cr^{6+} as electron acceptors in cells in the process of bacterial respiration affected the microbial detoxification of Cr^{6+} .⁶⁶

Nicotinamide Adenine Dinucleotide (NADH) and Nicotinamide Adenine Dinucleotide Phosphate (NAD(P)H) can be the electron donors for the reduction of Cr⁶⁺ to Cr³⁺ inside the cell. The intercellular detoxification of Cr⁶⁺ can produce Cr⁵⁺ (an active intermediate) and then be reduced to Cr³⁺ as a stable final product⁶⁶ or regenerated to Cr⁶⁺ by dioxygen.⁷⁵ Reactive Oxygen Species (ROS)⁷⁵ are produced, and the concentration of Cr⁶⁺ is unchanged. In addition, ROS has a lethal effect on the viability of bacteria, affecting their activity.⁶⁶ Cr³⁺, as the final product of Cr⁶⁺ reduction, can cause lethal impacts on DNA and proteins by interacting with carboxyl, phosphate, and thiol groups.⁸²

B. Extracellular reduction of Cr^{6+} by S. oneidensis MR-1

The ability of *Shewanella* sp. to do extracellular respiration was facilitated by the metal-reducing (mtr) respiratory pathway.⁸³ The route of extracellular electron transfer started from the oxidation of the organic matter as electron sources via the catabolic pathway and then the transport of electrons to the outer membrane,⁸³ as described below.

1. Electron source

Electron donors played a critical role in the extracellular respiration of Cr⁶⁺ or any other terminal electron acceptor by bacteria.⁸⁴ *S. oneidensis* MR-1 favoured using

low-molecular-weight salts of organic acids for growth such three carnon, C-3 materials as lactate (CH₃CHCOO⁻), ^{85,87} pyruvate (CH₃COCOO⁻) ⁸⁶ and two-carbon compounds like acetate (CH₃COO⁻), ^{88,89} one-carbon, C-1 unit like formate as sources of carbon and energy. ⁹⁰ For Cr⁶⁺ bio-reduction, *S. oneidensis* MR-1 used sodium lactate as a carbon source for most studies in the presence or absence of oxygen. ^{66,91–93} Under aerobic and anaerobic respiratory conditions, *S. oneidensis* MR-1 can oxidise lactate to pyruvate using Lactate Dehydrogenase enzymes. ^{85,87}

2. Central carbon metabolism pathway

The pyruvate is metabolised by pyruvate dehydrogenase or pyruvate formatelyase, as summarised by Kouzuma. ⁹⁴ Under aerobic conditions, pyruvate oxidation by pyruvate dehydrogenase in the presence of NAD+ produces acetyl coenzyme A (acetyl-CoA), carbon dioxide (CO₂), and NADH. ⁸⁶ The resulting NADH was oxidised back to NAD+ by NADH dehydrogenase combined with the reduction of quinones into quinol. Acetyl-CoA was completely oxidised into CO₂ and generated NADH following a complete tricarboxylic acid (TCA) cycle. ⁹⁵

Under anaerobic conditions, pyruvate formate-lyase oxidised pyruvate into acetyl-CoA and formate.⁸⁶ Formate was oxidised to CO₂ by formate dehydrogenase acting with quinones.⁹⁰ The anaerobic conditions repressed TCA cycle. The phosphotransacetylase-acetate kinase pathway synthesises acetate from acetyl-CoA.⁹⁶ One molecule of Adenosine triphosphate (ATP) is generated, and one molecule of acetate by substrate-level phosphorylation is released. Some genes involved in the TCA cycle are missed in *S. oneidensis* MR-1. Encoding genes for 2-oxoglutarate dehydrogenase

complex are not adequately expressed in *S. oneidensis* MR-1 under anaerobic conditions. ^{95,97,98} *S. oneidensis* MR-1 oxidise one lactate molecule without using the TCA cycle to acetyl-CoA, and one formate molecule is released.

3. Electron transport to the outer membrane

Respiratory electrons enter the quinone pool in the inner membrane. ⁹⁹ via NADH or formate oxidation, as reviewed by Beblawy et al. ⁹⁴ Quinone was reduced by electrons to quinol on the inner membrane. Cytoplasmic membrane-anchored tetraheme c-type cytochrome (CymA) received electrons from the menaquinone pool. ⁹⁴

Shewanella species used metal-reducing (mtr) proteins to transmit electrons from the cell to its outside. Such mtr proteins involve mtr C, A and B complex (mtrCAB), 100 mtr F, E and D complex (mtrFED), 101 dimethyl sulfoxide (DMSO) reductase system (dmsEFA) 102 and the SO4359–SO4360 system. 101 Electrons transfer within the periplasm in *S. oneidensis* MR-1 via periplasmic electron carriers (PECs). Both mtrA and mtrD are used by *S. oneidensis* MR-1 to reduce metals and flavin. 83 The act of the third PEC and dmsE proteins reduce DMSO as a terminal electron acceptor. The function of the fourth PEC gene (SO4360) was not revealed to date. 83 A direct interaction between PECs and outer-membrane cytochrome, including mtrC and OmcA, is facilitated by mtrB, an outer membrane β-barrel protein. 99,103,104

4. Extracellular electron transfer

For the electron flux across the outer membrane of *S. oneidensis* MR-1, mtrC and OmcA directly participate in electron transfer to extracellular minerals or extracellular

electron shuttles. 99,103,104 The outer-membrane cytochrome protein mtrF was involved in the direct electron transfer pathways to insoluble terminal electron acceptor and soluble flavin electron shuttles. 105

1.2.5 Multiple mechanisms for Cr⁶⁺ reduction by S. oneidensis MR-1

In *S. oneidensis* MR-1, the electron transfer across the outer membrane can occur either via direct electron transfer (DET) pathway, i.e. without using mediators, or mediated electron transfer (MET) which requires shuttles^{72,106} as will be described below.

A. DET

In the mechanism of DET, electron transfers from the electroactive cells to the terminal electron acceptor using direct physical contact with the bacterial cell membrane. The presence of Cr³⁺ particles on the cell surface of *S. oneidensis* MR-1 could have resulted from bio-reduction⁹¹ via the DET mechanism. *S. oneidensis* MR-1 can develop outer membrane and periplasmic extensions, including the multiheme cytochromes called nanowires. This organelle allows microbes to reach and use a distant solid anode surface or highly soluble terminal electron acceptor such as Cr⁶⁺. Nanowire also contains the MtrABC complex, via which electrons transfer to a terminal electron acceptor.

B. MET

MET mechanisms represented a pathway linking microbial metabolism to the terminal electron acceptors. Microbial cells can use redox species as electron mediators

to shuttle electrons outside the cell in the case of limited electron acceptors due to poor diffusion. The mediator acts as a reversible electron acceptor. They can be reduced to deliver electrons from the bacterial cell to an insoluble oxidant, solid substrate or aerobic biofilm layers. So, the mediators are re-oxidised by losing the electron and regenerated for subsequent redox processes. The redox mediators effectively enable the transfer of electrons and increase the efficiency of respiration.¹⁰⁹

These mediators can be exogenous electron shuttling compounds like humic acids, iron oxides, or metal chelates. Bacteria also can produce low-molecular (endogenous redox mediators) electron shuttling compounds. Bacterial phenazines like pyocyanine and flavins are examples of endogenous redox mediators that are produced via secondary metabolic pathways to be involved in extracellular electron transfer processes. 81,109,110

1.2.6 Limitations for using S. oneidensis MR-1 to detoxify Cr⁶⁺

Some limitations were reported that can impede using *S. oneidensis* MR-1 for Cr^{6+} removal. In the present project, the gaps among the tolerable dose of Cr^{6+} by bacteria, the highest concentration of Cr^{6+} that can be bio-detoxified, and the total concentration of $Cr^{3+/6+}$ in the effluents are the main focus.

A. Toxicity of Cr^{6+} to S. oneidensis MR-1

The lethal effect of Cr^{6+} on microbes during respiration $^{9,78,82,111-113}$ was considered a potential limitation for the bio-remediation of Cr^{6+} . The minimum

inhibitory concentration (MIC) of Cr^{6+} , the lowest concentration of Cr^{6+} that can stop the visible growth of bacteria, was reported to be ~ 42-65 mg/L for *S. oneidensis* MR-1.^{73,82}

Cr⁶⁺ was suggested to cause mutations that affected growth or non-reversible interaction with proteins that inhibited growth.⁸² The impact of Cr⁶⁺ on *S. oneidensis* MR-1 bacterial cell morphology and colonies was imaged.^{9,78,82,91} After reacting *S. oneidensis* MR-1 cells with Cr⁶⁺, bacterial cells' size decreased with a shrunken-surface shape,⁷⁸ cell membranes were damaged,⁹ and cracks were formed.⁷⁸ Exposing *S. oneidensis* MR-1 to 10 mg/L Cr⁺⁶ showed 10⁴⁻⁶ fold decreases in the plate count viability.⁸² The loss in viability of *S. oneidensis* MR-1 after Cr⁶⁺ treatment was suggested to be because of the intracellular effects of Cr⁶⁺.⁸²

B. Low efficiency of Cr^{6+} bio-reduction by S. oneidensis MR-1

The initial Cr^{6+} concentration had an inverse relationship with its reduction by *S*. *oneidensis* MR-1.^{66,78,114} This strain alone can reduce 26-78 % of 20 mg/L Cr^{6+} into Cr^{3+} within 8 h,^{78–80} which is much lower than what can be detoxified by physical and chemical materials.⁵⁸

C. High concentration of $Cr^{3+/6+}$ in industrial effluents

The concentration of $Cr^{3+/6+}$ in industrial effluents may be reached 1000-1500 mg/L, as was reviewed by Mpofu et al.¹¹⁵ Only 42-65 mg/L Cr^{6+} can stop the growth of *S. oneidensis* MR-1.^{73,82} The optimal concentration of Cr^{6+} bio-reduction by *S. oneidensis* MR-1 is 20 mg/L^{78–80,82} which is half of MIC value of Cr^{6+} . So, bio-remediation needs to be improved for the detoxification of heavy metals.

1.3 Strategies for enhancing Cr⁶⁺ Bio-reduction by Shewanella

The cytotoxicity of Cr^{6+} to *Shewanella* is the major limitation of using such metal-reducing bacteria as whole cells for its bio-detoxification. Therefore, enhancing the bacterial tolerance to Cr^{6+} was considered an effective way to improve the reduction of Cr^{6+} . Several methods can improve the viability of biomass and enhance the activity of bio-reductions 65,67,124–126,116–123 as follows.

1.3.1 Biomass-related strategies

A. Biofilm development

Microbial biofilms were defined as attached microorganisms to a solid surface and embedded within slimy extracellular polymeric substances (EPS).¹²⁷ Such microbial structure can boost the resistance of microbial cells to the toxicity of heavy metals by stopping the spread of pollutants. In addition, EPS can protect the growth of microorganisms. More EPS production was stimulated during the early growth stage of biofilm in response to Cr⁶⁺. EPS removed over 60% of the total adsorbed Cr⁶⁺. However, the dose-dependent toxicity of Cr⁶⁺ to the bacterial growth restricts using bacteria for Cr remediation even in the biofilm stage. Using a high biomass concentration to overcome the toxicity of Cr⁶⁺ produced Cr³⁺ and Cr⁶⁺ contaminated sludge, which increased the amount of landfill.³¹

B. Encapsulation of bacterial cells

Encapsulating bacteria within dopamine¹¹⁸ and alginate¹²³ polymers improved the bio-reduction of Cr⁶⁺ removal 3-3.7 times higher than free cells.^{118,123} However, the toxic effect of solvents and chemicals used in polymerisation was a limiting factor for this technique. Besides that, the encapsulation may affect the encapsulant's internal environment.¹¹⁹

C. Genetic engineering of cells

Enhancing the extracellular bio-reduction of Cr⁶⁺ by genetic engineering of *Shewanella* was also reported.^{120,124–126} The engineered strain showed 3 folds¹²⁰ and 5.5 folds¹²⁴ higher Cr⁶⁺reduction efficiency. The lack of effective synthetic biology tools restricted the practical applications of engineered microbes.¹²⁰ In addition, genetic-based enhancement was reported to impair metabolism and cellular growth because of the competition for limited cellular resources.¹²⁴

D. Long-term adaptation of biomass

Culturing microbial consortia with a gradual increase in the concentration of pollutants can enhance their tolerance to and interaction with pollutants. Such a strategy was designated as the acclimation process. *S. oneidensis* MR-1 was acclimated for 120 days by increasing the concentration of Cr⁶⁺ from 10 to 190 mg/L. The bacterium survived in the highly toxic Cr⁶⁺ environment because of the enhanced capability to reduce Cr⁶⁺ and the increased cell membrane surface. Although applying acclimatisation improves bacterial productivity in environmental biotechnology, it needs a long time, which

reaches 120 days.^{65,116} In addition, it remains uncertain how microorganisms gain tolerance to high concentrations of pollutants, which was risky to develop resistant bacteria.^{65,116}

1.3.2 Microbial Fuel Cells (MFCs)

MFCs are bio-electrochemical systems used for electricity production and waste treatment. The most common design for MFCs comprises two chambers separated by an ion exchange membrane. Electrons are recovered from organic substrates via microbial biodegradation in the anodic chamber. These electrons transfer from the anode and flow to the cathode through an external circuit. In parallel, protons are produced at the anode chamber and migrate across a selective barrier (proton exchange membrane) to the cathode chamber, forming water or other chemicals. MFCs can be used for the detoxification of Cr⁶⁺ and the production of bio-energy from industrial effluents. The critical advantages of MFCs compared to conventional fuel cells are the mild operation conditions, including temperature and pH. The

In MFCs, the ability of *Shewanella* species to detoxify Cr⁶⁺ and electricity production was reported.¹³⁰ *Shewanella*, biocatalysts at the cathode of MFCs, could reduce Cr⁶⁺ at a concentration of 2.5 mg/L.¹³⁰ *S. oneidensis* MR-1 was used in an anode chamber to oxidise molasses within the MFCs system. The released electrons were used to reduce 8 mg/L of Cr⁶⁺ solution at the cathode chamber into Cr³⁺.¹³¹ Mixed culture of *S. decolorationis* S12 and *Klebsiella pneumoniae* L17 can be used as an anode catalyst in MFCs. Here, Cr⁶⁺ can be reduced in an air—code dual-chamber, and hydrogen peroxide (H₂O₂) was electrogenerated at the cathode.¹³² The possibility of fouling in MFCs by the

biomass or reduced Cr species decreased the removal efficiency of Cr⁶⁺. The precipitated Cr species may also accumulate at the electrode surface after detoxification, resulting in a limited area for the reaction. Non-reducing bio-genic materials, such as inactive cells, dead biomass, cell debris, and biofilm matrices, restrict the active surface area at the electrode surface.¹³⁰

1.3.3 Pre-treatment of effluents

Diluting the effluents by adding water could be a pre-treatment step to decrease the concentration of the heavy metals. In contrast, results showed increased bioavailability of Cr⁶⁺ and guided process inhibition.¹²¹ In addition, such a way would consume much more water and create a need to retreat water again.

1.3.4 Chemical-assisted strategies

A. Anti-oxidants

Using ROS quenchers to protect *S. oneidensis* MR-1 from the oxidative stress of heavy metals was reported using hydrogen sulfide (H₂S), either that bio-produced or added to the process. However, such acid was well known for its toxic and corrosive properties.¹³³ Natural enzymes like catalase or superoxide dismutase can enhance the performance of biological-based methods. Their instability, cost, and difficult reusability limited their applications.¹³⁴

B. Carbon-based NS

Carbon can be a cost-effective conductive adsorbent by acting as a physical link between *S. oneidensis* MR-1. Charcoal also can promote the bio-reduction of Cr⁶⁺ by acting as an electron shuttle.⁹² Yet, applying carbon-based materials in heavy metal removal is limited by their poor generation besides their anti-microbial activity.¹³⁵ The biogenic palladium NPs enhanced the electron transfer efficiency from *S. oneidensis* MR-1 cells to Cr⁶⁺ cells 5 and 10 times when adding reduced graphene oxide,¹³⁶ but such metal is expensive and toxic to bacteria.¹³⁶

C. Iron-oxides and hydroxides

Iron oxide/hydroxide materials can enhance the bio-reduction of Cr^{6+} by acting as adsorbents, abiotic reducing agents or electron mediators. Adsorbing Cr^{6+} on schwertmannite and jarosite shortened the distance between the bacterial cells and Cr^{6+} , which improved Cr^{6+} bio-reduction. 7 Cr^{6+} adsorption on α -Fe₂O₃ NPs and microparticles enhanced Cr^{6+} bio-reduction by *S. oneidensis* MR-1. 79,80 The adsorption limits the Cr^{6+} solubility and the uptake of Cr^{6+} and Cr^{3+} (bio-reduction product) by the bacterial cells, 79,80 Combining α -Fe₂O₃ NPs and *S. oneidensis* MR-1 improved Cr^{6+} bio-reduction to Cr^{3+} by 1.09 and 1.46 times 79,80 using bacteria alone 79,80 and α -Fe₂O₃ microparticles alone. 79

S. oneidensis MR-1 can reduce the Fe³⁺ of ferrihydrite, ⁸ Goethite (α -FeOOH), ⁸⁻¹¹ and α Fe₂O₃¹³⁷ to Fe²⁺ as an abiotic reducing agent for Cr⁶⁺. ⁸⁻¹¹ The addition of biochar enhanced Fe³⁺ reduction by S. oneidensis MR-1, which increased the yields of biogenic

Fe²⁺ and improved the bio-reduction of Cr⁶⁺ into 13.8.⁸ α-FeOOH enhanced *S. oneidensis* MR-1⁹ and *S. putrefaciens* CN32¹¹ to detoxify 20-30% and 60% of Cr⁶⁺, respectively.^{9,11} The enhancement of Fe³⁺ reduction by *S. oneidensis* MR-1 increased the yields of biogenic Fe²⁺, which improved the bio-reduction of Cr⁶⁺ by around 18%.⁸ The reactivity of Fe₃O₄ towards Cr⁺⁶ was enhanced by microbial reduction of Fe³⁺ via *Geobacter sulfurreducens* and oxidation of Fe²⁺ via *Rhodopseudomonas palustris*.¹³⁷ Fe₃O₄ NPs showed limited lethal activity against bacteria.¹³⁸ Yet, Zhang et al. reported that biogenic Fe²⁺ from *S. oneidensis* MR-1 can contribute only by 5% of Cr⁶⁺ reduction, while the main Cr⁶⁺ reduction pathway for *S. oneidensis* MR-1 was probably via extracellular electron transfer.¹⁰

In contrast, Mohamed et al.⁷⁸ stated that the Cr^{6+} reduction rate declined to 56% in the presence of α -FeOOH, which was attributed to the coverage of S. oneidensis MR-1 bacterial surface by α -FeOOH.⁷⁸ The adhesion affinity between α -FeOOH and S. oneidensis MR-1 increased by 2-5 times under anaerobic conditions. Iron reductase in the outer membrane of S. oneidensis MR-1 can interact with α -FeOOH to facilitate the electron transfer process. This attachment of α -FeOOH to the surface of S. oneidensis MR-1 could disrupt the electron transfer and inhibit Cr^{6+} bioreduction.⁷⁸

S. oneidensis MR-1 cells were reported to attach to αFe_2O_3 surfaces¹³⁷ via van der Waals and electrostatic forces, followed by forming P–O–Fe bonds.¹³⁹ The structures of membrane proteins were changed, and the structural integrity of the membrane was lost.¹³⁹ So, αFe_2O_3 NPs can penetrate the cells, and ROS is generated on the surface of NPs, leading to cell toxicity. The cytotoxicity of αFe_2O_3 NPs could explain why the effect

of Cr^{6+} microbial removal by $\alpha\text{-Fe}_2O_3$ was only one-third of what was removed in the presence of $\alpha\text{-Fe}OOH.^{11}$

The presence of an electron shuttle in the coupled adsorption bio-reduction of Cr^{6+} by α -FeOOH and S. oneidensis MR-1 can mediate the electron transfer from bacteria to Fe³⁺-bearing materials and Cr^{6+} . 8,9,78 Biochar as an electron mediator increased the reduction extent of Fe³⁺ in α -FeOOH by S. oneidensis MR-1 around ~ 2.3 times. Anthraquinone-2,6-disulfonate can also increase the removal level of Cr^{6+} in the presence of both α -FeOOH and S. oneidensis MR-1 together by 2.6 times. Humic substances acted as an electron shuttle to accelerate the rates and extents of Cr^{6+} reduction by S. oneidensis MR-1. Mohamed et al. 8 suggested that humic acid diminished the bacterial cell adhesion to α -FeOOH to facilitate the electron transfer from S. oneidensis MR-1 to Cr^{6+} . 8 So, the reduction rate of Cr^{6+} by S. oneidensis MR-1 is mightily increased to 1.3 times in response to the combined effect of α -FeOOH and humic acid. Cr^{7+}

D. Zero-Valent Fe (ZVI) NPs

ZVI NPs are reported to improve the microbial remediation of Cr⁶⁺ from water⁶⁹ and soil.¹⁴² *Shewanella* alone can remove from 5.2 mg^{78–80} to 25 mg⁹¹ of Cr⁶⁺. In the presence of both ZVI NPs and *S. oneidensis* MR-1, around 112 mg of Cr⁶⁺ per gram of NPs was removed.¹⁴¹ The eliminated Cr⁶⁺ by a gram of ZVI supported by biochar in the absence of bacteria was 65.8 mg,⁹¹ which increased into 166.7-187 mg of Cr⁶⁺ per gram of ZVI/biochar by the synergic effect of *S. oneidensis* MR-1.^{91,143} ZVI NPs-microorganisms hybrid system achieved a remarkably 2.9 times higher Cr³⁺- removal than in the iron ZVI alone.¹⁴²

ZVI NPs reacted with Cr⁶⁺ to form Fe³⁺ hydroxides, which are deposited on the surface of NPs, resulting in the loss of reactivity of ZVI NPs.⁶⁹ EPS derived from *S. oneidensis* MR-1 eradicated the passivation layer from the surface of ZVI NPs^{91,141} and prolong its reactivity and Cr⁶⁺ removal.¹⁴¹ However, ZVI NPs could create an appropriate living circumstance as a terminal electron acceptor for anaerobic bacteria, it showed cytotoxicity reviewed by Dong et al.¹⁴⁴ This lethal effect of ZVI NPs was attributed to the generation of ROS, which has a detrimental effect on the microbial activity and Cr⁶⁺ reduction.¹⁴⁴

E. Mn and Fe mixed oxides

Manganese iron oxide and Fe^{3+} -oxides acted as binding agents after Cr^{6+} reduction during ageing in soil. The organo-Fe oxides play a critical part in reducing Cr^{6+} and the subsequent binding of Cr^{3+} . The exotic Cr^{6+} significantly altered the soil microbial consortia. The relatively low pH, organic materials and Fe oxide contents supported the growth of Cr-reducing bacteria. Such conditions improved the Cr^{6+} reduction in the soil. Cr^{6+} reduction in the

Manganese-doped iron oxide or manganese ferrite (MnFe₂O₄) in the nanoscale revealed no lethal effect during different toxicity tests. 146 MnFe₂O₄ has been stated to display enzyme-like activities $^{147-150}$ and accelerate extracellular electron transfer in MFCs. 151,152 The removal efficiency of Cr^{6+} by ferrites followed the order MnFe₂O₄ > magnesium ferrite (MgFe₂O₄) > zinc ferrite (ZnFe₂O₄) > copper ferrite (CuFe₂O₄) > nickel ferrite (NiFe₂O₄) > cobalt ferrite (CoFe₂O₄). 153 The maximum adsorption capacity

of MnFe₂O₄ NPs for Cr^{6+} was reported to be ranging approximately from 31 to $35\,mg/g.^{146,153}$

The electrostatic interaction between the surface of oxide and pollutants is one of the mechanisms of Cr⁶⁺ adsorption on MnFe₂O₄ NPs. Ion exchange in the aqueous solution between hydroxyl groups and oxyanions is another mechanism for heavy metal removal. Such a mechanism of adsorption allows the reusing of MnFe₂O₄ NPs and recycling of Cr⁶⁺ without losing the adsorption capacity or changing their oxidation states. Limited reports proposed a chemosorption for Cr⁶⁺ on the surface of MnFe₂O₄ NPs. In MnFe₂O₄, the existence of Mn and Fe in different oxidation states facilitates the reduction and oxidation processes on the nanoparticle surface. Surface of Mn and Surface of Mn and Surface Surface.

Despite the reported superiority of heavy metal removal by MnFe₂O₄, other works have stated that introducing Mn into ferrite reduced the adsorption capacity of magnetite to Cr^{6+} from 15.9 mg/g to 8.54-8.9 mg/g.^{155,156} The release of Mn to the solution because of Cr^{6+} reduction by nano-adsorbents diminished the adsorption capacity.¹⁵⁵

Doping level (x) in sulfur-doped $MnFe_2O_4$ ($MnFe_2O_4/FeS_x$)¹⁵⁷ and in cobalt-doped $MnFe_2O_4$ ($Mn_{1-x}Co_xFe_2O_4$)¹⁵⁸ showed a significant impact on the adsorption capacity for Cr^{6+} by $MnFe_2O_4^{157,158}$ which turned to be 5 times higher than that of undoped NPs.¹⁵⁶ The effect of the variation of atomic concentration of Mn in $Mn_xFe_{3-x}O_4$ NPs on particle size, saturation magnetisation,¹⁵⁹ adsorption performance of arsenic,¹⁶⁰ heating energy generation, magnetic anisotropy,¹⁶¹ and oxidase-like activity¹⁴⁸ have been illustrated in different research studies. However, the influence of structural features of $Mn_xFe_{3-x}O_4$ NPs on Cr^{6+} adsorption has not been thoroughly explored. The effect of the

oxidation state of Mn precursors on the chemical structure and morphological and magnetic properties of $Mn_xFe_{3-x}O_4$ NPs prepared by scalable polyol solvothermal method has been studied in a few reports^{162,163} but not in relation to their adsorption efficiency for heavy metals.

Using iron-based NPs in combination with metal-reducing bacteria has been applied to enhance the detoxification of Cr⁶⁺ to Cr³⁺ via acting as adsorbents, reducing agents and electron mediators.⁸ Iron is cheap and available material with limited toxicity impact on bacteria.⁶⁷ Due to the usage of Cr³⁺, Mn and Fe in the steel industry, ^{164,165} glass ceramics, ¹⁶⁶ fertilisers, ¹⁶⁷ Mn/Fe oxides can use as an adsorbent to recover Cr from industrial effluents or highly contaminated water. The recovered Cr can be used in metallurgical, glass and fertiliser industries to minimise landfill contamination. ^{164–167}

1.4 Research gap

The gap between the tolerable concentration of Cr^{6+} *S. oneidensis* MR-1 (~ 40-65 mg/L)^{73,82} and the total amount of Cr in the effluents (~ 788 mg/L)²⁷ is a critical problem in the biological treatment of Cr^{6+} . Using adsorbents can increase the viability of *S. oneidensis* MR-1, but the cytotoxicity of such supporting materials is challenging. ^{139,144}

Iron oxide/hydroxides were reported to boost the ability of *S. oneidensis* MR-1 to bio-reduce Cr^{6+} under anaerobic environments.^{69,160} Expect Fe₃O₄, surface passivation, cytotoxicity and attachment of materials on the surface of bacteria affected negatively on the bio-reduction of Cr^{6+} . Therefore, MnFe₂O₄ NS was selected for this research to adsorb Cr^{6+} . MnFe₂O₄ NS revealed biocompatibility,¹⁴⁶ supported growth of Cr-functional

bacteria, ¹⁴⁵ enzyme-like activities, ^{147–150} and accelerated extracellular electron transfer in MFCs, ^{151,152} and high removal efficiency of Cr⁶⁺. ^{145,146,153,154} The influence of the chemical structure and morphology of Mn_xFe_{3-x}O₄ NS on Cr⁶⁺ adsorption has not been thoroughly explored. The effect of the oxidation state of Mn precursors on the chemical structure and morphological properties of Mn_xFe_{3-x}O₄ NS prepared by scalable polyol solvothermal method has been studied in a few reports ^{162,163} but not in relation to their adsorption efficiency for heavy metals. Mn doping level Fe₃O₄ NPs on the adsorption efficiency of Cr⁶⁺ by Mn_xFe_{3-x}O₄ NS can affect the cost of the process of treatment. The current project addresses the following gaps in the literature:

- The impact of Mn doping level and the oxidation state of Mn precursor on the efficiency of Mn_xFe_{3-x}O₄ NS to adsorb Cr⁶⁺.
- The effect of the selected Mn_xFe_{3-x}O₄ NS on the bio-detoxification efficiency of Cr⁶⁺ by *S. oneidensis* MR-1 bacteria and considering the microbial viability during the reduction process.

1.5 Aim and objectives

Applying such nanostructures with a biological reduction of Cr^{6+} can overcome the accessibility of specific technologies, ¹²⁰ using less toxic chemicals and reducing the production of contaminated, poisonous waste. ¹³³ The current PhD project aims to enhance the bio-detoxification of Cr^{6+} to Cr^{3+} via adsorbing Cr^{6+} on nanostructures. This integrated adsorption and bio-reduction method are safe and cheap for heavy metal elimination from wastewater.

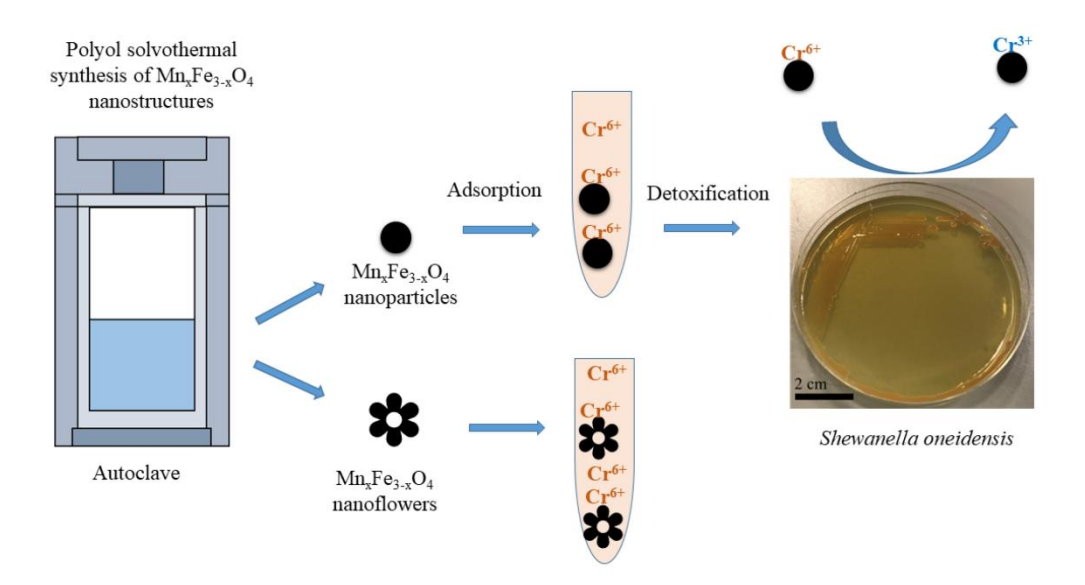


Figure 1: Representation of the enhancement strategy for the bio-reduction of Cr^{6+} studied in the current project.

Towards this target, the project was carried out as shown in *Figure 1* and with the following 3 objectives:

- Objective 1: Synthesis and characterisation of Mn_xFe_{3-x}O₄ nanoparticles (NPs) and nano-clusters.
- Objective 2: Determining the adsorption capacity (Qe) of the prepared
 Mn_xFe_{3-x}O₄ NS for Cr⁶⁺.
- Objective 3: Assaying the impact of the selected Mn_xFe_{3-x}O₄ NS on the bio-detoxification efficiency of Cr⁶⁺ by S. oneidensis MR-1

1.6 Thesis outline

This dissertation explains the current project's sequence of activities, as summarised in *Figure 2*. The outputs are structured in the following chapters:

Chapter 2 presents a synthetic platform for achieving the most suitable chemical structure of $Mn_xFe_{3-x}O_4$ NS to recover Cr^{6+} from artificial wastewater. The impact of two oxidation states of manganese precursors on the doping level in $Mn_xFe_{3-x}O_4$ NS and the morphological and crystal structure of NPs are tested. $Mn_{0.2}^{2+}Fe_{2.8}^{3+}O_4$ NPs are selected to study the impact of synthesis conditions, such as ageing time and annealing temperature, on their morphology and structures.

Chapter 3 discusses the nature of Cr^{6+} adsorption and removal by selected Mndoped ferrite. All experiments for heavy metal removal are done in semi-synthetic wastewater. $Mn_{0.7}^{2+}Fe_{2.8}O_4$ NPs prepared at a synthesis temperature of 250 °C for 6 h

showed the best Cr^{6+} adsorption capacity. The adsorption of Cr^{6+} by $Mn_{0.2}^{2+}Fe_{2.8}O_4$ NPs are fitted to Langmuir isotherm model as a function of initial Cr^{6+} concentrations. A chemical redox reaction took place between $Mn_{0.2}^{2+}Fe_{2.8}^{3+}O_4$ NPs and Cr^{6+} , as evidenced by X-ray Photoelectron Spectroscopy (XPS) analysis.

In Chapter 4, the bio-detoxification and tolerance of Cr^{6+} by *S. oneidensis* MR-1 assisted by $Mn_{0.2}^{2+}Fe_{2.8}^{3+}O_4$ NPs are described. The effect of $Mn_{0.2}^{2+}Fe_{2.8}^{3+}O_4$ NPs on the viability of *S. oneidensis* MR-1 in response to Cr^{6+} have been studied by flow cytometry and Scanning Electron Microscopy. In addition, Cr^{6+} bio-removal and bio-reduction were shown by the colourimetric method and XPS analysis, respectively.

In Chapter 5, our conclusion is drawn regarding the combination of adsorption and bio-reduction to improve the safe removal efficiency of Cr^{6+} . The original contribution to the knowledge is that $Mn_{0.2}^{2+}Fe_{2.8}^{3+}O_4$ NPs can boost the bio-detoxification of the carcinogenic Cr^{6+} to the less toxic form, Cr^{3+} , by *S. oneidensis* MR-1. In addition, lowering the doping level of Mn in the chemical structure of $Mn_xFe_{3-x}O_4$ NPs decreases the cost of NPs. Several studies are planned to be done as future work, as listed in Chapter 5, to reveal the mechanism of integrated adsorption bio-reduction of Cr^{6+} and to minimise the remediation cost of Cr^{6+} .

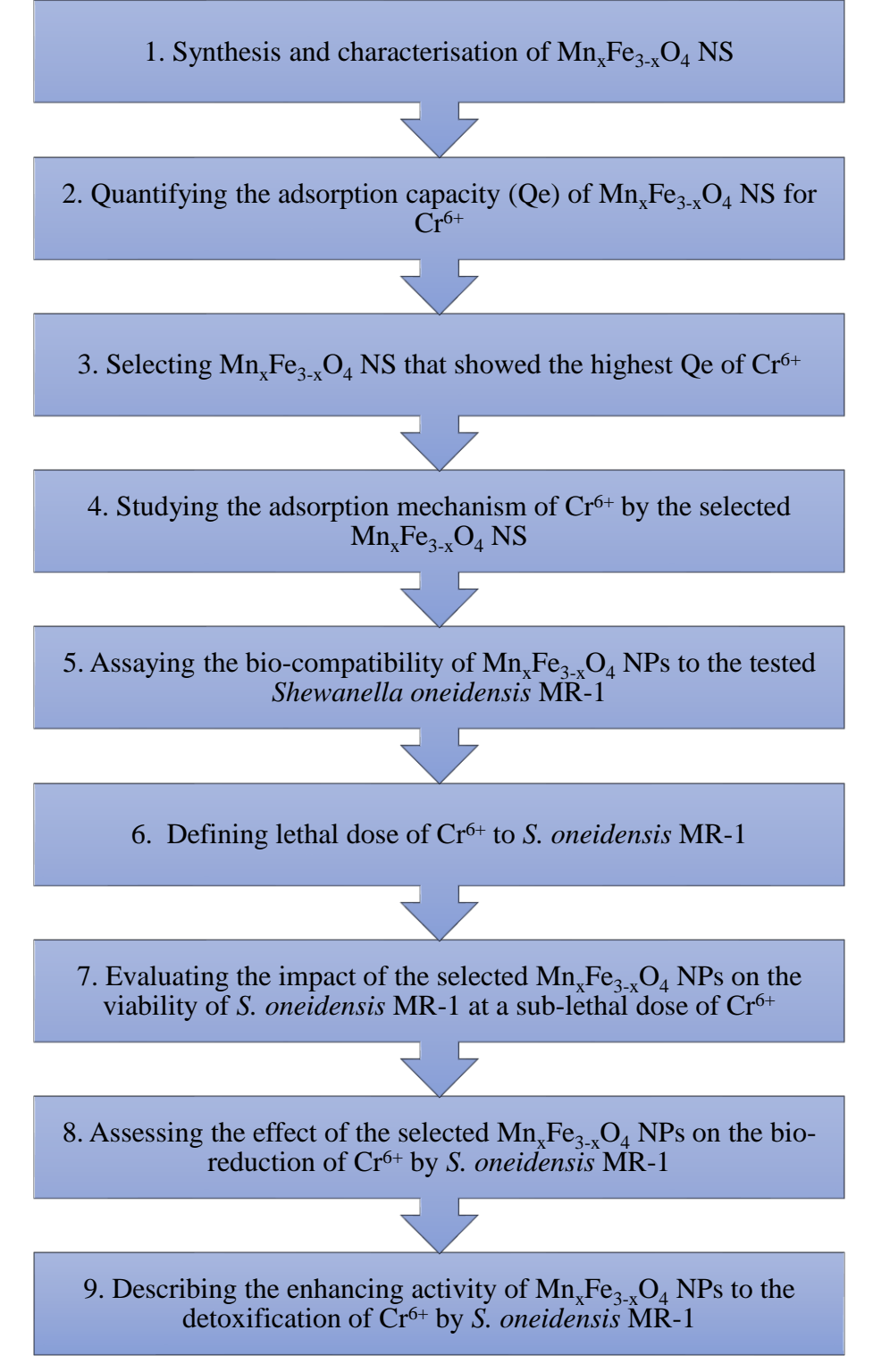


Figure 2: Flowchart of the experimental activities in the current PhD.

Chapter 2. Synthesis and characterisation of spherical and flower-like manganese ferrite nanostructures

2.1 Introduction

Nanostructures (NS) have become common and efficient materials for the remediation of pollutants from effluents. Controlling the morphology, crystallinity and chemical structure is crucial for benefiting nano-sized materials in environmental applications. So, a reproducible, simple and cheap protocol for synthesising NS is a bottleneck in the scaling-up process. Several methods were reported for preparing manganese ferrite (Mn_xFe_{3-x}O₄) NS. Several methods were reported for preparing manganese ferrite (Mn_xFe_{3-x}O₄) NS. Several method for synthesising such NS is easy to use, cheap and has a potential for scalability. In addition, the polyol solvothermal method can control the chemical composition, and morphology of Mn_xFe_{3-x}O₄ NS. Chapter 2 reported the synthesis and characterisation of Mn_xFe_{3-x}O₄ NPs and nanoflowers (NFs) using the polyol solvothermal method. The impact of the oxidation states of Mn precursors, variation in Mn doping levels and synthesis conditions, including temperature and time of synthesis, on the chemical structural and morphological characteristics of MnFe₂O₄ NPs have been investigated.

2.2Materials and methods

2.2.1 Chemicals for NS preparation and characterisation

All chemicals that were consumed during the present project were used as received without further purification. Absolute ethanol (C₂H₅ OH, 99.9%) were purchased from HaymanKimia, UK. Acetone (C₃H₆O, >99%) and hydrochloric acid (HCl, 34%) were bought from VWR Chemicals, UK. Anhydrous sodium hydroxide (NaOH, 98%), ferric acetylacetonate (Fe(acac)₃, 99.9%), iron standard for Inductively Coupled Plasma (ICP) TraceCERT® where the concentration of Fe in nitric acid (HNO₃) was 1000 mg/L, manganese(II) acetylacetonate (Mn(acac)₂, 99.9%), manganese(II, III) oxide (Mn₃O₄, 97%), manganese(III) acetylacetonate (Mn(acac)₃, 99.9%), manganese standard for ICP TraceCERT® (1000 mg/L in HNO₃), HNO₃ (70%), potassium bromide (KBr, FTIR grade 99%), tetra-ethylene glycol (TEG, 99%), and tri-sodium citrate dihydrate (Na₃C₆H₅O₇.2H₂O) were obtained from Sigma-Aldrich (UK).

2.2.2 Synthesis of Mn_xFe_{3-x}O₄ NS

Mn_xFe_{3-x}O₄ NPs were prepared by a polyol solvothermal synthetic procedure^{159,163} with some modifications. The influence of the oxidation number of Mn precursors, *i.e.*, Mn(acac)₂ vs Mn(acac)₃, the molar ratio between [Mn precursor] to [Fe(acac)₃] and reaction temperature on the properties of NPs were studied. Based on previous experience from our research group, using 15 wt%/vol as a total dissolved precursor concentration resulted in NPs with narrow size distribution.¹⁷²

A. Synthesis of $Mn_xFe_{3-x}O_4$ NPs

The desired amounts of precursors with ratios [Mn(acac)_{2 or 3}] / [Fe(acac)₃] equal to 0, 0.14, 0.33, 0.6, 1, 1.66 and 3 were mixed in 20 mL of TEG as a solvent. The mixture was homogenised by vortexing for 10 min, then sonicated for 30 min, and then transferred into a 45 mL Teflon chamber enclosed in a stainless-steel autoclave. The autoclave was placed in an oven (Memmert, model UFP400) at room temperature, and the reaction temperature was raised for 30 min to 250 °C, which was maintained for 6 h. Only for the ratio [Mn(acac)_{2 or 3}] / [Fe(acac)₂] equal to 0 and 0.33, the synthesis conditions include ageing time from 2 to 24 h at 250 °C, and synthesis temperature at 200 °C for 6h was assayed. The resulting black dispersion was collected using a magnet and washed with 1:10 v/v of acetone, followed by ethanol and water 3 times for each solvent. Then, the nanomaterials were ready for characterisation and functionalisation.

B. Preparation of $Mn_xFe_{3-x}O_4$ NFs

 $Mn_xFe_{3-x}O_4$ NFs were prepared following the above-described protocol for $Mn_xFe_{3-x}O_4$ NPs and literatures¹⁷³ with some modifications. The autoclave was inserted in the oven, which was heated to 200 °C for 6 h, and the tested ratios between precursors [Mn(acac)₃] / [Fe(acac)₃] were 1 and 3 while [Mn(acac)_{2 or 3}] / [Fe(acac)₃] ratio of 7 was kept at 250 °C for 6 h.

2.2.3 Characterisation of Mn_xFe_{3-x}O₄ NS

For the prepared nanomaterials, the shape and diameter (D_{TEM}) of the core were determined by JEOL JEM 1200-EX Transmission Electron Microscopy (TEM) operating at an acceleration voltage of 120 kV. The crystal phase of $Mn_xFe_{3-x}O_4$ NPs and NFs and their average crystallite size (D_{XRD}) were analysed by PANalytical XPERT PRO MPD X-Ray Diffractometer (XRD). The X-Ray radiation source of XRD was Co k_α (λ = 1.789 Å), and an X'Celerator detector operated at 40 kV and 40 mA. The crystalline phases were identified using the International Centre for Diffraction Data Powder Diffraction File (ICDD PDF) database. The D_{XRD} was calculated using Scherrer's equation at the most intense X-ray peaks (311).

The elemental analysis of Mn_xFe_{3-x}O₄ was characterised by the Inductively Coupled Plasma Atomic Emission spectrometer (ICP-AES, Optima 3100 XL Perkin Elmer). The capping agent on the surface of the prepared NS was assayed using an Attenuated Total Reflectance-Fourier Transform-Infrared Spectroscopy (ATR-FTIR, Perkin Elmer Spectrum 100 instrument with a Ge/Ge universal ATR). The samples were air-dried at room temperature overnight to yield a fine powder to be placed on an ATR crystal. The measurement window for the recorded spectra was with a resolution of 2 cm⁻¹ in the range 4000 – 600 cm⁻¹ using 40 scan accumulation.

2.2.4 Functionalisation of Mn_xFe_{3-x}O₄ NS

A. Ligand exchange of TEG by tri-sodium citrate

To exchange the initial ligand TEG, 1 mL of the dispersions of the prepared nanomaterials and 10 mL of 1 M aqueous tri-sodium citrate solution were mixed for 48 h at room temperature under stirring. Immobilisation of citrate on the surface of the commercially available Mn₃O₄ (Mn-rich and Fe-free ferrite control) was obtained by dispersing 0.1 g of the metal oxide in 10 ml of 1 M aqueous tri-sodium citrate solution under similar mentioned conditions. An external magnet collected the functionalised NS. NS were washed with acetone 3 times and ethanol 3 times before being dispersed in deionised water.

B. Surface characterisation of $Mn_xFe_{3-x}O_4$ NS

The capping agents on the surface of NS were elucidated using an ATR-FTIR spectrometer with wavenumbers within a range from 4000 to 600 cm⁻¹ of a 2 cm⁻¹ resolution and 40 scan accumulation. The hydrodynamic diameter (D_{HD}) of citrate-functionalised NPs was quantified by Dynamic Light Scattering (DLS) measurements using a Nanosizer ZS instrument (He–Ne 633 nm laser) from Malvern Instruments Ltd, Worcestershire, UK). The ζ -potentials of the functionalised NPs were determined using a disposable capillary cell (DTS1070) at 25 °C by DLS.

2.2.5 Statistical analysis

All experiments were done in triplicates, and all statistical analyses were done via OriginLab software. Log-normal function fitted the distribution of D_{TEM} . Normal distribution function described the data sets of D_{XRD} , X_{ICP} , D_{HD} and ζ -potential. The statistical Students t-test was used to assess how the statistical difference between $[Mn(acac)_{2 \text{ or } 3}]$ / $[Fe(acac)_3]$, the oxidation state of Mn precursor and synthetic conditions (temperature and time) of the selected $Mn_x^{2+\text{ or } 3+}Fe_{3-x}^{3+}O_4$ NPs affected D_{TEM} , D_{XRD} , X_{ICP} , D_{HD} and ζ -potential. The significance level was described as a calculated probability (P) < 0.05 (*) and P < 0.01 (**).

2.3 Results and discussion

2.3.1 Synthesis of nanomaterials

The present study synthesised Mn_xFe_{3-x}O₄ NPs and NFs using a polyol solvothermal method. In polyol synthesis, metal precursors are reduced by alcohols (polyols) which act as an appropriate capping agent, solvent and reducing agent at a high boiling temperature. Then the formed metal nuclei grow and controllably coalesce together to produce the desired particles.¹⁷⁴ The solvolysis of the metal precursor involved a ligand exchange. TEG replaced the acetylacetonate of the metal precursor generating metal carboxylate.¹⁷⁵ The second step is a condensation reaction in which carboxylate reacts with iron resulting in the formation of an oxo-bridge between metal (metal-oxygen-metal clusters) and ultimately resulting in the formation of metal oxide nanocrystals.¹⁷⁵

2.3.2 Characterization of Mn_xFe_{3-x}O₄ NPs

A. Morphology of Mn_xFe_{3-x}O₄ NPs

The prepared $Mn_xFe_{3-x}O_4$ NPs using precursor ratios $0 \le [Mn(acac)_2 \text{ or } 3]$ / $[Fe(acac)_3] \le 3$ had nearly spherical shapes and were well dispersed, with sufficient interparticle distances as shown in *Figure 3* and *Figure 4*. D_{TEM} particle size ranged from 5 to 12.5 nm with polydispersity indexes between 0.14-0.21 except for 0.66 and 3 for the case of $[Mn(acac)_2 \text{ or } 3]$ / $[Fe(acac)_3]$ as represented in *Figure 5*.

The doping level of Mn had an insignificant change in the D_{TEM} of Mn_xFe_{3-x}O₄ NPs compared to undoped Fe₃O₄ NPs (*Figure 5 A*). In the case of using the divalent Mn

precursor, an insignificant change in D_{TEM} when increasing the ratio of precursors in agreement with similar trends as was reported by Garcia-Soriano et al..¹⁷⁶

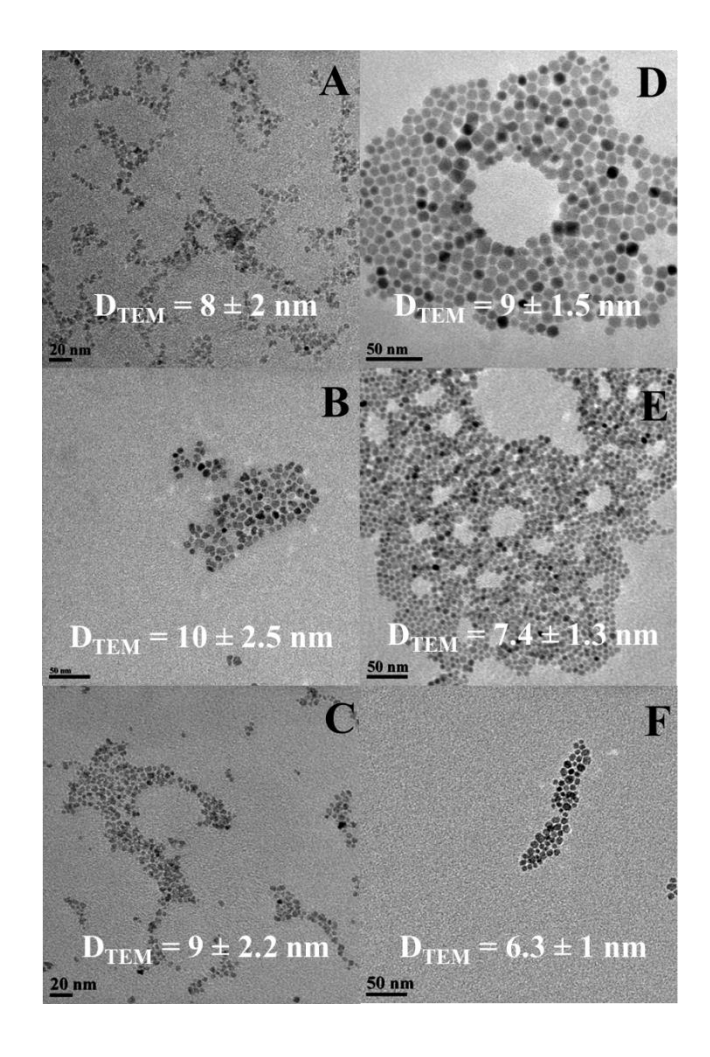


Figure 3. TEM images for the spherical (A) undoped Fe_3O_4 NPs, (B) $Mn_xFe_{3-x}O_4$ of precursor ratio $[Mn(acac)_2]$ / $[Fe(acac)_3] = 0.33$, (C) $[Mn(acac)_3]$ / $[Fe(acac)_3] = 0.33$ prepared at 200 °C as reaction temperatures, (D) undoped Fe_3O_4 NPs and (E & F) $Mn_xFe_{3-x}O_4$ NPs prepared with the same precursor ratio but at 250 °C.

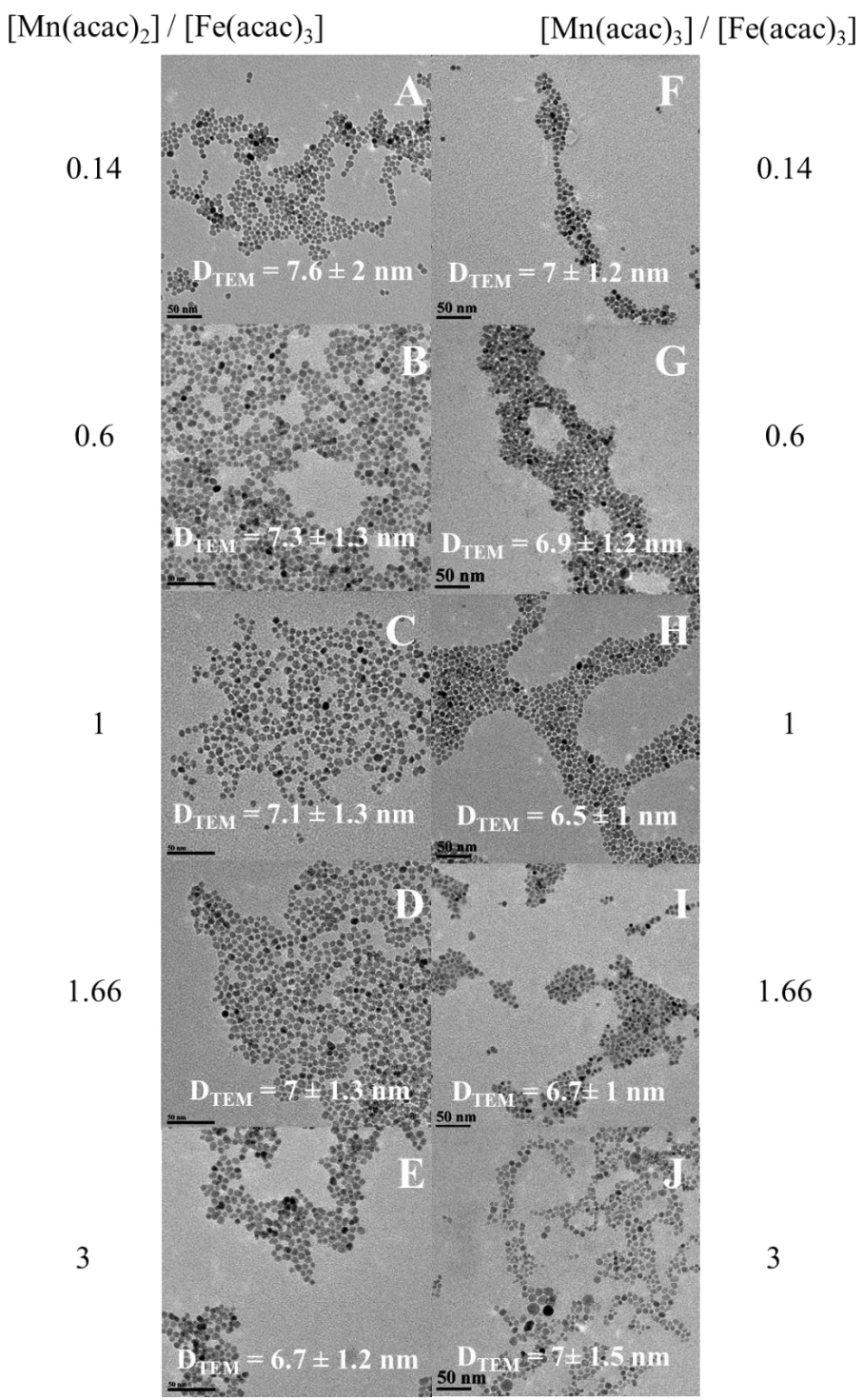


Figure 4: TEM images of spherical $Mn_xFe_{3-x}O_4$ nanoparticles (NPs) prepared by solvothermal method at 250 °C. The precursor concentration ratio of (A-E) [Mn(acac)₂] / [Fe(acac)₃] and (F-J) [Mn(acac)₃] / [Fe(acac)₃] respectively were 0.14, 0.6, 1, 1.66 and 3.

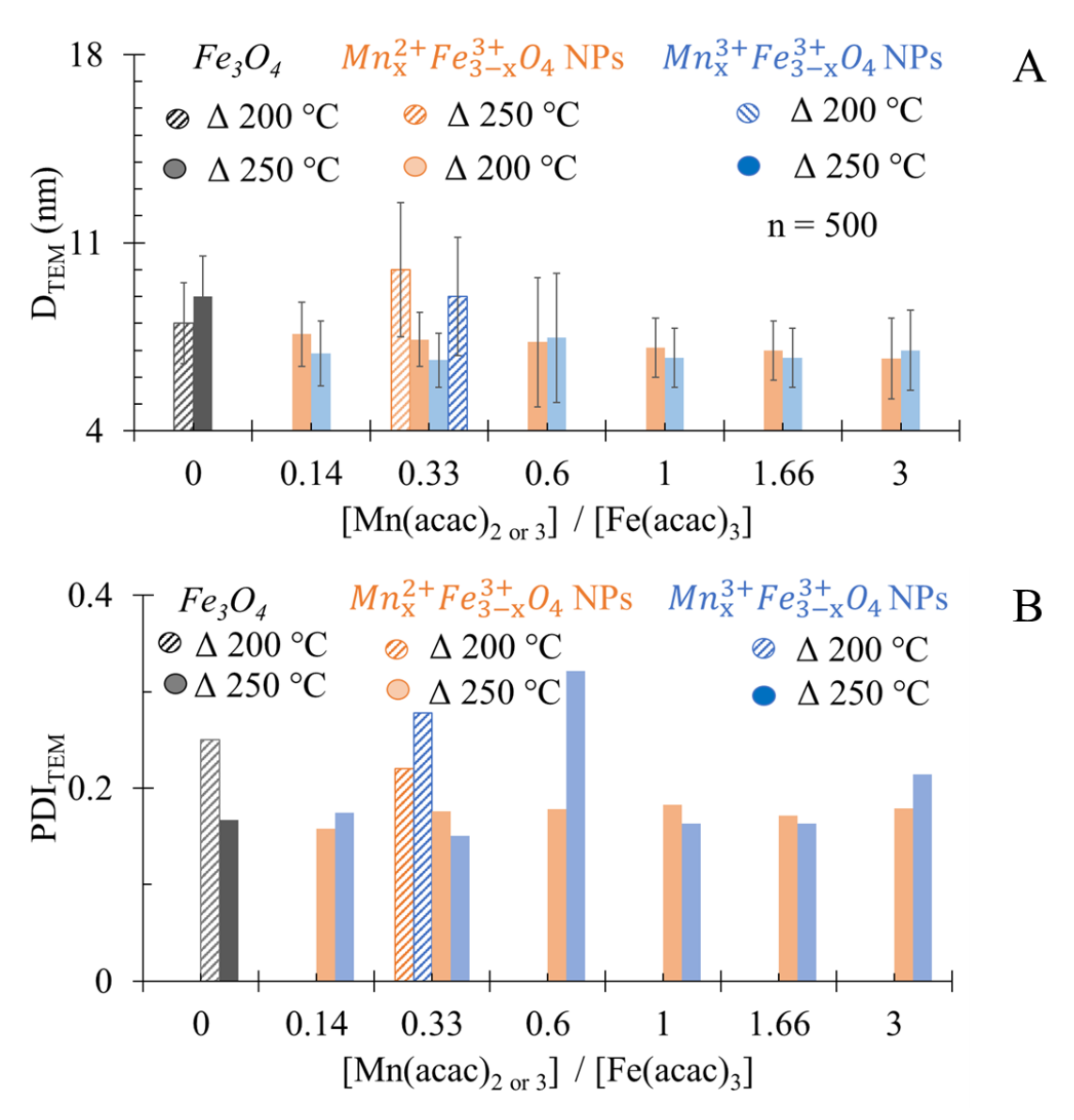


Figure 5: Impact of reaction temperatures (200 vs 250 °C) on (A) D_{TEM} of $Mn_xFe_{3-x}O_4$ NPs prepared from $0 \le [Mn(acac)_{2 \text{ or } 3}] / [Fe(acac)_3] \le 3$. (B) Polydispersity index (PDI) of NPs diameters varied with precursor concentration ratios ($0 \le [Mn(acac)_{2 \text{ or } 3}] / [Fe(acac)_3] \le 3$) calculated from TEM.

B. Crystal structure of Mn_xFe_{3-x}O₄ NPs

XRD of Fe₃O₄ NPs and Mn_xFe_{3-x}O₄ NPs that were prepared at a temperature of 200 °C are shown in *Figure 6*. The undoped Fe₃O₄ NPs were formed at 250 °C with an ageing time of 6 h. XRD measurements of such particles are shown in Table 1.

The main peaks at the diffractogram of these NPs appear at 21.5° (111), 35.1° (220), 41.4° (311), 50.4° (400), 62.8° (422), 67.3° (511), and 74.1° (440). These peak locations matched ICDD PDF card No. 01-086-2344, revealing the formation of iron oxide (FeO-Fe₂O₃). 172,177,178

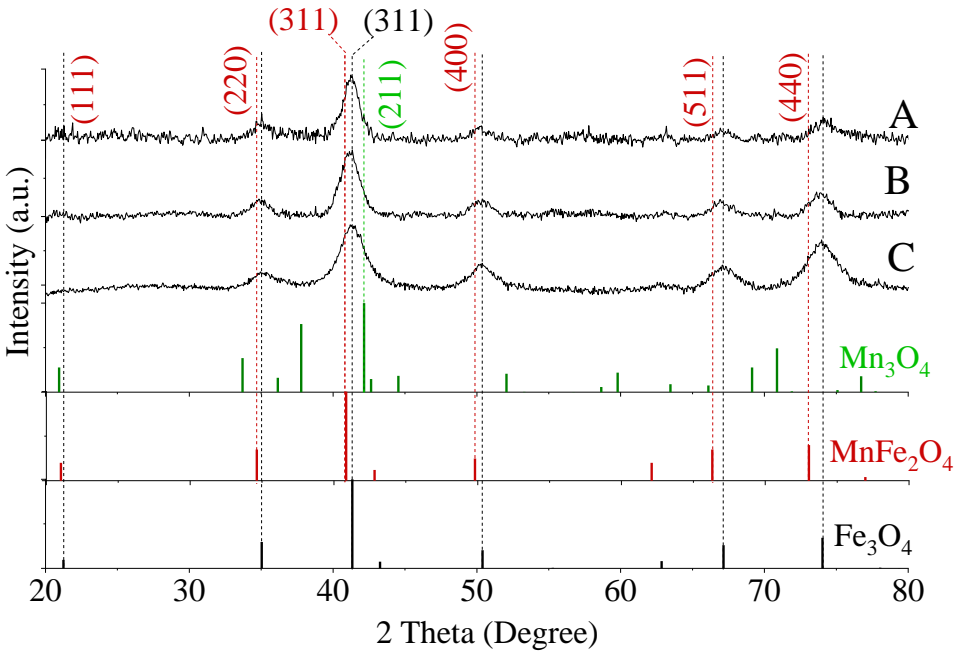


Figure 6: XRD patterns of NPs prepared at 200 °C where (A) undoped Fe_3O_4 NPs, (B) $[Mn(acac)_2]$ / $[Fe(acac)_3]$ was 0.33, (C) $[Mn(acac)_3]$ / $[Fe(acac)_3]$ was 0.33. The reference ICDD were Mn_3O_4 (PDF card no. 01-080-0382), $MnFe_2O_4$ (PDF card no 00-010-0319) and Fe_3O_4 (PDF card no 01-089-0688).

Table 1: Summary of 311 peak positions and crystal size $(D_{XRD})^a$ determined by XRD of $Mn_xFe_{3-x}O_4$ NPs prepared at 250 °C.

[Mn(acac) _{2 or 3}] / [Fe(acac) ₃]	Mn(acac) ₂		Mn(acac) ₃	
	2θ (311)	D _{XRD} (nm)	2θ (311)	D _{XRD} (nm)
0.14	41.33	7 ± 1	41.01	7 ± 1
0.33	41.4	7 ± 0.5	41.06	6 ± 1*
0.6	41	7 ± 1	41.07	7.5 ± 1
1	41.1	7 ± 1	41.01	6.5 ± 1*
1.66	41	6.5 ± 1*	40.92	5 ± 1**
3	41	6.5 ± 1.5*	40.87	5.5 ± 1.5**
7	-	-	-	-

 $^aD_{XRD}$ was presented as (mean \pm standard deviation) of 3 independent synthesis experiments, and $^*p < 0.05$ and $^*p < 0.01$ showed the statistical confidence levels by comparing the crystal size with Fe₃O₄ NPs (9 \pm 1.3 nm) synthesized in the same conditions.

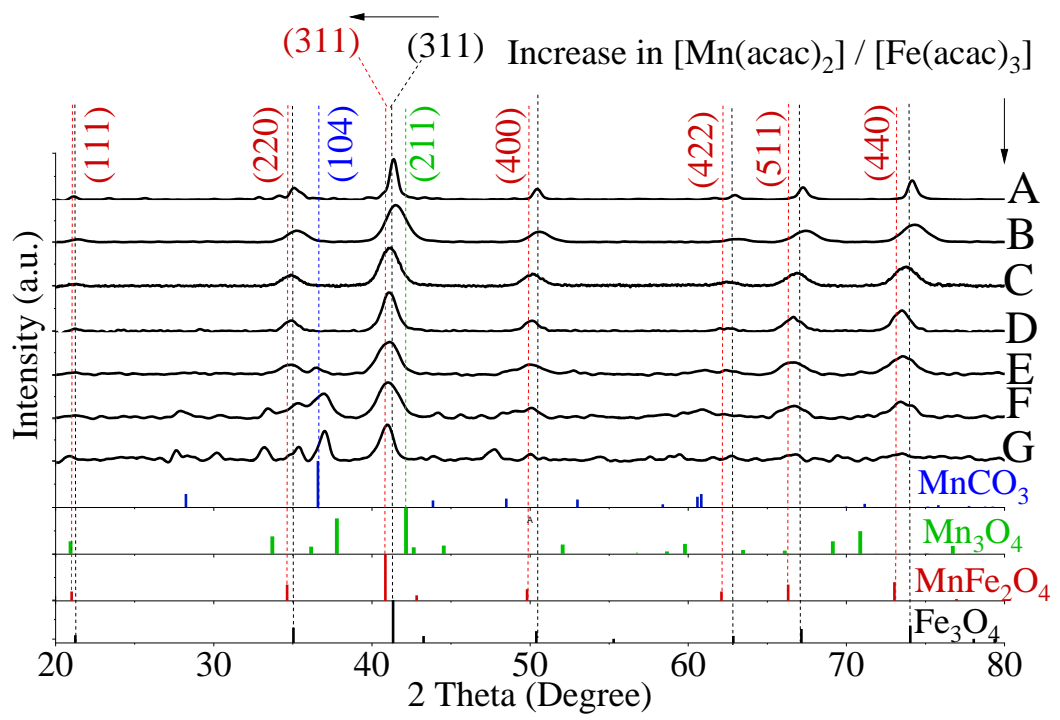


Figure 7: XRD patterns for fcc lattice of Fe_3O_4 (A) and $Mn_xFe_{3-x}O_4$ NPs where $[Mn(acac)_2]$ / $[Fe(acac)_3]$ were 0.14 (B), 0.33 (C), 0.6 (D), 1 (E), 1.66(F), 3 (G). The horizontal arrow pointed out the shifting in the peak of 311 from the reference Fe_3O_4 (PDF card no 01-089-0688) towards the lower diffraction angle of $MnFe_2O_4$ (PDF card no 00-010-0319) in response to the increase in $[Mn(acac)_2]$ / $[Fe(acac)_3]$. A secondary phase of $MnCO_3$ (Reference ICDD PDF card no. 00-044-1472) was found for NPs prepared from $(1 \le [Mn(acac)_2 \text{ or }_3]$ / $[Fe(acac)_3] \le 3)$ (E-G). The synthesis temperature for all NPs was 250 °C. The vertical arrow indicates the gradual increase in $[Mn(acac)_2]$ / $[Fe(acac)_3]$ from (A-G) Mn_3O_4 (PDF card no. 01-080-0382).

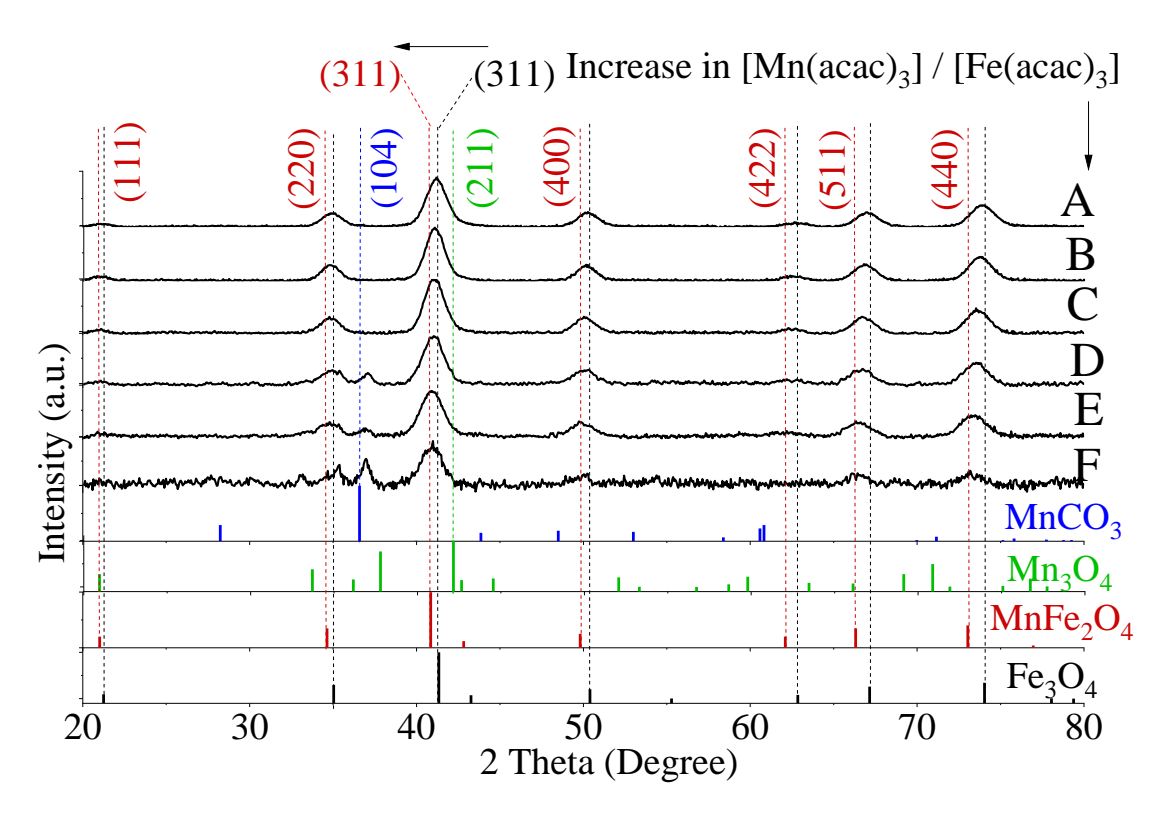


Figure 8: XRD patterns of $Mn_xFe_{3-x}O_4$ NPs where $[Mn(acac)_3]$ / $[Fe(acac)_3]$ were (A) 0.14, (B) 0.33, (C) 0.6, (D) 1 (E) 1.66 (F) 3. The reference ICDD were Mn_3O_4 (PDF card no. 01-080-0382), $MnFe_2O_4$ (PDF card no 00-010-0319) and Fe_3O_4 (PDF card no 01-089-0688). A secondary phase appears to be present for NPs prepared from (1 \leq $[Mn(acac)_2 \ or \ 3]$ / $[Fe(acac)_3] \leq 3$) (D-F), which was identified as $MnCO_3$ (Reference ICDD PDF card no. 00-044-1472). Perpendicular and horizontal arrows showed the gradual increase in $[Mn(acac)_3]$ / $[Fe(acac)_3]$ from (A-F) and the shifting in the peak of 311 from the reference Fe_3O_4 towards the lower diffraction angle of $MnFe_2O_4$, respectively.

Incorporating Mn ions into the Fe₃O₄ lattices as substitutional atoms were then implemented from either Mn(acac)₂ or Mn(acac)₃. By increasing the ratio of [Mn(acac)₂ or $_3$] to [Fe(acac)₃], a slight shift of the peaks towards a lower 2 θ value (closer to the reference peak of MnFe₂O₄) was observed at XRD measurements (*Figure 7* and *Figure 8*). Using Mn(acac)₃ caused a relocation of XRD peak positions closer to the reference peak positions of MnFe₂O₄ (2 θ = 40.8°), as shown in *Figure 8*. These repositioning of peaks can be attributed to the further inclusion of Mn³⁺ into the spinel iron oxide lattice due to the similar ionic radii between Mn³⁺ and Fe³⁺ (0.64 Å¹⁵⁹ for both), which are smaller than Mn²⁺ (0.80).¹⁵⁹

The slight broadening in the peaks with an increase in the Mn precursor concentration implies a change in crystal size, 179 , which was supported by the Full-Width Half Maximum (FWHM) of the most intense X-ray peaks (311), as summarised in *Table 1*. Using $0.33 \leq [\text{Mn}(\text{acac})_{2 \text{ or } 3}] / [\text{Fe}(\text{acac})_{3}] \leq 0.6$ resulted in the formation of MnFe₂O₄ with a face-centred cubic crystal (fcc) as verified by XRD patterns and presented in *Figure 7 B-D* and *Figure 8 A-C*.

The XRD peaks matched with ICDD PDF card no. 00-010-0319 of MnFe₂O₄. The lattice planes correspond to the cubic spinel structure of MnFe₂O₄ (ICDD card no. 00-010-0319). For NPs prepared using $1 \le [\text{Mn}(\text{acac})_2] / [\text{Fe}(\text{acac})_3] < 7$ in *Figure 7E-G*, the distinct additional peaks at 20 values of 36.8, 36.9° and 37.0°, respectively, indicated the formation of a secondary phase that was indexed to the (104) Miller plane of MnCO₃ (ICDD card no. 00-044-1472). In *Figure 7 F & G*, peaks attributed to the TEG molecule appeared at 20 equal to 27.8° and 27.6°, respectively, as shown in the XRD of the TEG compound alone before and after thermal treatment (*Figure 9*) as reported by Vamvakidis

et al.¹⁵⁹ as well as Khanna and Verma.¹⁸⁰ Peaks were noticed at 30.2° and 33.1°, which were assigned to MnOOH (ICDD PDF card no. 01-074-1631, data are not shown), and MnO₂ (ICDD PDF card no. 00-024-0735, data are not shown) correspondingly. The presence of multiple phases of Mn oxides/hydroxides was attributed to the formation of H₂O and Mn₂O₃ (the products of thermal decomposition of Mn(acac)₂),¹⁸¹ which can lead to oxidation of Mn³⁺ into Mn⁴⁺ and hydroxylation of Mn³⁺ oxides.

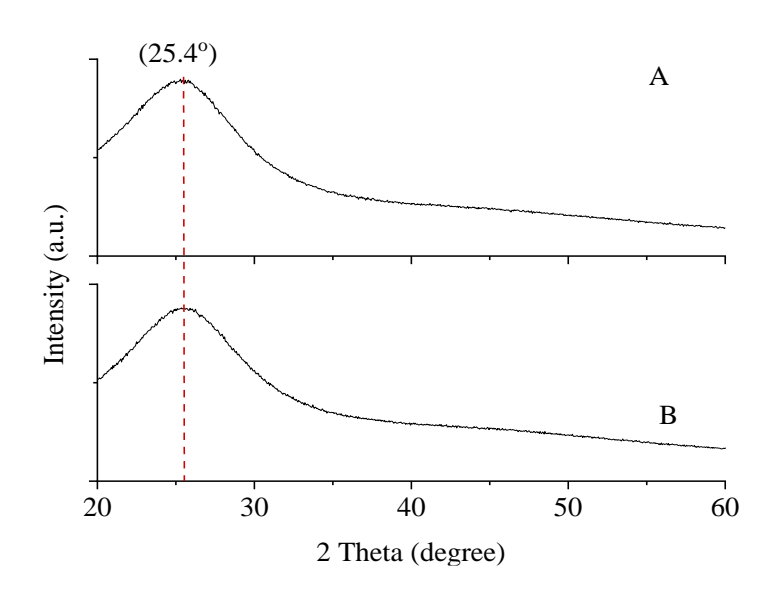


Figure 9: XRD patterns of TEG (A) before and (B) after thermal treatment at 250 °C for 6 h in the autoclave.

The increase in the [Mn(acac)_{2 or 3}] / [Fe(acac)₃] leaded to a slight broadening in the 311 peaks, which indicated a modification of the crystal size,¹⁷⁹ as determined by measuring the FWHM and summarised in *Table 1*. This could be explained by substituting Fe atoms with Mn atoms of a smaller cationic radius.^{163,182} The calculated crystal size obtained from XRD of samples (6.5-7 and 5-7.5 nm) for NPs prepared from divalent and trivalent Mn precursors, respectively, see PDI of crystal size in *Figure 11*)

were within the range of the average particle size derived from TEM. Therefore, these NPs were considered single crystallite. However, the XRD analysis indicated the presence of MnCO₃ for NPs of precursor ratios in the range of $1 \le [Mn(acac)_{2 \text{ or } 3}] / [Fe(acac)_3] \le 3$, the crystal sizes determined by XRD were also within the diameter range observed by TEM.

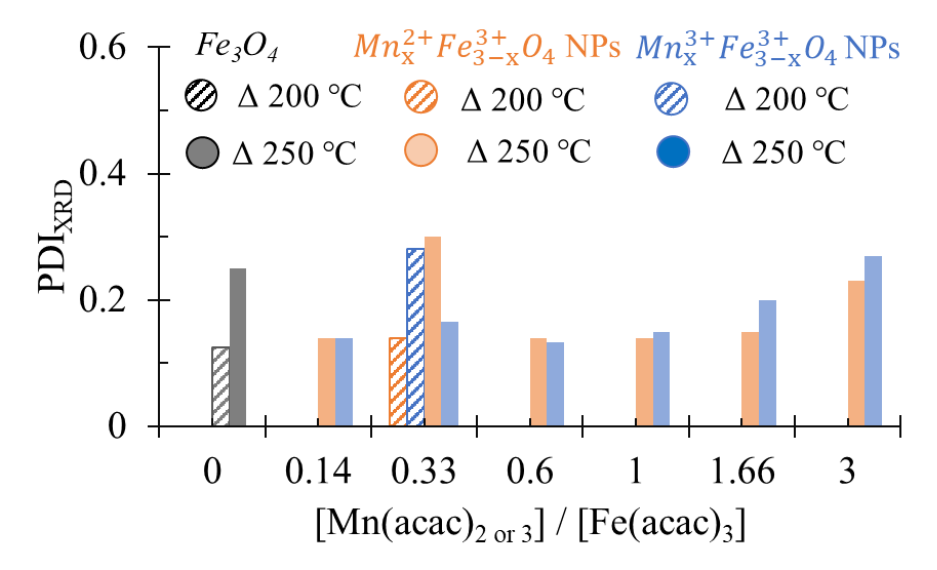


Figure 10: Polydispersity index (PDI) of D_{XRD} varied with precursor concentration ratios calculated from XRD at the most intense peak of (311) at annealing temperature (200 vs 250 °C).

2.3.3 Characterisation of Mn_xFe_{3-x}O₄ NFs

The preparation of $Mn_xFe_{3-x}O_4$ NFs was prepared using a modified solvothermal method. The morphology was controlled by varying the ratios between $[Mn(acac)_3]$ / $[Fe(acac)_3]$ precursors and the reaction temperature, as shown in *Figure 11A* and *B* and $[Mn(acac)_2]$ / $[Fe(acac)_3]$ in *Figure 11 C*.

A. Morphology of Mn_xFe_{3-x}O₄ NFs

At 200 °C, the polyol solvothermal method resulted in a well-defined flower-like structure with a narrow size distribution, as shown in *Figure 11 A & B*. The morphology of Mn_xFe_{3-x}O₄ NFs (*Figure 11 B*) matched the CoFe₂O₄ NFs, reported by Fu et al., but ours were smaller size (D_{TEM} of M_xFe_{3-x}O₄ NFs = 60 ± 12 nm vs D_{TEM} of CoFe₂O₄ NFs = 164.8 ± 20.7 nm). The smaller diameter of Mn_xFe_{3-x}O₄ NFs than the reported CoFe₂O₄ NFs by 2.75 fold can be attributed to using sodium hydroxide during the solvothermal preparation of CoFe₂O₄ NFs, ¹⁷³ which accelerated the hydrolysis of the precursors and promoted the formation of larger oxide clusters. TEM analysis of NPs synthesised at 250 °C with a ratio [Mn(acac)₃] / [Fe(acac)₃] equal to 7 showed the formation of aggregated crystalline particles in clusters (*Figure 11 C*).

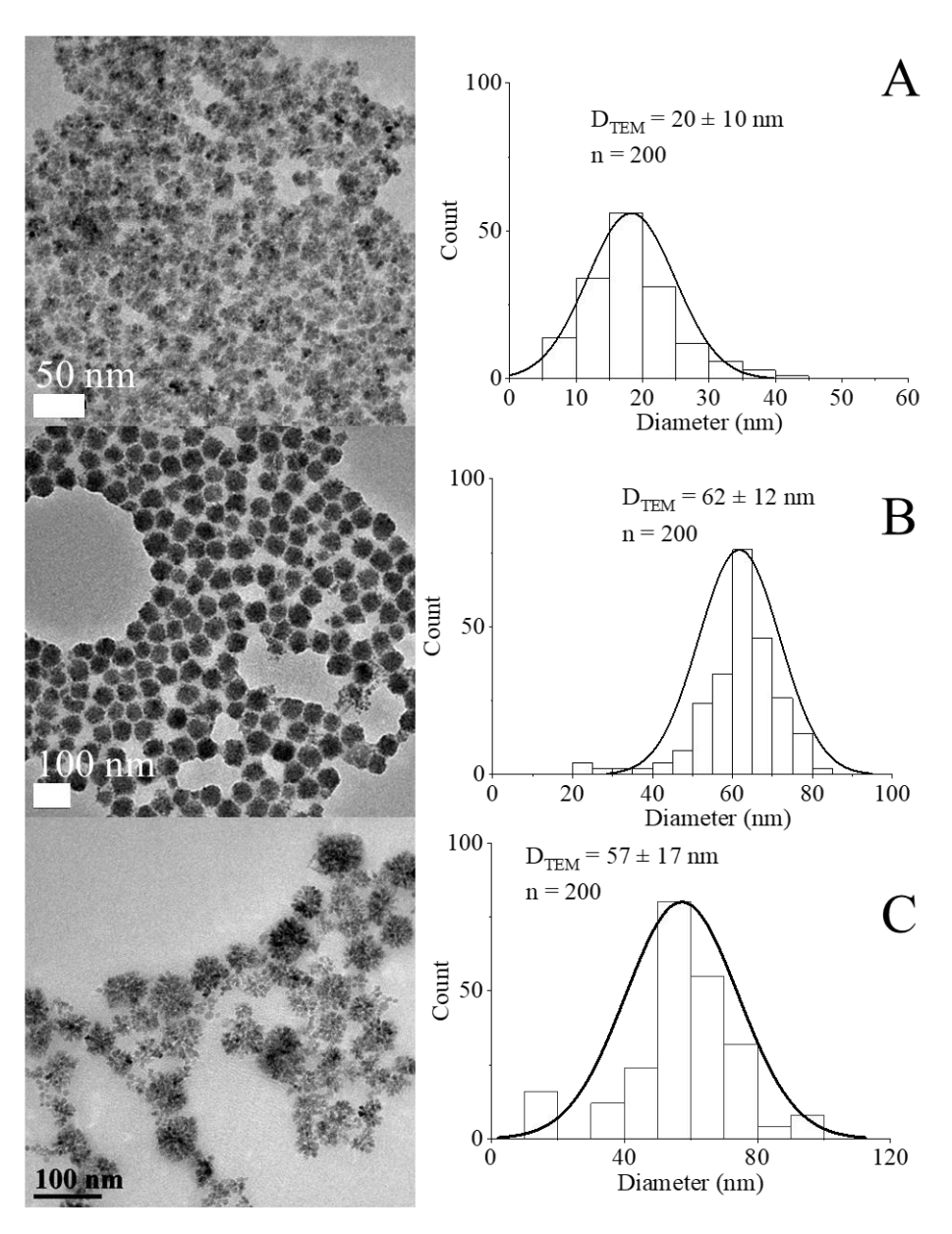


Figure 11: TEM images and histograms for D_{TEM} of NFs prepared from [Mn(acac)₃] / [Fe(acac)₃] = (A & B) 1 & 3 at synthesis temperature 200 °C, respectively (C) 7 at synthesis temperature 250 °C.

B. Crystal structure of Mn_xFe_{3-x}O₄ NFs

Figure 12 showed diffraction patterns of Mn_xFe_{3-x}O₄ with crystal size of NFs were 6-8 nm. The small crystal size compared to D_{TEM} of NFs (*Figure 11*) implied the formation of primary nanocrystals, which do not grow significantly. The primary nanocrystals aggregated into larger secondary particles, as shown in *Figure 11A-C* and as described by Gavilan et al.¹⁸⁴ The generation of MnCO₃ accelerated the hydrolysis of the precursors and resulted in the formation of oxide clusters.¹⁷³ In our case, nano-clusters were prepared in a single step, including the synthesis of nanoparticles and their coalescence. Shifting in the peak of 311 from the reference Fe₃O₄ (PDF card no 01-089-0688) towards the lower diffraction angle of MnFe₂O₄ (PDF card no 00-010-0319) in response to the increase in [Mn(acac)₃] / [Fe(acac)₃] from 1 to 3 was observed and an indicator for inclusion of Mn ions into the Fe₃O₄ lattices.

In the case of preparing NPs with a [Mn(acac)₃] / [Fe(acac)₃] ratio equal to 7 at 250 °C, the XRD pattern shows the development of a polycrystalline material corresponding to a mixture of phases. As shown in

Figure 12 D, the peaks at 36.9° (104) and 27.7° (102) diffraction peaks were indexed to MnCO₃ (JCPDS card no. 00-044-1472). The 2 θ Bragg reflections at 21.5° (111), 35.4° (220), 41.0° (311), 50.1° (400), 66.6° (511), and 73.5° (440) confirmed the formation of MnFe₂O₄ (JCPDS card no. 00-010-0319). A peak at 27.5° was assigned to TEG, ¹⁸⁰ which was supported by our results, as shown in *Figure 9*. Also, peaks appeared

at 20 equal to 30.1°, 33.2° and 35.3° were related to MnOOH (JCPDS card no. 01-074-1631) and MnO₂ (JCPDS card no. 00-024-0735). Our results revealed that the ratio increase between the used precursors led to the formation of nano-clusters of $Mn_xFe_{3-x}O_4$, which matched what was reported for $Mn_xFe_{3-x}O_4^{185}$ and other ferrites by the solvothermal method.¹⁸⁶

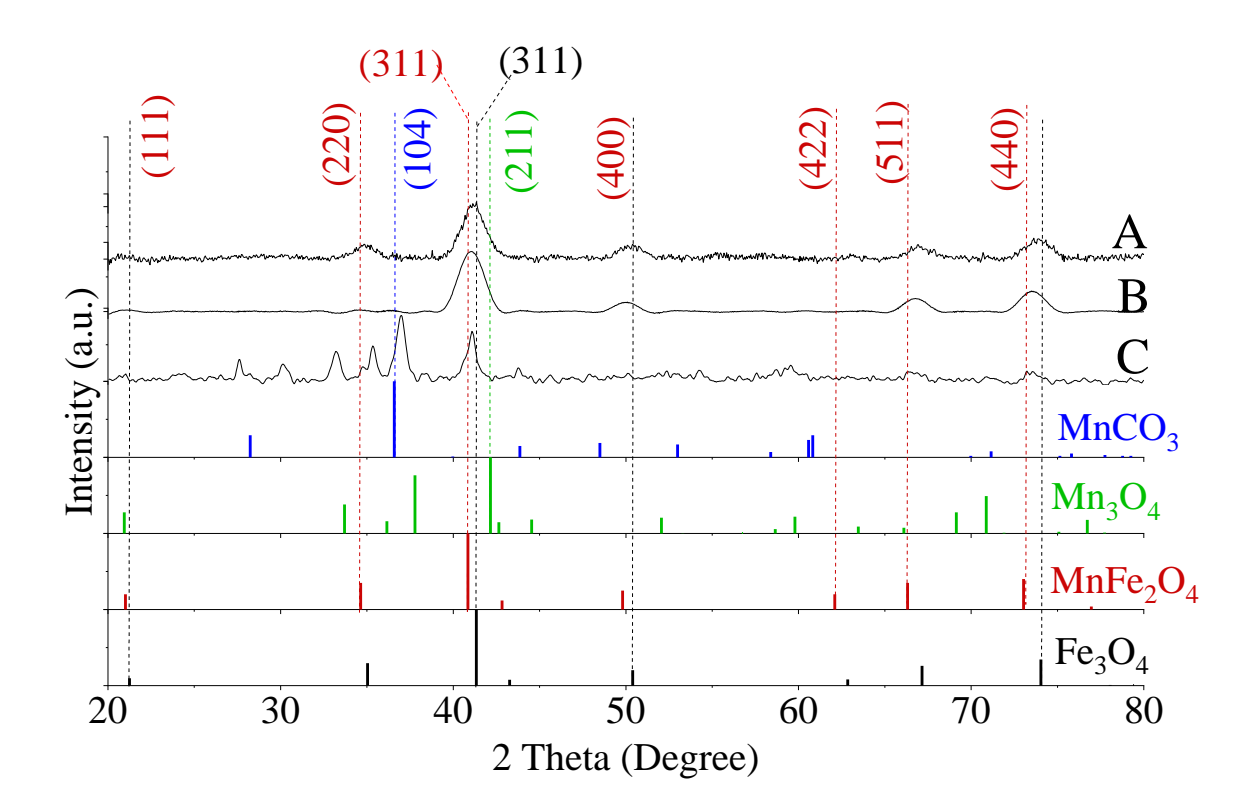


Figure 12: XRD patterns of $Mn_xFe_{3-x}O_4$ NFs prepared from $[Mn(acac)_3]$ / $[Fe(acac)_3]$ ratio equal to (A) 1 and (B) 3 at 200 °C, (C) 7 at 250 °C. A secondary phase-matched $MnCO_3$ (Reference ICDD PDF card no. 00-044-1472) was found for NFs prepared from a precursor equal to 7 at 250 °C. No detected peaks matched Mn_3O_4 (PDF card no. 01-080-0382).

When [Mn(acac)₂] / [Fe(acac)₃] was 7, the observed XRD peaks of the solvothermal-produced material at 250 °C cannot be assigned to well-established crystal phases of ferrite materials (*Figure 13*). Hence, this sample was not selected for further analysis since it could not offer any crucial insights into metal substitution. The inability of nanocluster formation using [Mn(acac)₂] / [Fe(acac)₃] equal to 7 can be attributed to the thermal stability of Mn(acac)₂, which limits its decomposition.¹⁸¹

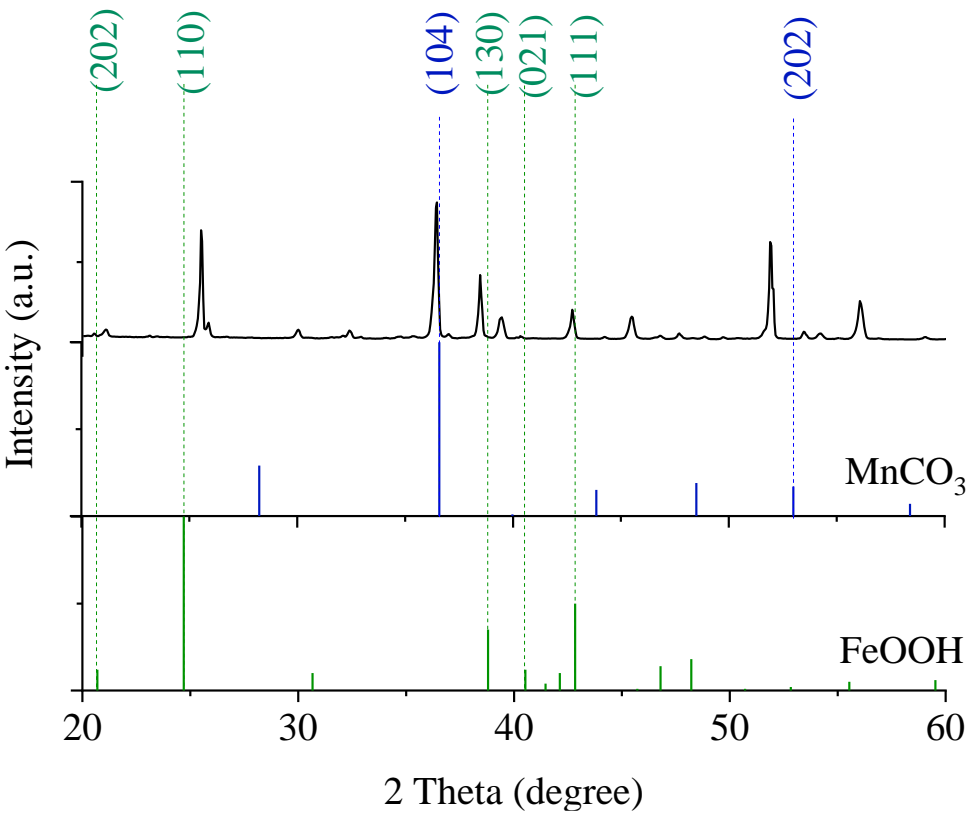


Figure 13: XRD patterns of a produced sample where [Mn(acac)₂] / [Fe(acac)₃] was 7.

Reference JCPDS card no. 00-044-1472, 00-029-0713, for MnCO₃, FeOOH, respectively.

2.3.4 Growth of the selected Mn_xFe_{3-x}O₄ NPs over time

 $Mn_xFe_{3-x}O_4$ NPs that were prepared of precursor ratios $[Mn(acac)_2]$ / $[Fe(acac)_3]$ = 0.33 at a synthesis temperature of 250 °C for 6h showed the best adsorption capacity for hexavalent chromium (Cr^{6+}) as explained in Chapter 3 later. So, these NPs were selected to study their growth over 2 h to 24 h under similar synthesis conditions.

A. Morphology of selected $Mn_xFe_{3-x}O_4$ NPs over time

Spherical Fe₃O₄ NPs and Mn_xFe_{3-x}O₄ NPs were synthesised using the polyol solvothermal method with a size range from 7 to 23 nm and 6.5 to 15 nm, respectively, over a reaction duration from 2 h to 24 h, as shown in *Figure 14* and *Figure 15*.

B. Crystal growth of selected $Mn_xFe_{3-x}O_4$ NPs over time

Figure 16 and Figure 17 show the XRD patterns collected for Mn_xFe_{3-x}O₄ NPs and Fe₃O₄ NPs. For Mn_xFe_{3-x}O₄ NPs, a slight shift of the main peak at 311 from the expected position according to the reference pattern MnFe₂O₄ (PDF card no 00-010-0319) at 40.8 to a higher angle is noticed with the increase in the reaction time.

At reaction time $\geq 8h$, a decrease in the D_{TEM} and D_{XRD} of $Mn_xFe_{3-x}O_4$ NPs compared to the undoped Fe₃O₄ NPs was observed, as plotted in *Figure 18*. The crystal size determined from the width of the diffraction peaks using the Scherrer formula showed an increase over time in D_{XRD} from 6 to 16 nm for Fe₃O₄ NPs and from 6 to 10.24 nm for $Mn_xFe_{3-x}O_4$ NPs, as illustrated in *Figure 18 B*.

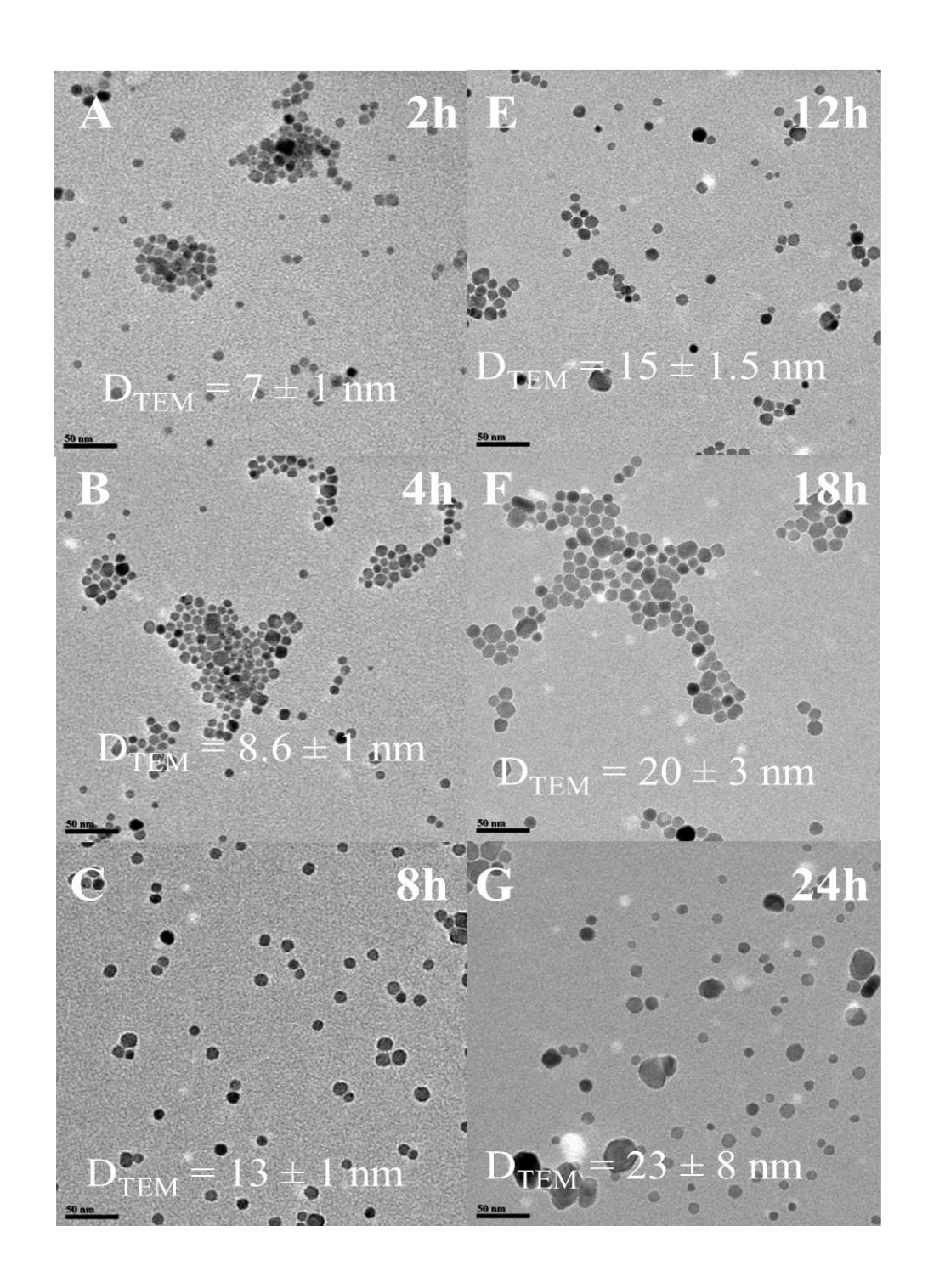


Figure 14: TEM images of the growth of spherical Fe₃O₄ NPs over a time range of 2-24 h at a reaction temperature of 250 °C. DTEM is an average of 500 measured particles.

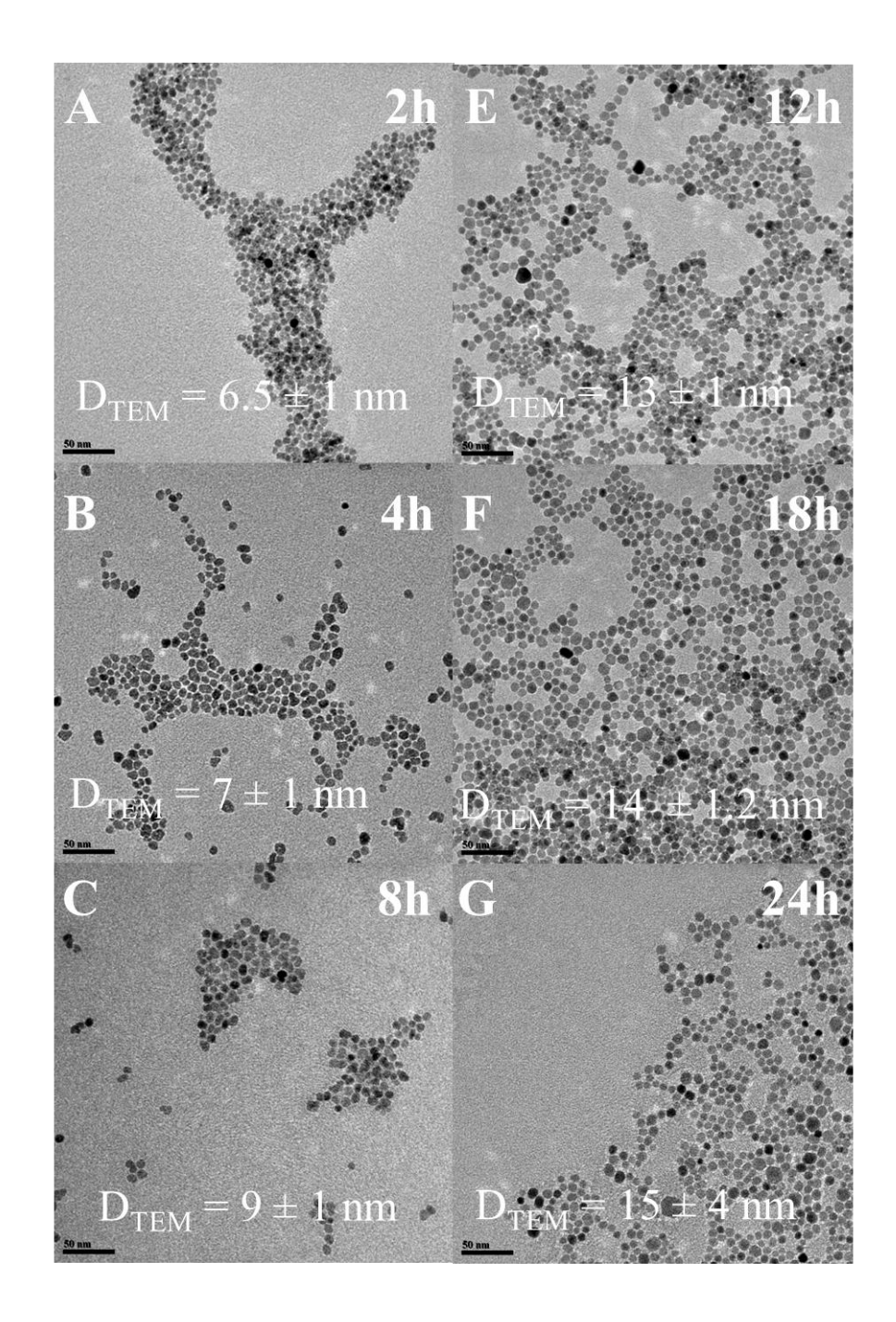


Figure 15: TEM images of $Mn_xFe_{3-x}O_4$ NPs prepared from $[Mn(acac)_2]$ / $[Fe(acac)_3]$ equal to 0.33 over a time range of 2-24h where 500 particles were measured per each tested time point.

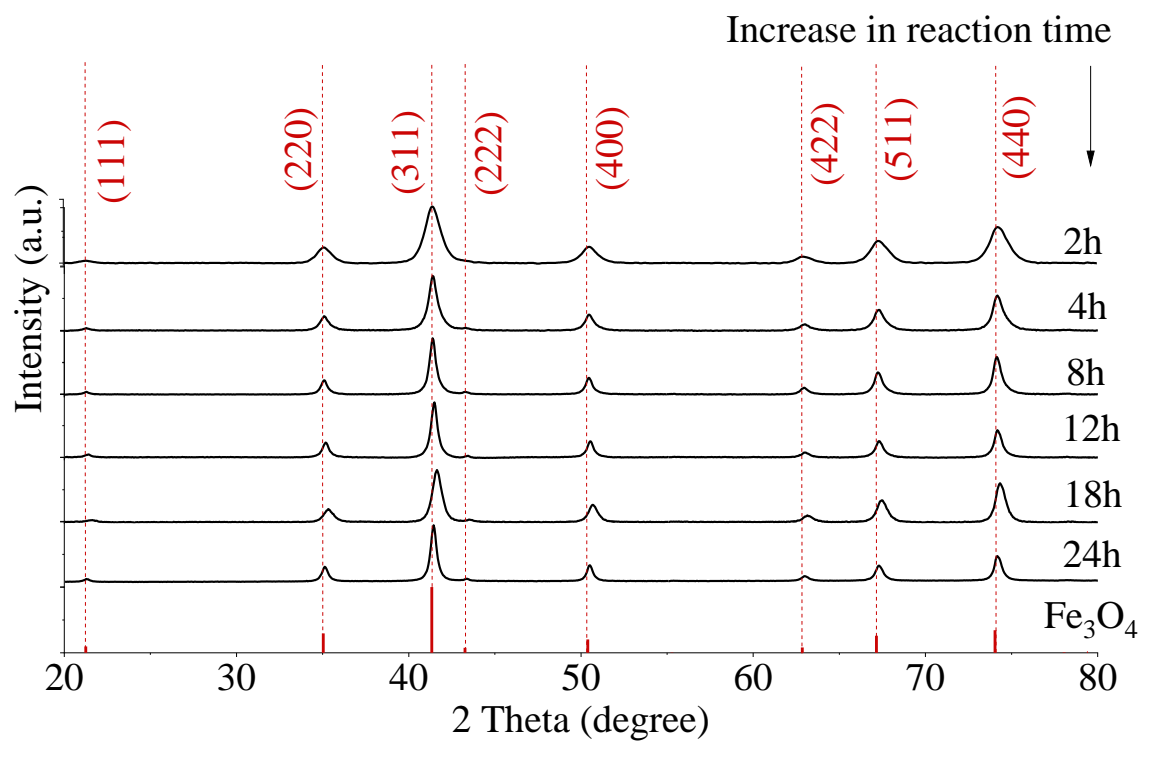


Figure 16: XRD diffractograms of Fe_3O_4 NPs prepared at 250 °C for reaction time (2 h -24 h). XRD patterns were matched to reference Fe_3O_4 (PDF card no 01-089-0688).

Solvothermal treatment of Fe(acac)₃ and [Mn(acac)₂] / [Fe(acac)₃] = 0.33 in the presence of TEG at 250 °C led particle growth of Fe₃O₄ NPs and Mn_xFe_{3-x}O₄ NPs over time. The growth of NPs in our experiment, as shown in *Figure 18A and B* fitted LaMer crystallization model, which predicted a lowering in the concentration of metal ions below critical saturation once the nuclei were formed. Ripening of the particle occurred by diffusion from the precursors on the original nuclei. 175,187,188

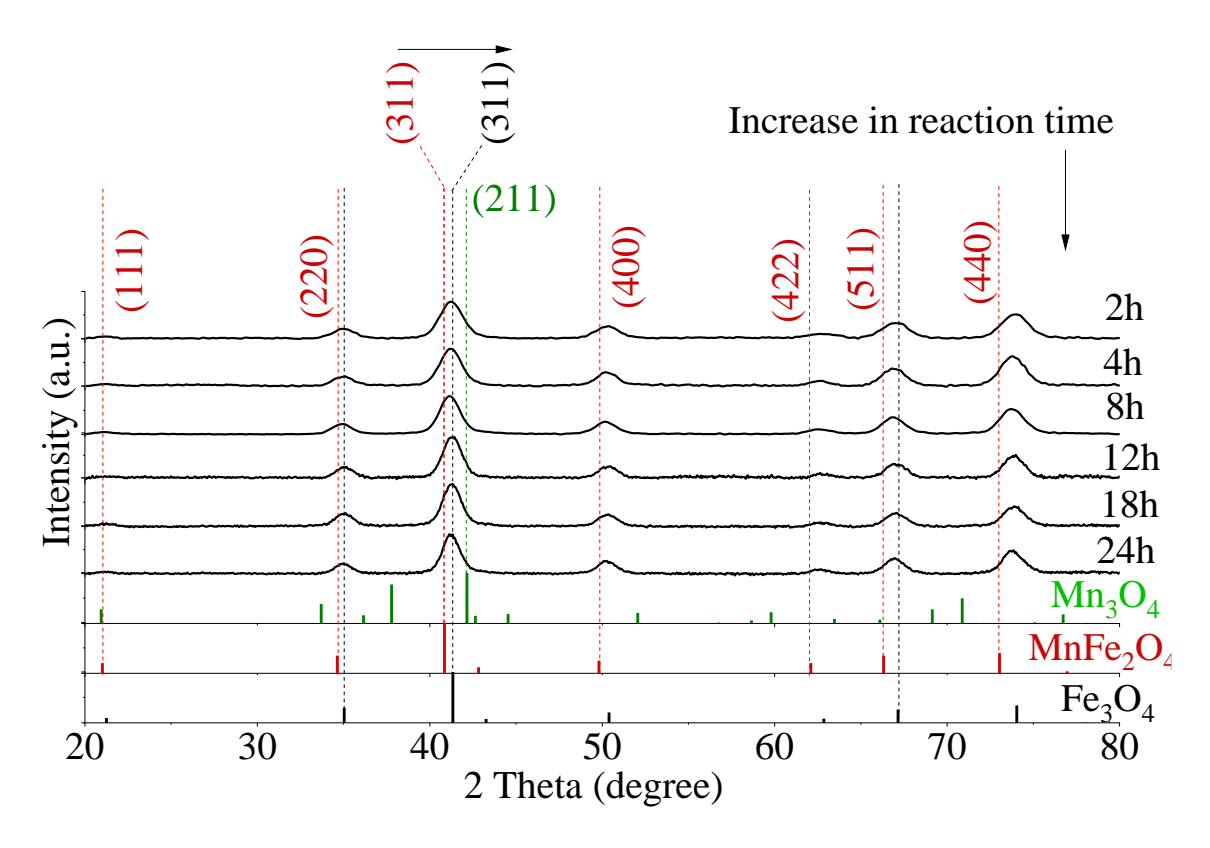


Figure 17: XRD patterns of $Mn_xFe_{3-x}O_4$ NPs prepared by $[Mn(acac)_2]/[Fe(acac)_3] = 0.33$ at 250 °C for synthesis time (2 h-24 h) during. The horizontal arrow pointed out the shifting in the peak of 311 towards the reference Fe_3O_4 (PDF card no 01-089-0688) from the lower diffraction angle of $MnFe_2O_4$ (PDF card no 00-010-0319) in response to the increase in reaction time, which is represented by the vertical arrow.

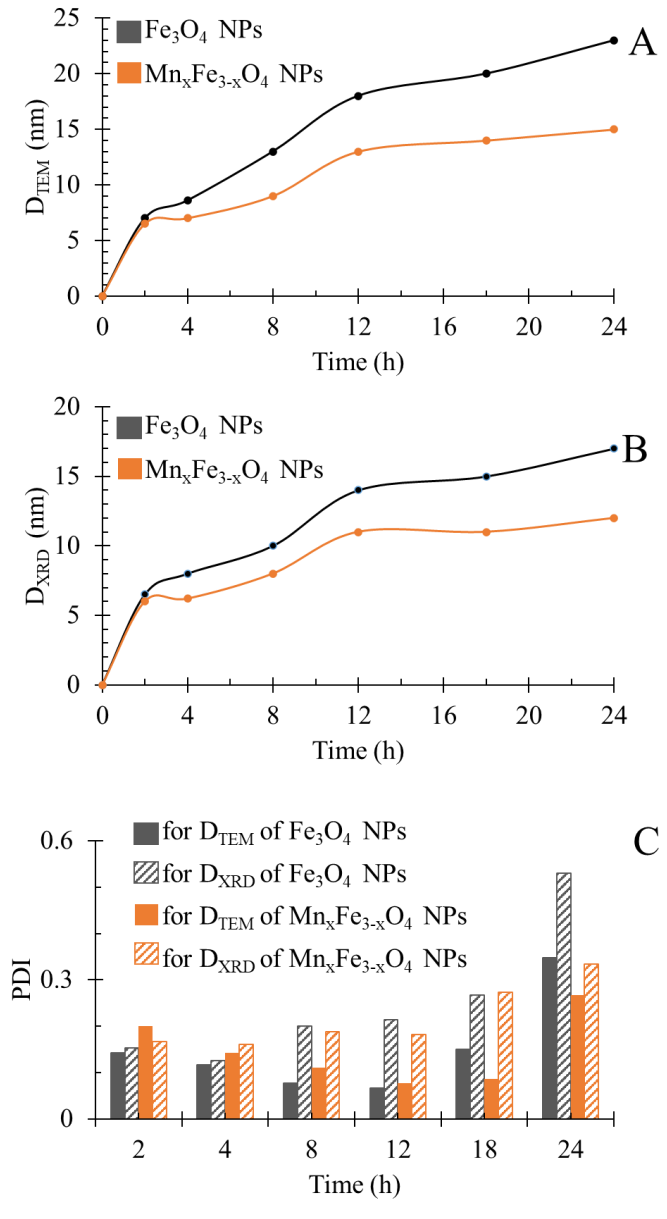


Figure 18: Synthesis time-dependent (A) D_{TEM} (B) D_{XRD} (C) PDI of particle diameter and crystal size of Fe_3O_4 NPs and $Mn_xFe_{3-x}O_4$ NPs prepared from $[Mn(acac)_2]$ / $[Fe(acac)_3]$ equal to 0.33 and both NPs were thermally treated at 250 °C for synthesis time ranged from 2 h to 24 h.

2.3.5 Elemental analysis of Mn_xFe_{3-x}O₄ NS

Results of elemental analyses are presented in Figure 19 A, showing a significant positive relationship between the Mn doping level and [Mn(acac)_{2 or 3}] / [Fe(acac)₃] ratios. The doping level of Mn in Mn_xFe_{3-x}O₄ NPs was probably the reason behind the small shifts in XRD patterns from the reference peak of Fe₃O₄ towards the lower diffraction angle of MnFe₂O₄ when [Mn(acac)_{2 or 3}] / [Fe(acac)₃] increases as shown in *Figure 7* and Figure 8. The variation in the Mn doping levels was significantly affected by the oxidation state of Mn precursor except in the cases when [Mn(acac)_{2 or 3}] / [Fe(acac)₃] ratios equal 0.14 and 0.33. The faster thermal decomposition of Mn(acac)₃ than Mn(acac)₂¹⁸¹ resulted in more Mn-rich NPs prepared by the trivalent Mn precursor than those prepared by the divalent Mn precursor. The increase in the reaction time led to a slight decrease in the Mn doping level, as shown in Figure 19 B. This result explains the minor shift in the peak position of 311 towards higher angles, as shown in Figure 17. The better thermal stability of Mn(acac)₂ than Fe(acac)₃¹⁸¹ resulted in a lower amount of Mndoping in NPs. Overall, at 250 °C, the change in the oxidation state and the ratios between the precursors did not show a variation in the morphology of NPs, but it significantly affected the Mn doping level. While at a synthesis temperature of 200 °C, the oxidation state and the ratios between the precursors affected the Mn doping level and resulted in different shapes of Mn_xFe_{3-x}O₄ NPs and NFs.

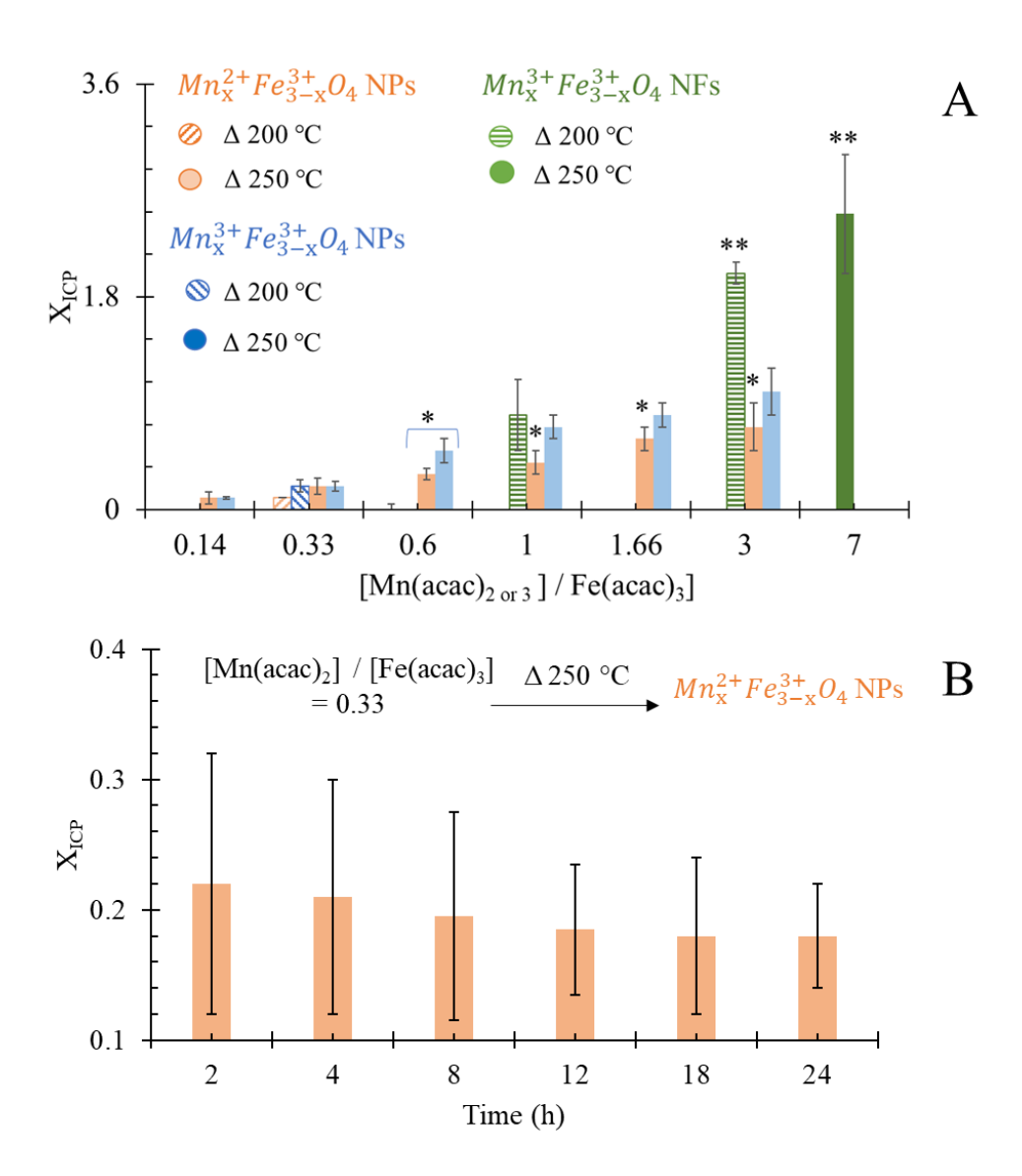


Figure 19: Elemental analysis of $Mn_xFe_{3-x}O_4$ NS (A) prepared at temperatures 200 °C and 250 °C for 6 h. (B) that were prepared using $[Mn(acac)_2]$ / $[Fe(acac)_3] = 0.33$ at synthesis temperature 250 °C for synthesis time 2-24 h. * P < 0.05 and ** P < 0.01 in comparison to $Mn_x^{3+}Fe_{3-x}^{3+}O_4NPs$ of similar precursor ratios.

2.3.6 Functionalization of NPs and NFs

A. Hydrodynamic radius (D_{HD}) of citrate-coated NPs

The D_{HD} of citrate-coated NPs can maintain a physical barrier leading to good dispersibility (*Figure 20* and *Figure 21*). In addition, applying a small molecule like citrate as a ligand resulted in a smaller D_{HD} of NPs than polymeric ligands. In *Figure 21* B, D_{HD} of NPs was increased by increasing the synthesis time, which was attributed to the growth of NPs diameter and crystal sizes of NPs, as shown in *Figure 14*, *Figure 15* and *Figure 18*. The obtained stable dispersions of nano-colloids were attributed to the negative charges induced by the citrate¹⁸⁹ as determined by ζ -potentials (*Figure 21*).

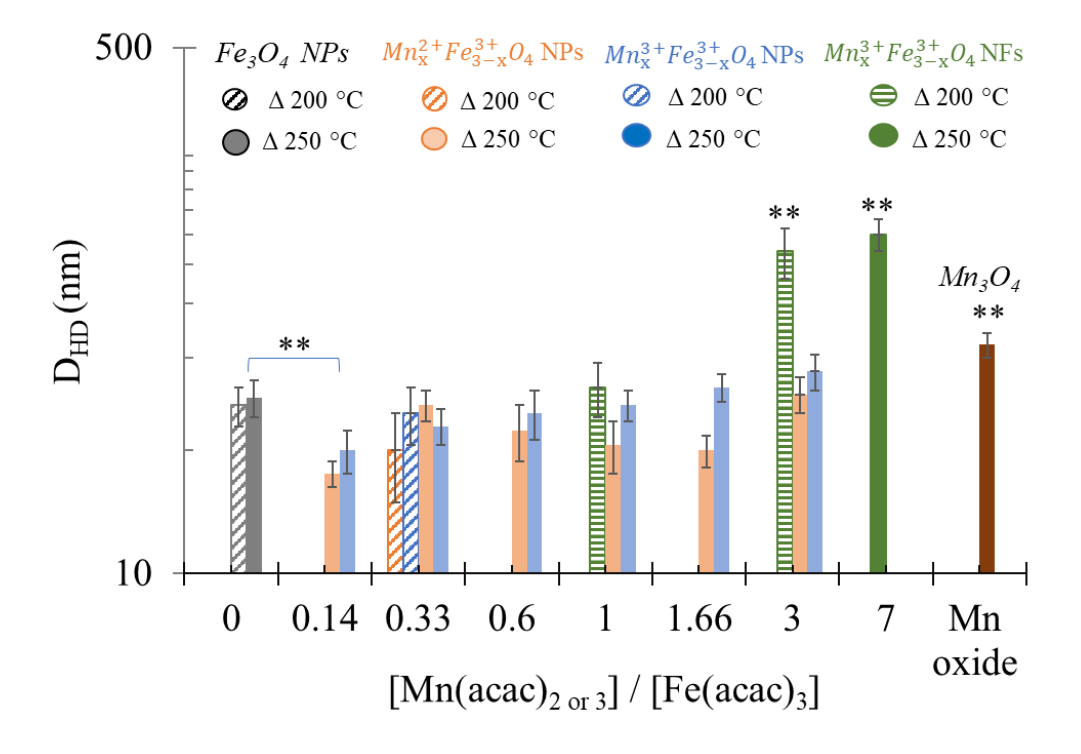


Figure 20: Impact of variation in ratios between [Mn(acac)_{2 or 3}] / [Fe(acac)₃] in Mn_xFe_{3-x}O₄ NS and synthesis temperature (200 vs 250 °C) on D_{HD} of citrate-coated NPs and NFs. **p < 0.01 showed the statistical confidence levels when comparing the size with Fe₃O₄ NPs synthesised at 250 °C.

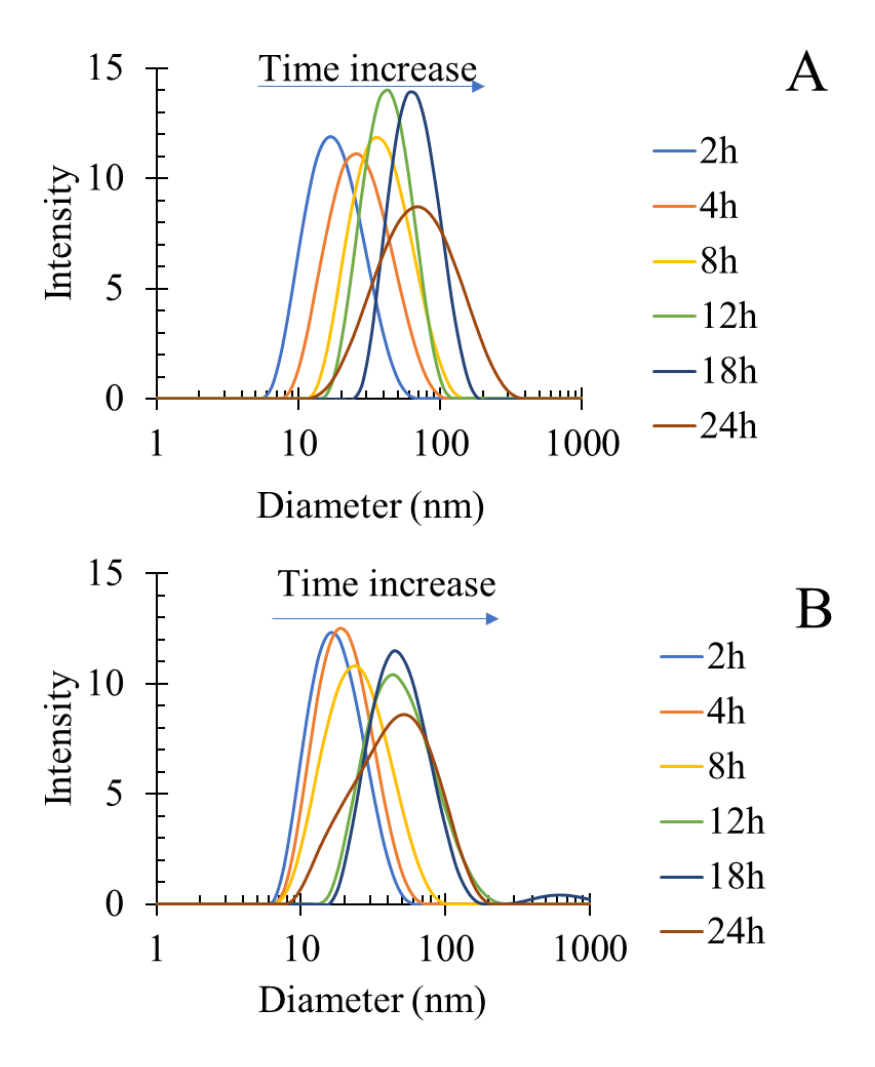


Figure 21: An increase in D_{HD} of citrate coated (A) Fe_3O_4 NPs and (B) $Mn_{0.2}Fe_{2.8}O_4$ NPs prepared at a temperature of 250 °C over synthesis time 2-24 h.

DLS evaluates D_{HD} of the particles in a dispersion depending on the Brownian motion of particles. D_{HD} involved the core diameter of NPs and the surrounding organic ligands on the surface of NS, while D_{TEM} yielded only the core diameter of NS. ¹⁹⁰ The inclusion of organic ligands in D_{HD} explains why the values of D_{TEM} (*Figures 3, 4, 11, 14* and *15*) were smaller than D_{HD} (*Figures 20* and *21*). Over the tested synthesis time (2-24)

h), D_{HD} ranges of Fe₃O₄ and Mn_xFe_{3-x}O₄ were 2.5-3 times and 2-3.5 times, respectively, of their D_{TEM}, because of the tendency of aggregation.¹⁹⁰

B. Zeta potential (ζ -potentials) of citrate-coated NPs

The most negative value of ζ -potential was observed for Mn_xFe_{3-x}O₄ NPs of [Mn(acac)_{2 or 3}] / [Fe(acac)₃] = 3. The reflected colloidal stability was attributed to a weak base (MnCO₃), as expected from XRD patterns (*Figure 7* and *Figure 12*) and the negative charge of citrate. For other Mn_xFe_{3-x}O₄ NPs and NFs, the Mn doping level did not significantly impact their ζ -potentials.

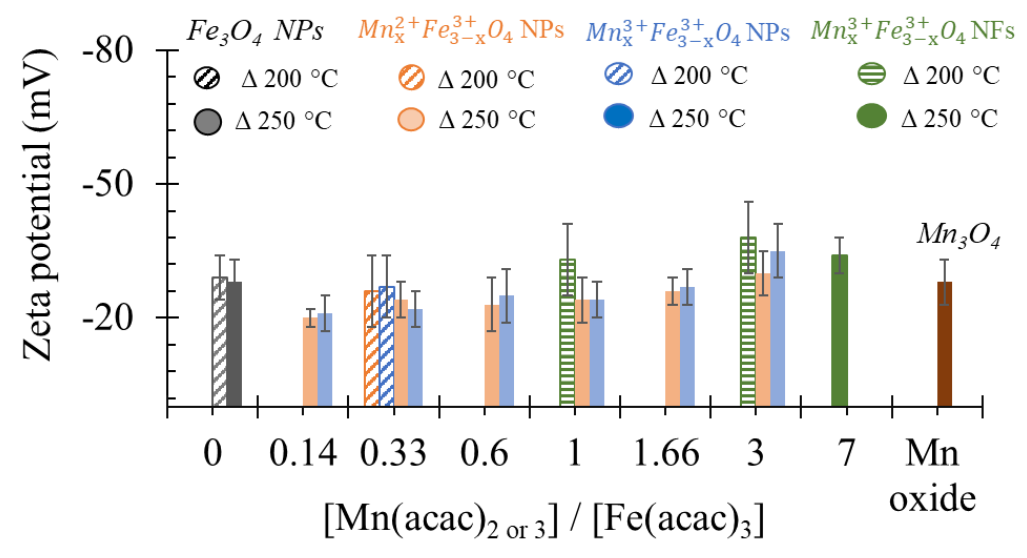


Figure 22: Impact of variation in $[Mn(acac)_{2 \text{ or } 3}]/[Fe(acac)_3]$ and synthesis temperature (200 vs 250 °C) on ζ -potential of NPs and NFs coated by citrate.

C. Functional group characterisation of citrate-coated NPs

Before ligand exchange, the presence of TEG on the surface of the prepared NS was characterised by the FTIR spectrum in *Figure 23*. The peak around 3429 cm⁻¹ and 2874 cm⁻¹ represent the stretching vibrations of the O-H (alcohol) groups and the aliphatic C-H stretching, respectively. The stretching vibration peak at 1063 cm⁻¹ characterises the C-O bond in response to an alcohol group of TEG. Immersing Mn₃O₄ NPs in TEG for 2 h resulted in the adsorption of polyol on its surface, as was shown in *Figure 23 E*.

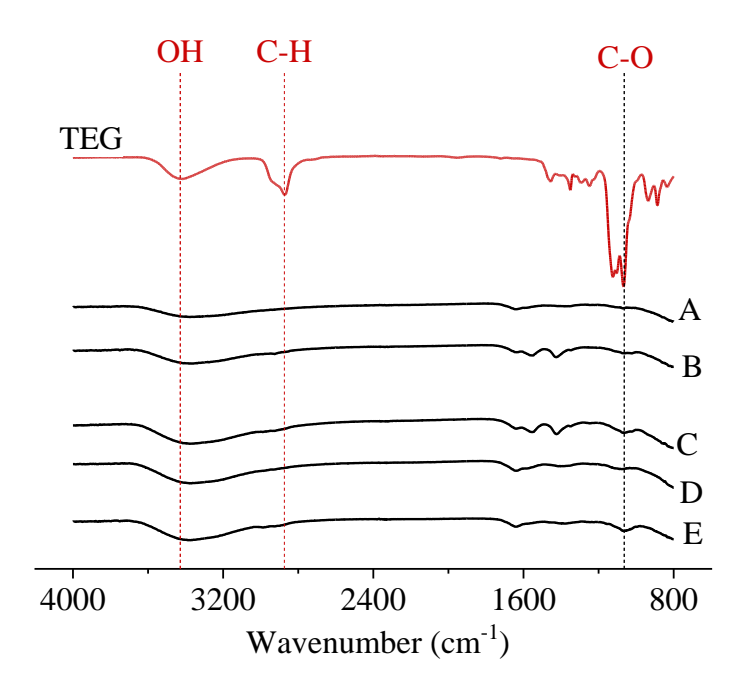


Figure 23: FTIR of TEG and selected TEG coated (A) Fe₃O₄ NPs prepared at 250 °C for 6h of synthesis time (B) $Mn_xFe_{3-x}O_4$ NPs prepared at 250 °C for 6h of synthesis time where $[Mn(acac)_{2 \text{ or } 3}]$ / $[Fe(acac)_3]$ was 0.33 (C) $[Mn(acac)_3]$ / $[Fe(acac)_3]$ was 3, (D) $Mn_{0.8}^{3+}Fe_{2.2}^{3+}O_4$ NFs $[Mn(acac)_3]$ / $[Fe(acac)_3]$ was 3 and (E) Mn_3O_4 NPs.

The FTIR measurements, as shown in *Figure 24*, confirmed that trisodium citrate exchanged TEG ligands which were supported by Chakraborty et al.¹⁹¹ Carboxylates exhibited absorptions for infra-red spectrum for carbonyl group vibration at 1590 cm⁻¹, acyl stretching at 1290 cm⁻¹ and hydroxyl of acid at 3000 cm⁻¹ which overlapped C-H band at 2900 cm⁻¹. A weak band was observed at 1100 cm⁻¹, which was assigned to the C-O mode of the hydroxyl group.^{192–194}

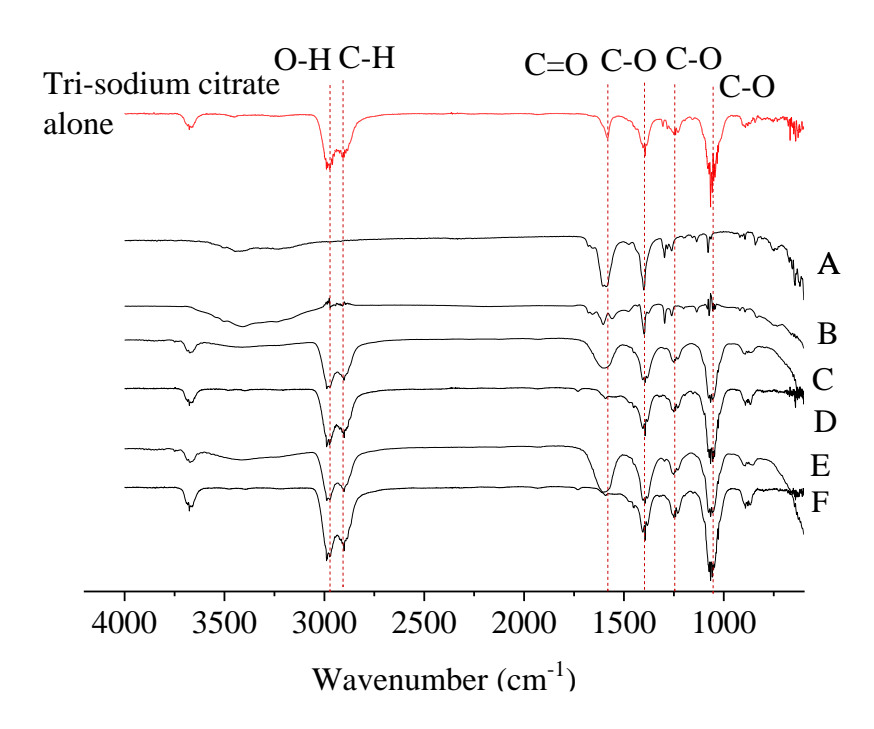


Figure 24: FTIR spectra of tri-sodium citrate alone, (A) Fe_3O_4 NPs prepared at 250 °C for 6h of synthesis time, $Mn_xFe_{3-x}O_4$ NPs prepared at 250 °C where (B) $[Mn(acac)_2]$ / $[Fe(acac)_3]$ and (C) $[Mn(acac)_3]$ / $[Fe(acac)_3]$ were 0.33, for 6h of synthesis time (D) $[Mn(acac)_3]$ / $[Fe(acac)_3]$ was 3, (E) $Mn_{0.8}^{3+}Fe_{2.2}^{3+}O_4$ NFs $[Mn(acac)_3]$ / $[Fe(acac)_3]$ was 3 and (F) Mn_3O_4 NPs. and all samples were coated by citrate.

2.4 Conclusion

A synthetic platform for achieving the most suitable chemical structure of $Mn_xFe_{3-x}O_4$ nanoparticles (NPs) and nanoflowers (NFs) was presented. At 250 °C, both divalent or trivalent manganese precursors formed spherical NPs, whereas, at 200 °C, nanoflower was obtained using a trivalent precursor. The particle growth of selected Fe_3O_4 NPs and $Mn_{0.2}^{2+}Fe_{2.8}^{3+}O_4$ NPs synthesized at 250 °C for a time ranging from 2h to 24h fitted LaMer particle growth model.

Chapter 3. The adsorption capacity of the prepared $Mn_xFe_{3-x}O_4$ NS for Cr^{6+}

3.1 Introduction

The attachment of molecules (adsorbates) to a two-dimensional matrix (adsorbents) is the basis of the adsorption phenomenon. Removing toxic heavy metals such as Cr by adsorption is highly recommended because of the adsorption technology's eco-friendly, cost-effective, and high-efficiency features.¹⁹⁵ The adsorbed oxyanions, such as chromate (Cr₂O₇)²⁻ form outer-sphere and inner-sphere complexes with the surface of iron oxides.¹⁹⁶ The outer-sphere complex is formed by weak reversible bonding, such as electrostatic attraction and hydrogen bonding.¹⁹⁶ Covalent bonds formed due to the inner-sphere complexation.¹⁹⁶ The best adsorbents should eliminate the maximum amount of pollutants to achieve the highest removal efficiency.¹⁸⁵

The adsorption capacity (Qe) in the current project is the amount of adsorbate (Cr^{6+}) removed per gram of the adsorbent. The aim of Chapter 3 was to select the most suitable chemical structure of $Mn_xFe_{3-x}O_4$ NS for the highest Qe for Cr^{6+} . The colourimetric method quantified the Qe and the removal efficiency of Cr^{6+} by NPs. The nature of Cr^{6+} adsorption by the selected $Mn_xFe_{3-x}O_4$ NS has been studied under neutral conditions. The oxidation states of the adsorbed Cr^{6+} by $Mn_{0.2}^{2+}Fe_{2.8}^{3+}O_4$ NPs were analysed using X-ray Photoelectron Spectroscopy (XPS) to explore the chemisorption and the reduction of Cr^{6+} to Cr^{3+} .

3.2Materials and methods

3.2.1 Chemicals

Citrate-capped $Mn_xFe_{3-x}O_4$ NS were used as prepared in Chapter 2 (section 2.2.4). Other used chemicals in this chapter were used as received. Hydroxylamine hydrochloride (ACS reagent, 98.0%), Sulfuric acid (H_2SO_4 , 99.99 %) sodium acetate (anhydrous, ReagentPlus®, \geq 99.0%), iron chloride tetrahydrate (FeCl₂.4H₂O \geq 99%), 1,10-phenanthroline monohydrate (titration \geq 99.5%), and 1,5-diphenylcarbazide (DPC, \geq 98.0%) were obtained from Sigma-Aldrich (UK). Potassium dichromate (K_2CrO_4) was purchased from VWR Chemicals, UK.

3.2.2 Fe quantification in NS

A colourimetric phenanthroline method was applied for the acid-digested tested agent for iron content quantification of the functionalised nanomaterials dispersed in water.¹⁹⁷ OD of the colour was measured using spectrophotometry (SpectraMax M2e, Molecular Devices, UK), and FeCl₂.4H₂O was used as a standard sample. An ICP-AES estimated the concentration of Mn in the Mn₃O₄ dispersion.

3.2.3 Cr⁶⁺ quantification

A stock solution of DPC was prepared by mixing 0.02 g of DPC with 10 mL ethanol and 40 mL of 1.8 M sulfuric acid. 0.1 mL of acid-digested Cr-containing sample samples was added to 2.9 mL of DPC solution. The concentration of Cr⁶⁺ was quantified

by measuring the OD of the colour generated by the Cr^{3+} -DPC complex ^{198,199} method at λ 545 nm using spectrophotometry (SpectraMax M2e, Molecular Devices, UK).

3.2.4 Cr⁶⁺ removal by nano-adsorbents

A. Measurement of the Cr^{6+} adsorption capacity of NS

Equal volumes of aqueous dispersed citrate-coated nano-adsorbents and Cr⁶⁺ aqueous solution were mixed and incubated for 6 h at pH 7 at room temperature. Citrate-capped Mn₃O₄ NPs were used as a controlling group, and 0.01 M of trisodium citrate served as a background. The adsorption capacity (Qe) was quantified following the relationship:¹⁸⁵

$$Qe = \frac{C_i - C_{ad}}{m} \times V$$

The initial concentration of Cr^{6+} (C_i) was 30 mg/L, and C_{ad} was the adsorbed concentration of Cr^{6+} . Therefore, the total volume of the reactants mixture (V) was 2 ml, and the mass of adsorbents (m) was represented with respect to Mn mass fractions.

B. Isotherm of Cr^{6+} adsorption by some selected nanomaterials

The mechanism of Cr^{6+} recovery by some selected NPs that showed the highest Qe was investigated by studying the isotherm of adsorption. The adsorption isotherms of Cr^{6+} removal by the selected NPs that showed the highest Qe (Fe₃O₄ NPs and $Mn_{0.2}^{2+}Fe_{2.8}^{3+}O_4$ NPs, both prepared at a temperature of 250 °C for 6 h) were chosen for studying the adsorption isotherms of Cr^{6+} . The isotherm was measured at room

temperature by varying the initial Cr⁶⁺ concentration from 10 to 250 mg/L at pH 7 for 6 h as a contact time. The adjustment of pH was by HCl [0.1 M] and NaOH [0.1 M]. The concentration of the adsorbents was adjusted to 1 mg/mL. For Mn_{0.2}²⁺Fe_{2.8}³⁺O₄, the mass of the adsorbent was calculated regarding both Fe and Mn fractions (0.68 and 0.05), correspondingly. Langmuir model fitted the adsorption isotherm as following:¹⁹⁵

$$Qe = \frac{Qmax C_e}{K_l + C_e}$$

Qmax (mg/g) was the maximum amount of Cr^{6+} that creates a monolayer on the surface of one gram of adsorbent. K_1 (mg/L) is a constant representing the binding sites' affinity.

C. Chemical adsorption of Cr⁶⁺ on the selected NPs

 $Mn_xFe_{3-x}O_4$ NPs that produced the lowest and the highest adsorption capacity for C^{6+} (Qe) were analysed by XPS, Kratos Analytical AXIS Ultra^{DLD} under ultra-high vacuum conditions (10^{-9} torr). The X-Ray radiation source of XPS was monochromated Al K α (λ = 1.4866 KeV). The data were fitted by combining Gaussian (70%) and Lorentzian (30%) distributions. The oxidation states of Mn, Fe and Cr elements of $Mn_{0.2}^{2+}Fe_{2.8}^{3+}O_4$ NPs ($Mn_xFe_{3-x}O_4$ NPs that were prepared by [$Mn(acac)_2$] / [$Fe(acac)_3$] equal to 0.6 at 250 °C for 6 h) after being exposed to Cr^{6+} were analysed by XPS (Kratos Analytical AXIS Ultra^{DLD} system) under the same conditions as abovementioned. For each element, a normalised peak area is calculated via dividing the area of its representative peak (from XPS spectrum) by the sensitivity factor. The equivalent homogenous atomic fraction (X) is the ratio between its normalised peak area and the

sum of all normalised peak areas, and multiply X by 100% to get an atomic percentage (%).

3.2.5 Statistical analysis of adsorption experiments

The impacts of precursors ratios [Mn(acac)_{2 or 3}] / [Fe(acac)₃], the oxidation state of Mn precursor and synthesis conditions (temperature and time) of the selected $Mn_x^{2+ \text{ or } 3+} Fe_{3-x}^{3+} O_4$ NPs on Cr^{6+} adsorption were studied using a statistical Students t-test. The significance level was described as a calculated probability (P) < 0.05 (*) and P < 0.01 (**). All statistical analyses were done via OriginLab software. All experiments were done in triplicates, except XPS was done one time.

3.3 Results and discussion

3.3.1 Adsorption of Cr⁶⁺ by NS

The removal of Cr^{6+} by $Mn_xFe_{3-x}O_4$ NPs and NFs was studied as a function of the chemical composition and morphology of NS. The quantities of Cr^{6+} (Qe) adsorbed onto citrate-coated Fe_3O_4 NPs were estimated to be 14 ± 1 mg/g at room temperature and pH 7 at equilibrium (*Figure 25 A*). The smaller size of the NPs in our results can probably explain the 1.4-fold higher adsorption efficiency than what was reported by Luther *et al.*¹⁵⁵

In an aqueous solution, Cr^{6+} was mainly present in the oxyanion form of chromate $(Cr_2O_7)^{2-}$ specie. It formed sphere complexes with iron oxide via surface hydroxyl exchange, 53,146,154,201 resulting in the generation of monodentate complexes and desorption of surface hydroxyl groups from the metal oxide surface sites. 53,146,154,201 Upon evaluating commercially available Mn_3O_4 as a control material under the same conditions, the binding capacity of Cr^{6+} (7 \pm 2.6 mg/g) was significantly lower than Fe_3O_4 which was attributed to the low physisorption affinity of Cr^{6+} to such material. 202

The higher adsorption capacity of NFs compared to NPs made of similar [Mn(acac)₃] / [Fe(acac)₃] ratio (1 and 3) but at different synthesis temperatures (200 °C vs 250 °C) was attributed to the higher surface area which allows Cr⁶⁺ to penetrate NFs.²⁰³ Increasing the doping level of Mn in NFs causes a decrease in Cr⁶⁺ adsorption as

 $Mn_{0.8}^{3+}Fe_{2.8}^{3+}O_4$ NFs showed an adsorption capacity of 12 ± 2 mg/g vs 8.5 ± 2 mg/g, as presented in *Figure 25 A*.

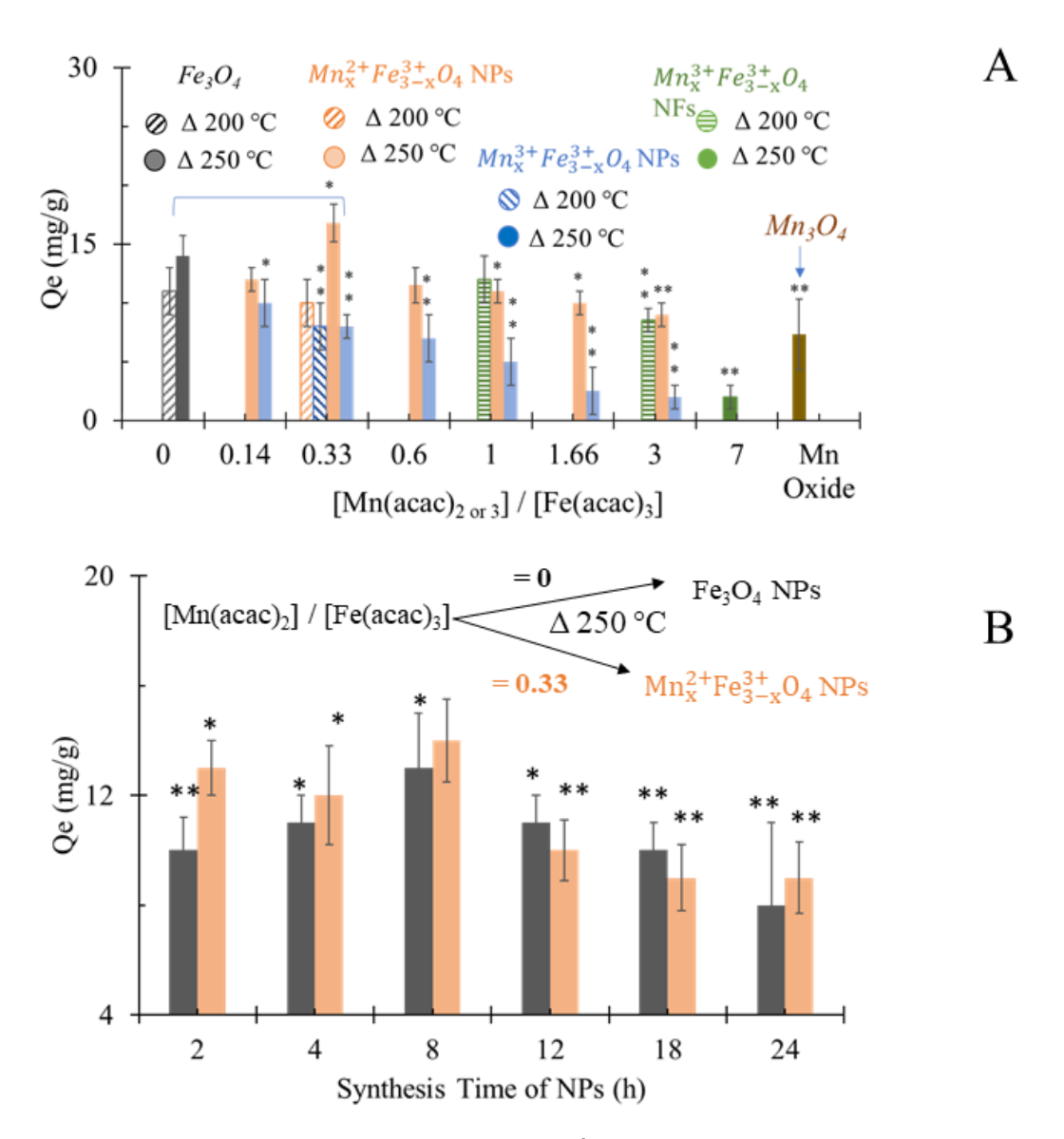


Figure 25: Adsorption capacity (Qe) for Cr^{6+} by (A) $Mn_xFe_{3-x}O_4$ NS (B) Fe_3O_4 and $Mn_x^{2+}Fe_{3-x}^{3+}O_4$ NPs ([$Mn(acac)_2$] / [$Fe(acac)_3$] = 0.33) on their Qe for Cr^{6+} , (both NPs were prepared at 250 °C for ageing time 2-24 h). * P < 0.05 and ** P < 0.01 in relation Fe_3O_4 NP which was prepared at 250 °C for 6 h.

Except $Mn_{0.2}^{2+}Fe_{2.8}^{2+}O_4$ NPs, $Mn_xFe_{3-x}O_4$ NPs prepared from either Mn^{2+} or Mn^{3+} sources showed an inverse trend for removal of Cr^{6+} with the increase of x compared to Fe_3O_4 NPs. Introducing Mn into ferrite reduced the adsorption capacity of Fe_3O_4 to Cr^{6+} from 15.9 mg/g to 8.54-8.9 mg/g.^{155,156} The inverse relationship between Mn concentration in the ferrite composition and adsorption of heavy metals was also observed in the arsenic removal by $Mn_xFe_{3-x}O_4$ NPs.¹⁶⁰ It was attributed to low binding affinity to the arsenic.¹⁶⁰ The increased Co substitution for iron in magnetite ($Fe_{3-x}Co_xO_4$, $0 \le x \le 1$) slightly enhanced the adsorption capacity of NPs to Cr^{6+} .²⁰⁴ The decrease in Mn doping in the $Mn_{1-x}Co_xFe_2O_4$ (x = 0.2, 0.4 and 0.6) induced a progressive, positive impact on the adsorption efficiency of Cr^{6+} . Since Mn^{2+} ions have larger ionic radii than Co^{2+} (0.8 A° vs 0.7 A°), the increase in x made overcoming energy barriers for ion exchange interaction more difficult.¹⁵⁸ The release of Mn into the solution due to Cr^{6+} reduction was suggested to alter the surface structure.¹⁵⁵

Considering the larger ionic radii of Mn^{2+} cation than Fe^{3+} (0.80 Å vs 0.64), 159 our results can be explained based on the reverse impact of Mn doping level on the adsorption capacity of $Mn_xFe_{3-x}O_4$ NPs to Cr^{6+} . Yet in $Mn_x^{3+}Fe_{3-x}^{3+}O_4$ NPs, the ionic radius of Mn^{3+} is smaller than Mn^{2+} and is approximately equal to Fe^{3+} radius but $Mn_x^{3+}Fe_{3-x}^{3+}O_4$ NPs showed lower adsorption capacities than their $Mn_{0.2}^{2+}Fe_{2.8}^{3+}O_4$ NPs counterparts. The inferiority of Mn^{3+} in the adsorption of Cr^{6+} could be attributed to the tendency of Mn^{3+} ([Ar] $3d^4$ $4S^0$) to be reduced to Mn^{2+} . The half-filled 3d orbital in the electronic configuration of Mn^{2+} ([Ar] $3d^5$ $4S^0$) makes it more stable than Mn^{3+} . While, oxidizing Fe^{2+} ([Ar] $3d^6$ $4S^0$) into more stable Fe^{3+} ([Ar] $3d^5$ $4S^0$) is favoured and can support the possible redox-based adsorption of Cr^{6+} by Fe_3O_4 .

The adsorption capacity of Cr^{6+} by stoichiometric $MnFe_2O_4$ NPs was higher than by non-stoichiometric $Mn_{1-x}Co_xFe_2O_4$ (x=0.2, 0.4 and 0.6). But, our results agree with what was stated by Martinez-Vargas et al. 160 as non-stoichiometric $Mn_{0.25}Fe_{2.75}O_4$ NPs exhibited the best adsorption capacity to arsenic. 160 Under the employed conditions, only $Mn_{0.2}^{+2}Fe_{2.8}^{+3}O_4$ (x=0.2), prepared at 250 °C was comparable to the adsorption capacity of Fe_3O_4 NPs (16.8 \pm 1.6 vs 14 \pm 1.7 mg/g, respectively). Using $Mn_{0.2}^{+2}Fe_{2.8}^{-3+}O_4$ NPs improved the Cr^{6+} recovery by 20% compared to Fe_3O_4 NPs and by 140% with regard to Fe_3O_4 NPs as shown in $Figure\ 25\ A$. The adsorption of chromate anions was because of forming weak bonds with Fe_3O_4 Substrate. The surface of Fe_3O_4 NPs has been reported to be rich in hydroxyl groups, 160 which favour Fe_3O_4 NPs and small diameter can explain their superior adsorption capacity compared to other reported Fe_3O_4 NPs (13.54 and 15 mg/g). At the same time, it is comparable with results from other reports (18.02 mg/g). 154

3.3.2 Impact of time-dependent growth of the selected NPs on their Qe for Cr⁶⁺

The removal of Cr^{6+} by Fe_3O_4 NPs and $Mn_{0.2}^{2+}Fe_{2.8}^{3+}O_4$ NPs was studied as a function of the time-dependent growth of NPs. The highest Qe for Cr^{6+} adsorbed on either citrate-coated Fe_3O_4 NPs or $Mn_{0.2}^{2+}Fe_{2.8}^{3+}O_4$ NPs were shown for NPs prepared at 250 °C for an ageing time of 6 h. It was observed that $Mn_{0.2}^{2+}Fe_{2.8}^{3+}O_4$ NPs prepared at 6 h of reaction time had the lowest PDI, as shown in *Figure 10* vs *Figure 18* C and the best Qe over all tested NPs in the present study.

An inverse relationship between the growth of the tested NPs (reaction time > 6h) and Qe was observed in $Figure\ 25\ B$. The increased reaction time during NPs preparation caused further growth of $Mn_{0.2}^{2+}Fe_{2.8}^{3+}O_4$ NPs and Fe_3O_4 NPs were combined with an improvement in the crystallinity of NPs. The increase in the diameter and crystallinity of NPs resulted in a decrease in the surface area of NPs, which can explain the negative impact of NPs' growth on their Qe.

3.3.3 Isotherm of Cr⁶⁺ adsorption by the selected NPs

The adsorption of Cr⁶⁺ by the selected citrate-coated adsorbents that showed the best Qe at pH 7 at room temperature can be described by Langmuir isotherm model as a function of the initial Cr⁶⁺ concentrations (*Figure 26 A-C*). Hence, the adsorbent NPs' surface has homogeneous energy distribution via the monolayer sorption process. Langmuir isotherm model considered the adsorption rate and desorption to be equal. The calculated maximum adsorption capacity (Qmax) by Langmuir isotherm model fitted the results of Qe, as shown in Table 2. The low values of K_L were indicators of the low binding affinity of adsorbate in the first monolayer to the tested NPs.

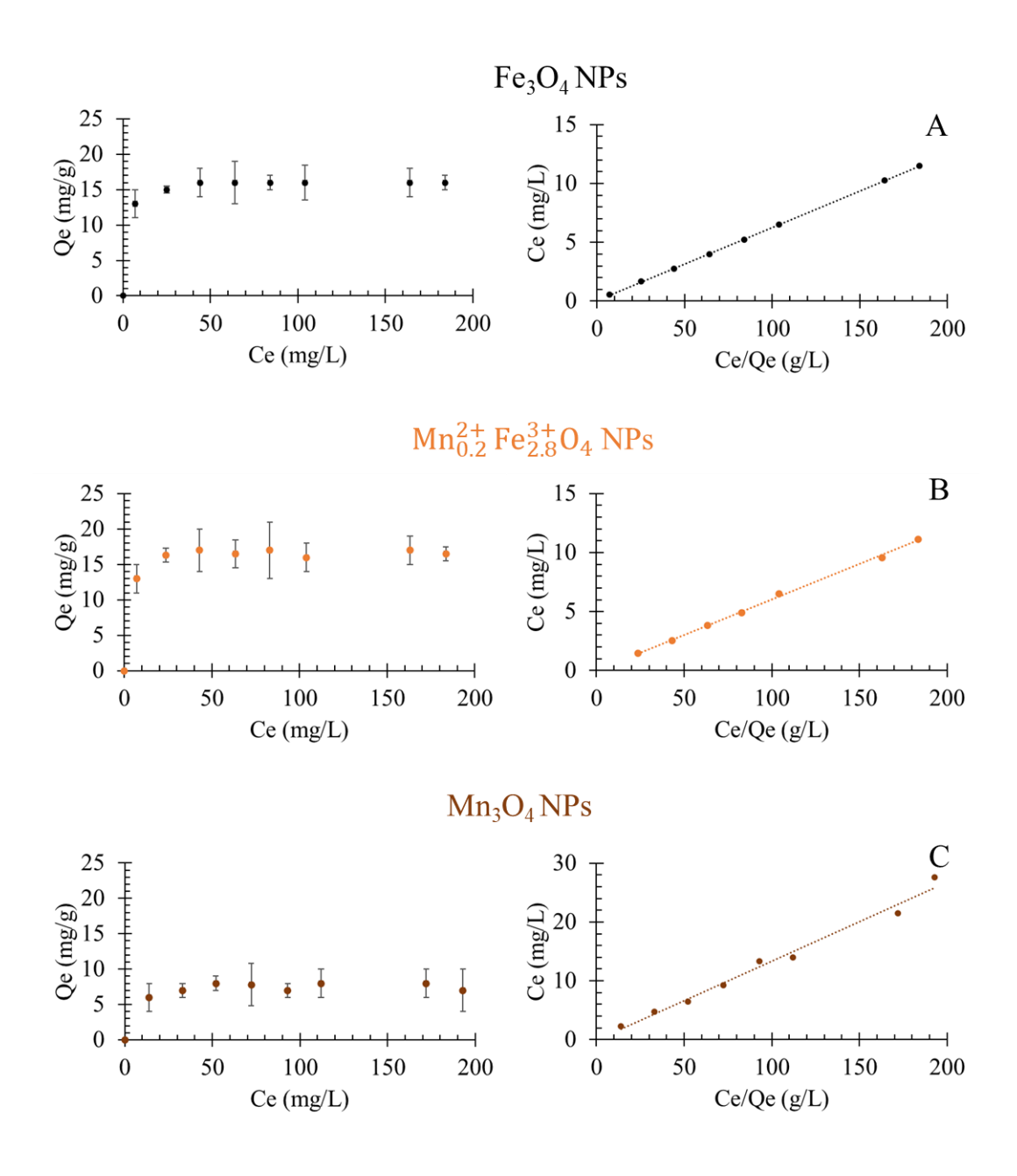


Figure 26: Adsorption isotherm for Cr^{6+} and linearisation of Cr^{6+} adsorption fitted by Langmuir model for (A) Fe_3O_4 , (B) $Mn_{0.2}^{2+}Fe_{2.8}^{3+}O_4$ and (C) Mn_3O_4 NPs.

Table 2: Calculated linear parameters for Cr^{+6} adsorption on NPs fitted by Langmuir model for isotherm.

	Qmax (mg/g) ^a	$K_{ m L}$	\mathbb{R}^2
Fe ₃ O ₄	14.7 ± 1.5	1.1	0.99
$Mn_{0.2}^{+2}Fe_{2.8}^{+3}O_4$	18.7 ± 1*	0.9	0.99
Mn ₃ O ₄	7.7 ± 2**	0.9	0.95

a Qmax was presented as (mean \pm standard deviation) of 3 independent synthesis experiments, and *p < 0.05 and **p < 0.01 showed the statistical confidence levels by comparing Qmax in relation to Fe₃O₄NPs.

3.3.4 The oxidation state of Mn and Fe in the selected Mn_xFe_{3-x}O₄ NPs.

XPS was used to gain insights into the chemical composition and oxidation state of the selected $Mn_xFe_{3-x}O_4$ NPs that showed either maximum or minimum Cr^{6+} recovery efficiency, as in Figure 25 and Figure 26. Binding energies (BEs) were used to identify elements and valence states. In *Figure 27*, the wide-scan spectra of $Mn_{0.2}^{2+}Fe_{2.8}^{3+}O_4$ and $Mn_x^{3+}Fe_{3-x}^{3+}O_4$ NPs indicate the presence of carbon (C) and oxygen (O) elements besides

Mn and Fe. the position of BE for Mn 2p and Fe 2p were marked at 641.80 eV and 710 eV, respectively. Using the relative area under the deconvoluted XPS spectra, a semi-quantitative estimation of the valence states of the elements in the mixed-valence compounds was achieved.

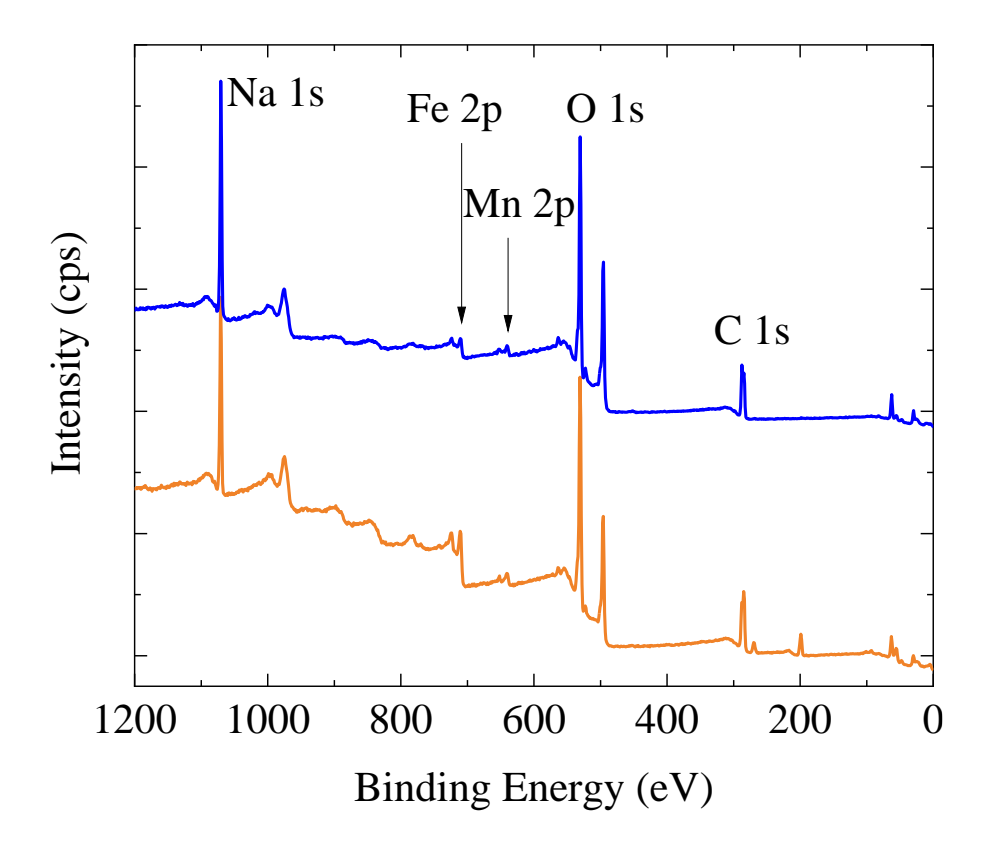


Figure 27: XPS spectra of $Mn_xFe_{3-x}O_4$ NPs where orange and blue represent $Mn_{0.2}^{2+}Fe_{2.8}^{3+}O_4$ and $Mn_x^{3+}Fe_{3-x}^{3+}O_4$ respectively.

A. The oxidation state of Mn in $Mn_{0.2}^{2+}Fe_{2.8}^{3+}O_4$ NPs and $Mn_x^{3+}Fe_{3-x}^{3+}O_4$ NPs

In *Figure 28 A*, Mn 2p was fitted by 5 contributions at around 640.2, 642.1, 645.2, 651.6 and 653.4 eV. The broadening of peaks demonstrated that Mn is present in an oxide form rather than a metallic one.^{206,207} The asymmetric Mn 2p3/2 main metal peak at 640.2

eV was subjected to a 2p3/2 to 2p1/2 splitting of FWHM 2.7 and 2.1 eV, respectively. BEs of 640.2 and 651.1 eV were reported to be related to Mn 2p3/2 and Mn 2p1/2 of Mn²⁺ correspondingly. The small satellite peak at 645.2 eV (\approx 14%, 2.9 eV FWHM) was assigned to MnO. Since stoichiometric Mn_xFe_{3-x}O₄ can be expressed as MnO-Fe₂O₃, this points to the formation of Mn_xFe_{3-x}O₄ NPs²⁰⁶ in agreement with XRD results (*Figure 7 C*). In the case of Mn³⁺_xFe³⁺_{3-x}O₄ NPs, the BE of Mn 2p was fitted by 4 peaks at 640.2, 642.1, 651.6 and 653.4 eV, as shown in *Figure 28 B*. The absence of a small satellite peak at 645.2 was reported due to Mn³⁺ presence represented by BEs of 640.2 and 651.6 eV. ²⁰⁶

Partial oxidation of Mn^{2+} to Mn^{3+} has been reported for $Mn_xFe_{3-x}O_4$ NPs prepared via polyol solvothermal method using $Mn(acac)_2$ precursor¹⁶³ due to the oxidative atmosphere inside the autoclave. ¹⁵⁹ Mn^{2+} and Mn^{3+} cations were reported to be present in $Mn_xFe_{3-x}O_4$ NPs. ¹⁶³ Hence, trivalent Mn was supposed to be formed during the synthesis of NPs as suggested by XRD and matched $MnCO_3$ ICDD PDF card no. 00-010-0319 (*Figure 12*). The relatively lower amount of Mn^{2+} in Mn^{3+} -substituted ferrites could account for the fact that $Mn_x^{3+}Fe_{3-x}^{3+}O_4$ NPs showed lower Cr^{6+} adsorption capacity than Mn^{2+} -substituted ferrites, as plotted in *Figure 25 A*. The presence of Mn^{4+} can be attributed to the possible oxidation of $Mn^{2+}/^{3+}$ during the preparation conditions.

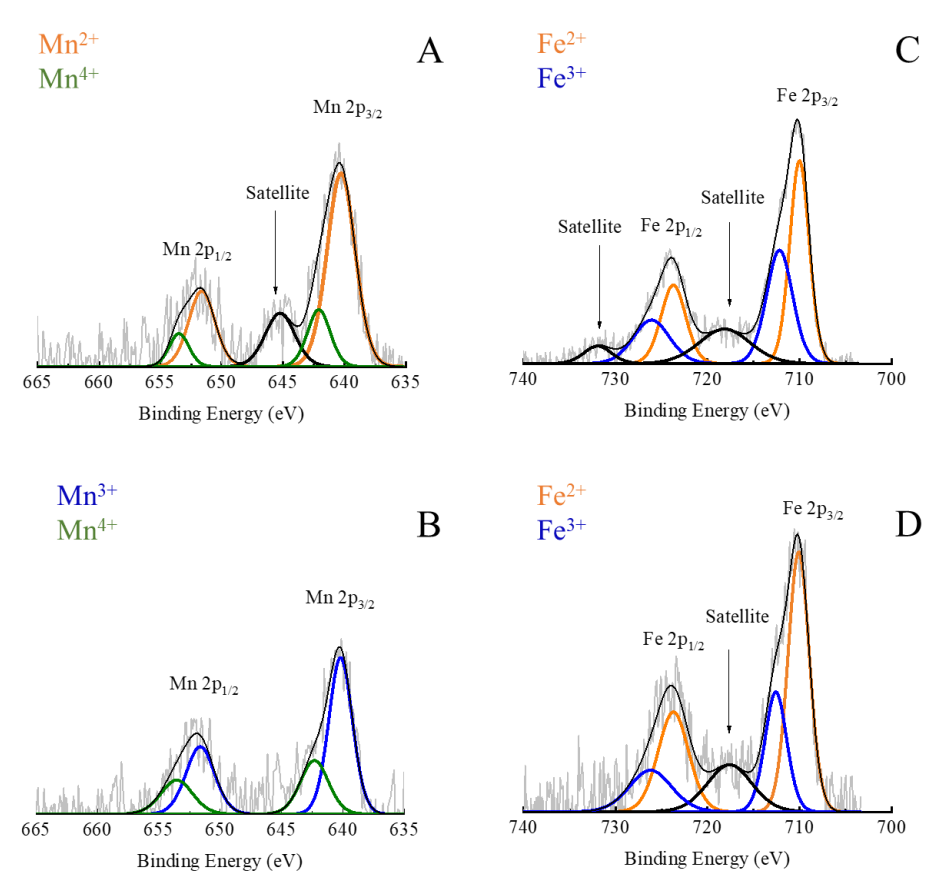


Figure 28: High-resolution XPS spectra of (A, B) Mn 2p, (C, D) Fe 2p; for $Mn_{0.2}^{2+}Fe_{2.8}^{3+}O_4$ (A, C) and $Mn_x^{3+}Fe_{3-x}^{3+}O_4$ NPs (B, D).

B. The oxidation state of Fe in $Mn_{0.2}^{2+}Fe_{2.8}^{3+}O_4$ and $Mn_x^{3+}Fe_{3-x}^{3+}O_4NPs$

For both samples, as shown in *Figure 28 C* and *D*, the peak of Fe 2p was split into Fe 2p3/2 at 710 eV, and its satellite appeared at 718 eV. While Fe 2p1/2 was situated at BE at 724 eV, and another satellite peak was observed at 729.5 eV. The peak of Fe 2p1/2 was wider and weaker than Fe 2p3/2 peak. FWHM of Fe 2p1/2 peak was smaller than Fe 2p3/2 because of spin-orbit (j–j) coupling. FWHM of Fe 2p peaks at 712 eV was slightly smaller than its counterpart at 712 eV, which can serve as an indicator for the presence of both Fe²⁺ and Fe³⁺ in these two samples. 207,209 This interpretation matched the elemental analysis results by ICP-AES (*Figure 19 A*) for the formation of non-stoichiometric Mn_xFe_{3-x}O₄. The absence of the satellite peak at 732 eV, as shown in *Figure 28 D*, was attributed to the presence of Fe₃O₄. 209

3.3.5 Reduction of Cr⁶⁺ by the selected Mn_xFe_{3-x}O₄ NPs

The possible redox mechanism of Cr^{6+} adsorption on $Mn_{0.2}^{2+}Fe_{2.8}^{3+}O_4$ NPs were investigated by studying the oxidation state of Mn and Fe of the adsorbent and Cr as an adsorbate by XPS, as shown in *Figure 29*.

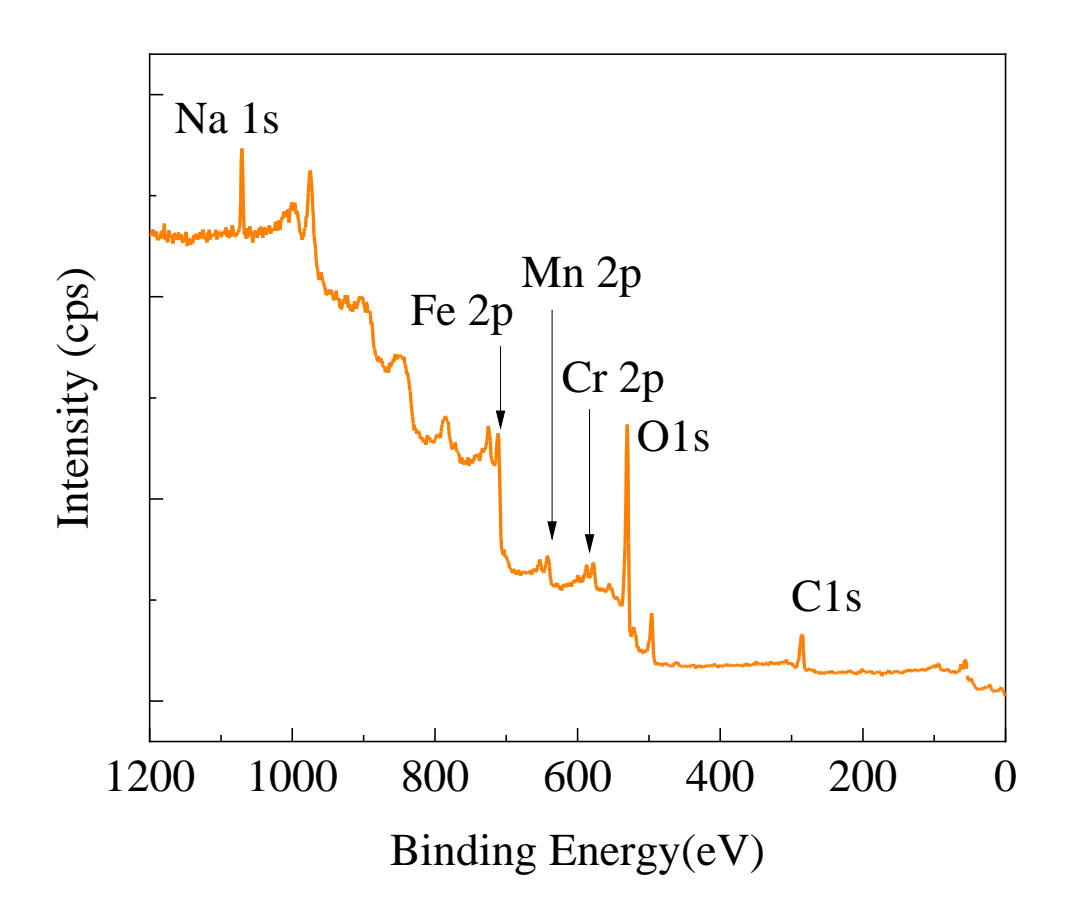


Figure 29: XPS spectrum of $Mn_{0.2}^{2+}Fe_{2.8}^{3+}O_4$ NPs treated by Cr^{6+} .

A. Mn in $Mn_{0.2}^{2+}Fe_{2.8}^{3+}O_4$ NPs after Cr^{6+} adsorption

After Cr^{6+} adsorption on $Mn_{0.2}^{2+}Fe_{2.8}^{3+}O_4$ NPs, the position of BE for Mn 2p was slightly shifted from 640.45 eV (*Figure 28 A*) to higher BE (641.80 eV), as shown in *Figure 30 A*, which could be attributed to the possible oxidation of Mn^{2+} . The peak became wider (FWHM = 3.029 vs 3.35), and the broadening of Mn 2p peak demonstrated that Mn is present in oxide form rather than a metallic one.^{206,207}

Like untreated Mn_{0.2}Fe_{2.8}O₄ NPs, Mn 2p was fitted by 5 contributions located at around 640.3, 642.2, 644.61, 652.2 and 654.8 eV. These peaks of Mn 2p can be grouped into two asymmetric peaks of Mn 2p_{3/2} and Mn 2p_{1/2}, and the corresponding BE values are 642 and 652 eV, respectively. The distance between the two photoelectron peaks is shorter than the untreated NPs (10.1 eV vs 11.4 eV), which is in the reported range by Biesinger et al.²⁰⁶ Mn in Mn_{0.2}²Fe_{2.8}³O₄ NPs were considered doubly valent as the peak of Mn 2p_{3/2} was deconvoluted into 640.35 and 642.25 eV representing Mn²⁺ and Mn⁴⁺, respectively. The peak of Mn 2p1/2 was also fitted into two contributions of Mn²⁺ and Mn⁴⁺ for 652.15 and 654.6 eV, respectively. ^{154,206–208} The fifth small satellite peak at 645.2 eV was assigned to Mn²⁺ of MnO.²⁰⁶ Since stoichiometric MnFe₃O₄ can be expressed as MnO-Fe₂O₃, this pointed to the formation of Mn_xFe_{3-x}O₄ NPs.²⁰⁶

B. Fe after Cr^{6+} interaction with $Mn_{0.2}^{2+}Fe_{2.8}^{3+}O_4$ NPs

After Cr^{6+} adsorption on $Mn_{0.2}^{2+}Fe_{2.8}^{3+}O_4$ NPs, the position of BE for Fe 2p shifted slightly to higher BE (from 710 eV to 711 eV), and the peak became somewhat narrower (FWHM = 3.88 vs 3.45). A peak of Fe 2p3/2 was spotted at 710.75 eV, while the asymmetric peaks are situated at 723.9 eV, attributed to 2p1/2. 207,209 Unlike untreated $Mn_{0.2}^{2+}Fe_{2.8}^{3+}O_4$ NPs, Fe 2p missed the satellite peak at 718 eV as shown in *Figure 30 B*, which was due to the presence of Fe₃O₄. 209 The ratio between Mn and Fe was doubled from 0.24 (as was reported by XPS and the range based on elemental analysis by ICP-AES in our of untreated $Mn_{0.2}^{2+}Fe_{2.8}^{3+}O_4$ NPs (see *Figure 19 A*) to 0.44 which can be attributed to the release of Fe in the medium.

C. Reduction of Cr^{6+} by $Mn_{0.2}^{2+}Fe_{2.8}^{3+}O_4$ NPs

Besides the ion exchange, our findings in the present chapter reveal that the interaction between Cr^{6+} and $Mn_{0.2}^{2+}Fe_{2.8}^{3+}O_4$ NPs involved a redox reaction. The ratio $[Cr^{3+}]$ / $[Cr^{6+}]$ was estimated to be 2.56, as shown in *Figure 30 C*. The chemical redox reaction between $Mn_{0.2}Fe_{2.8}O_4$ NPs adsorbent surface and Cr^{6+} solution can explain the possible oxidation of Mn^{2+} and iron release. The ability of $Mn_{0.2}^{2+}Fe_{2.8}^{3+}O_4$ NPs to reduce Cr^{6+} , in contrast to a report by Hu et al., ¹⁵⁴ can be attributed to the abundance of Mn^{2+} over Mn^{4+} in the present structure. The existence of Mn^{4+} in their tested $MnFe_2O_4$ adsorbent was reported. ¹⁵⁴

Overall, there were two possible schemes for the adsorption and reduction of Cr^{6+} by $Mn_{0.2}^{2+}Fe_{2.8}^{3+}O_4$ NPs. One of them was the adsorption of Cr^{6+} on the surface of NPs and then the reduction of Cr^{6+} into Cr^{3+} . Another scheme was the reduction of Cr^{6+} into Cr^{3+} by NPs, followed by the adsorption of Cr^{3+} . Doping Fe_3O_4 NPs by Mn^{2+} was reported to increase the superficial hydroxyl level, improving the adsorption of Cr^{6+} of NPs, as shown in *Figure 25 A* and *B* via ion exchange. At room temperature and pH 7, Langmuir isotherm model described the nature of Cr^{6+} adsorption by $Mn_{0.2}^{2+}Fe_{2.8}^{3+}O_4$ NPs (*Figure 26 B*). Hence, the nano-sorbents' surface has a homogeneous energy distribution via the monolayer sorption process.

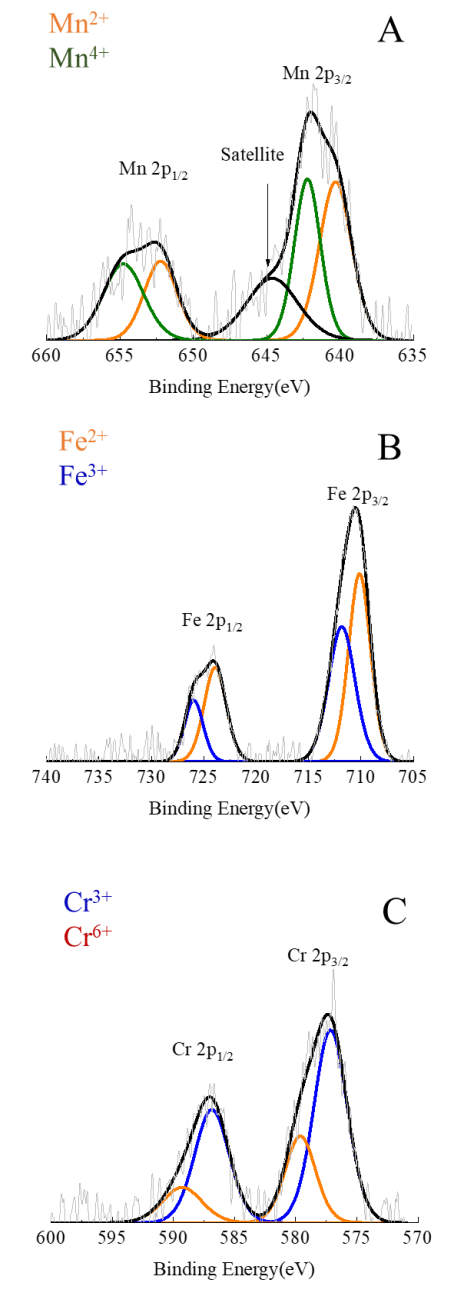


Figure 30: For $Mn_{0.2}^{2+}Fe_{2.8}^{3+}O_4$ NPs treated by Cr^{6+} , high-resolution XPS spectra of (A) $Mn\ 2p\ and\ (B)\ Fe\ 2p\ (C)\ Cr\ 2p.$

3.3.6 The proposed mechanism of Cr⁶⁺ adsorption by Mn_xFe_{3-x}O₄ NPs

The interaction between Cr^{6+} and $Mn_{0.2}^{2+}Fe_{2.8}^{3+}O_4NPs$ were proposed to involve both adsorption and reduction. Mn_{0.2}²⁺Fe_{2.8}³⁺O₄NPs adsorbed Cr⁶⁺ via a ligand exchange between the hydroxyl groups on the surface of NPs and chromate (Cr₂O₇)²⁻ oxyanion.53,146,154,201 The adsorption of Cr6+ on iron oxides/hydroxides was reported to generate inner-sphere coordination complexes, ¹⁹⁶ as shown in *Figure 31*. Covalent bonds link ligands to a central metal atom (or ion) in such coordination complexes. Fe forms monodentate (one covalent bond) and bidentate (two covalent bonds) complex with chromates. 196 The inner-sphere complex is strong and non-reversible. 196 The reduction of adsorbed Cr⁶⁺ to Cr³⁺ by Fe²⁺ or Mn²⁺ and Cr³⁺ was precipitated Cr(OH)₃ or Cr_xFe₁₋ $_{x}(OH)_{3}$. From the above analysis; there were two kinds of divalent ions in $Mn_{0.2}^{2+}Fe_{2.8}^{3+}O_{4}$ NPs, which are Mn^{2+} and Fe^{2+} (Figure 28 A and B), were stated by higher reductive activity. 210 Mn²⁺ can offer 2 electrons to be Mn⁴⁺, as shown in Figure 28 A, which can reduce Cr⁶⁺ into Cr³⁺, as supported by XPS findings in Figure 30 C. In addition to the 2 electrons offered by Mn²⁺, Fe²⁺ can be oxidised into Fe³⁺ and lose one electron to reduce Cr⁶⁺ into Cr³⁺. ^{210,212} After Cr⁶⁺ interaction, the release of Fe from Mn²⁺_{0.2}Fe³⁺_{2.8}O₄ NPs to the medium were an indicator of Cr3+ metal substitution, and the oxidation of Fe was approved in XPS results (Figure 30 B). The reduction of Cr⁶⁺ into Cr³⁺ was revealed by XPS; as shown in Figure 30 C. Unreduced, adsorbed Cr⁶⁺ can be incorporated into the Cr_xFe_{1-x}(OH)₃ structure.²¹¹

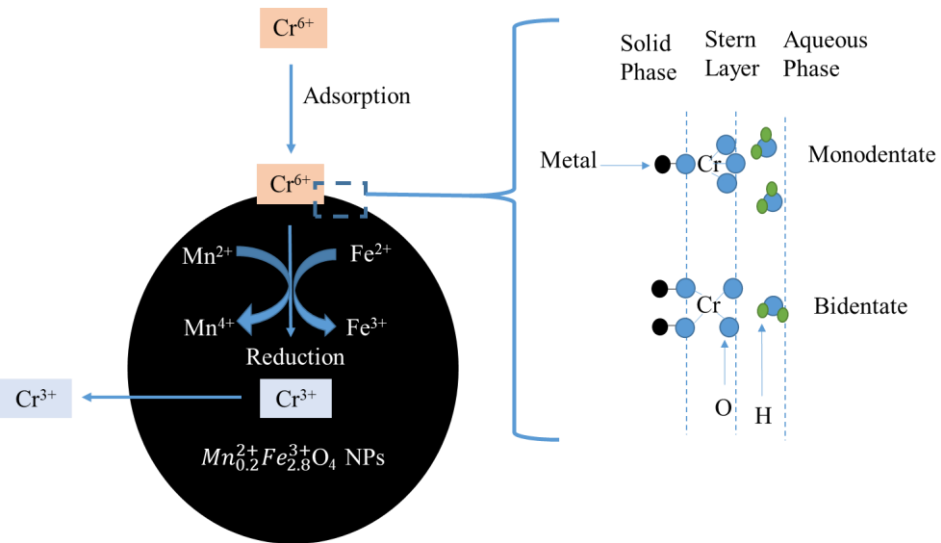


Figure 31: Scheme for Cr^{6+} adsorption-reduction by NPs. Redrawn from Xie et al.²¹³ and Johnston and Chrysochoou.²¹²

3.4 Conclusion

Citrate-coated $Mn_{0.2}^{2+}Fe_{2.8}^{3+}O_4NPs$ (prepared from Mn^{2+} precursor at a synthesis temperature of 250 °C for 6 h) showed the highest Cr^{6+} adsorption capacity (16.8 ± 1.6 mg/g). Langmuir isotherm model fitted the adsorption of Cr^{6+} by the $Mn_{0.2}^{2+}Fe_{2.8}^{3+}O_4NPs$ as a function of the initial Cr^{6+} concentrations at pH 7 at room temperature. $Mn_{0.2}^{2+}Fe_{2.8}^{3+}O_4NPs$ NPs can reduce 61% of the adsorbed Cr^{6+} into Cr^{3+} . Because of the highest adsorption capacity, $Mn_{0.2}^{+2}Fe_{2.8}^{+3}O_4NPs$ were selected to explore their impact on the bio-reduction of Cr^{6+} by *S. oneidensis* MR-1 compared to undoped Fe₃O₄ and Mn₃O₄ NPs.

Chapter 4. Enhancing the bio-detoxification efficiency of *Shewanella oneidensis* MR-1 for Cr⁶⁺ by the selected Mn_xFe_{3-x}O₄ NPs

4.1 Introduction

The remediation of the carcinogenic Cr⁶⁺ needs not only its removal (elimination) from the waste stream but also its reduction (detoxification) to a less harmful form, Cr³⁺. Some microbes that can survive in heavy metal-contaminated places are used for the bioreduction (bio-detoxification) of Cr⁶⁺ to Cr³⁺. *S. oneidensis* MR-1 bacteria are a model metal-reducing microbe recommended for heavy metal removal,^{3,58-60} as was explained in Chapter 1, section 1.2 in more detail.

Several factors affect the bio-reduction efficiency of *S. oneidensis* MR-1 to Cr⁶⁺. Using starch as an electron source caused the reduction of 90% of Cr⁶⁺ by *S. putrefaciens* bacteria, followed by 1% glucose (88% reduction) and 77% by 1% cellulose.²¹⁴ The presence of oxygen inhibited the bio-reduction of Cr⁶⁺ by *S. oneidensis* MR-1.⁶⁶ The bioremoval of Cr⁶⁺ was reported to be maximised at pH 7-8,^{214,215} temperature 35°C, contact time of 16.57 h, and biomass dosage of 0.42 g/L.²¹⁵

The reduction of Cr^{6+} by *S. oneidensis* MR-1 had an inverse relationship with its concentration, 66,78,114 because of the cytotoxicity of Cr^{6+} to *Shewanella*. $^{9,78,82,111-113}$ *S. oneidensis* MR-1 strain alone can reduce 26-78 % of 20 mg/L of Cr^{6+} into Cr^{3+} within

8 h. $^{78-80}$ The bio-reduction efficiency is much lower than what can be detoxified by physical and chemical materials. 58 The lethal dose of Cr^{6+} at which *S. oneidensis* MR-1 cannot show a visible growth was reported to be $\sim 42\text{-}65$ mg/L. $^{73.82}$ Cr^{6+} was suggested to cause mutations that affected growth or non-reversible interaction with proteins that inhibited growth. 82 The loss in viability of *S. oneidensis* MR-1 after Cr^{6+} treatment was suggested to be because of the intracellular effects of Cr^{6+} . Yet, the concentration of $Cr^{3+}/^{6+}$ in industrial effluents may be reached 1000-1500 mg/L as reviewed by Mpofu et al. 115 Therefore, enhancing the bacterial tolerance to Cr^{6+} was considered an effective way to enhance the bio-reduction efficiency of Cr^{6+} by *S. oneidensis* MR-1.

Adsorption is a simple and effective technique for removing metals from waste streams. Integrating the adsorption-bio-reduction method is effective for Cr⁶⁺ safe removal, i.e. elimination and reduction. The synergism of *S. oneidensis* MR-1 and other specific nanostructures is the most common method for promoting Cr⁶⁺ reduction. These materials promote heavy metal respiration by *S. oneidensis* MR-1 in different ways. Such chemicals can enhance the bio-reduction of Cr⁶⁺ by acting as electron shuttles, catalysts and reducing agents.⁶⁷

Chapter 4 assesses the impact of $Mn_{0.2}^{2+}Fe_{2.8}^{3+}O_4$ NPs (that showed the highest Qe to Cr^{6+}) on the removal efficiency of Cr^{6+} by *S. oneidensis* MR-1. The effect of $Mn_{0.2}^{2+}Fe_{2.8}^{3+}O_4$ NPs on the viability of *S. oneidensis* MR-1 in response to Cr^{6+} have been studied by flow cytometry. Subsequently, the colourimetric method has investigated their impact on the bio-removal of Cr^{6+} by *S. oneidensis* MR-1. The modification in the morphology of *S. oneidensis* MR-1 cells after being exposed to Cr^{6+} in the presence of

 $Mn_{0.2}^{2+}Fe_{2.8}^{3+}O_4$ NPs were imaged using Scanning Electron Microscopy (SEM). The change in the oxidation state of Cr^{6+} after the interaction with *S. oneidensis* MR-1 in the presence $Mn_{0.2}^{2+}Fe_{2.8}^{3+}O_4$ NPs were studied using X-ray Photoelectron Spectroscopy (XPS) to reveal any redox interaction.

4.2 Materials and methods

Fe₃O₄ NPs, $Mn_{0.2}^{2+}Fe_{2.8}^{3+}O_4$ NPs (both were prepared at 250 °C for 6 h as synthesis temperature and time, respectively) and Mn_3O_4 NPs were used as prepared in Chapter 2. Fe₃O₄ NPs and Mn_3O_4 NPs were used as Mn-free and Fe-free controlling NPs, respectively, for $Mn_{0.2}^{2+}Fe_{2.8}^{3+}O_4$ NPs. Chemicals and techniques used for quantifying the efficiency of Cr^{+6} bio-removal and the reduction mechanism were described in sections 3.2.1 and 3.2.2.

4.2.1 For microbiological studies

Both forward primer (1369F) of sequence CGGTGAATACGTTCYCGG and reverse primer (1492R) of sequence GGWTACCTTGTTACGACTT were obtained from Integrated DNA Technology (UK) in a dry form. FastDNA Spin Kit for Soil was purchased from MP Biomedicals, UK. Invitrogen, UK supplied the Qubit dsDNA broad range (2 to 1000 ng) assay kit and DNase/RNase-free sterile ultrapure distilled water. From New England Biolabs (UK), Luna Universal qPCR Master Mix was obtained. Vitamin and trace mineral supplements (MD-VSTM and MD-TMSTM, respectively) were procured from American Type Culture Collection (ATCC, UK). Live-dead BacLight bacterial viability test kit and M9 minimal salts (2x) medium were obtained from

ThermoFisher, UK. Luria–Bertani agar (LB) medium was bought from Oxoid, UK. Glutaraldehyde (25%), phosphate buffer saline (PBS), sodium DL-lactate (≥99.0%), sodium fumarate dibasic (≥99.0%) and 4-(2-hydroxyethyl)-1-piperazine-ethanesulfonic acid (HEPES, ≥99.5%) were obtained from Sigma-Aldrich (UK). Microbank[™] Cryobeads were purchased from Pro-Lab Diagnostics, UK.

4.2.2 Sources of bacteria of interest

Freeze-dried cultures of Shewanella oneidensis MR-1 (strain number LMG 19005) Belgian Coordinated Collections acquired from of were Microorganisms/Laboratory for Microbiology of Ghent University (BCCM/LMG). Shewanella loihica PV-4 (strain number DSMZ 17748) was obtained from Leibniz-Institut DSMZ-Deutsche Sammlung von Mikroorganismen und Zellkulturen GmbH and used as a positive biological control for microbial reduction of Cr⁶⁺. Professor Jeffrey A. Gralnick kindly provided S. oneidensis JG1486 and JG3355 as LB agar stabs cryovials. These strains were used as negative biological controls. The dried bacteria were recovered via streaking on LB agar plates and incubated for 18 h at 37 °C. Colonial growth from all cultures was stored after being preserved on Cryobeads at -80 °C.

4.2.3 Molecular identification of the tested bacteria

The Genomic DNA of bacteria was extracted by boiling a single colony in ultrapure water for 10 min at 95 °C. Then, FastDNA Spin Kit for Soil was applied to the boiled broth following the manufacturer's instructions.

Amplification of 16S rRNA gene fragment for the tested strains was done by polymerase chain reaction (PCR) using 1369F and 1492R primers and Luna Universal qPCR Master Mix. Using thermocycler (Cole-Parmer), the solution mixture, including the extracted nucleic acid, primers and the master mix was heated to 94 °C for 5 min as an initial step for the denaturation of double-stranded DNA into single-stranded one followed by a denaturation for 45 s. Next, the annealing step was done by heating the mixture at 52 °C for 45 s to allow the primers and polymerase enzyme from the mixture solution to bind to the single strands of DNA. Finally, the extension of DNA by adding nucleotides was processed at 72 °C for 90 s to form a new complementary strand of DNA. The denaturation, annealing and extension of DNA were repeated ~ 30 cycles. Qubit 3.0 fluorometer (Life Technologies, UK) was used to quantify the amount of DNA in PCR products via Qubit dsDNA broad-range assay.

Both the purification of amplified PCR products and Sanger sequencing were implemented using the commercial service of Source Bioscience, Cambridge, UK. The sequenced data were assigned for matching identity for species with the highest fitting 96-100 % by nucleotide BLAST (Basic Local Alignment Search Tool) from the database of the National Centre for Biotechnology Information (NCBI) (https://blast.ncbi.nlm.nih.gov).

4.2.4 Microbial viability under Cr6+ stress

A. Minimum inhibition concentration of Cr^{6+}

To assess the impact of Cr^{6+} on the viability of the tested *Shewanella* spp, a Guava easyCyte® flow cytometer (Merck, UK) was used. 10 μ L of homogeneous bacterial cell suspensions with OD measured at $\lambda600$ nm equal to 0.1 was added to 80 μ L of M9 minimal salts (x 2) medium. ²¹⁷ This medium was supplemented by 20 mM sodium lactate as a sole electron source, 5 mL/L each of vitamins and minerals and pH was adjusted to 7.2 by 10 mM HEPES buffer. ²¹⁸ The viability of cells was quantified in response to serial dilutions of Cr^{6+} (1 to 100 mg/L) as a terminal electron source alone. Sodium fumarate (20 mM) was used as an alternative terminal electron acceptor to Cr^{6+} . In all cases, media were purged with nitrogen gas for 5 min after bacterial inoculation. The proportion of live cells was quantified relative to the overall number of cells via live-dead BacLight bacterial viability assay. The gating strategy of the bacterial cells' live and dead populations was defined based on fluorescence minus one (FMO). ²¹⁹ Data of 3 replicates are expressed as means \pm standard deviation. The minimum inhibitory concentration (MIC) of any agent was defined as its lowest concentration that inhibits the growth of bacteria after overnight incubation. ²¹⁹

B. Viability of the tested Shewanella to the Fe_3O_4 , $Mn_{0.2}^{2+}Fe_{2.8}^{3+}O_4$ NPs, $MnFe_3O_4$ NPs

The impact of tri-sodium citrate and citrate-coated Fe_3O_4 , $Mn_{0.2}^{2+}Fe_{2.8}^{3+}O_4$ NPs and $MnFe_3O_4$ NPs on the viability of the tested *Shewanella* were assayed in the presence and

absence of the sub-lethal dose of Cr⁶⁺ using Guava easyCyte® flow cytometer (Merck, UK) following the protocol maintained above in section 4.2.4.A.

C. Imaging bacteria by Scanning Electron Microscopy (SEM)

The samples were imaged by Philips XL30 FEG SEM (FEI, Eindhoven, Netherlands) with an accelerating voltage of 5 keV. To acquire SEM images, $50 \,\mu\text{L}$ from the cell suspension of the untreated and treated *S. oneidensis* MR-1 bacteria by $Mn_{0.2}^{2+}Fe_{2.8}^{3+}O_4$ NPs alone and by Cr^{6+} in the presence and absence of $Mn_{0.2}^{2+}Fe_{2.8}^{3+}O_4$ NPs were deposited on microscope cover glass (Fisher, UK) and left to be air-dried for 1h at room temperature. At room temperature, cells were fixed by immersing the glass covers in glutaraldehyde (2.5% v/v in 0.01 M PBS) for 30 min. Next, the fixed cells were washed 3 times with PBS [0.01 M]. The slides were dipped consequently in a serial dilution of ethanol (10% v/v in distilled water, 30% v/v, 50% v/v, 70% v/v and 90% v/v), then finally 100% of ethanol for 5 min per each concentration for dehydration. The slides were then attached to aluminium stubs with double-sided carbon tape (Agar Scientific, UK). Samples were then sputter-coated with gold-palladium at 20 mA and 1.25 Kv for 90 seconds using a Palaron E5000 sputter coater.

4.2.5 Integrated adsorption bio-reduction safe removal of Cr6+

A. Biological removal of Cr^{6+} by the tested Shewanella

 Cr^{6+} bio-removal efficiency in response to NPs presence was tested at Cr^{6+} sub-lethal dose for the tested bacteria. For *S. oneidensis* MR-1 and *S. loihica* PV-4, the sub-lethal concentration of Cr^{6+} was 50 mg/L. 10 and 1 mg/L of Cr^{6+} for *S. oneidensis* JG1486

and JG3355 were defined as sub-lethal doses. The concentration of citrate was 0.1 mM, and citrate-coated, Fe_3O_4 , $Mn_{0.2}^{2+}Fe_{2.8}^{3+}O_4$ NPs and Mn_3O_4 NPs were adjusted to 1 mg/mL. The remaining soluble Cr^{6+} in the supernatant (Cr_S) passed through a 0.45 μ m filter membrane and was quantified using the Cr^{3+} -DPC complex method ^{198,199} described in section 3.2.3.A. The percentage of Cr^{6+} bio-reduction was calculated in relation to the initial concentration (Cr_i) of Cr^{6+} following: ^{82,92}

Bioremoval (%) =
$$\left(\frac{\operatorname{Cr}_i - \operatorname{Cr}_s}{\operatorname{Cr}_i}\right) x 10$$

B. Microbial detoxification of Cr^{6+}

The change in oxidation states of Cr⁶⁺ after being incubated with *S. oneidensis* MR-1 alone and Mn²⁺_{0.2}Fe³⁺_{2.8}O₄ NPs and *S. oneidensis* MR-1 were analysed by XPS (a Kratos Analytical AXIS Ultra^{DLD} system) under similar environments as mentioned above in section 3.2.4.

4.2.6 Statistical analysis

The effect of $Mn_xFe_{3-x}O_4$ NPs on microbial viability and detoxification of Cr^{6+} was studied using a statistical Students t-test. The significance level was described as a calculated probability (P) < 0.05 (*) and P < 0.01 (**). All experiments were done in triplicates except SEM and XPS were done once.

4.3 Results and discussion

4.3.1 Molecular identification of the tested Shewanella

Shewanella bacterial species are metal-reducing and metal-resistant bacteria. 82 The tested wild-type *S. oneidensis* MR-1, *S. loihica* PV-4, *S. oneidensis* JG1486 and JG3355 were identified by sequencing fragments of their 16s rRNA genes. Our results illustrated that the sequence of 16s rRNA genes of *S. oneidensis* MR-1 and *S. loihica* PV-4 matched *S. putrefaciens* (NCBI Reference Sequence NR_113582) by 98.90 % and 100 %, respectively. *S. oneidensis* JG3355 showed similarity to *S. pealeana* (NCBI Reference Sequence: NR_114421) by 100 %. The sequence of 16s rRNA of *S. oneidensis* JG1486 was similar to *S. oneidensis* MR-1 (NCBI Reference Sequence: NR_074798.1) by 96.4 %.

4.3.2 The viability of the tested *Shewanella* under Cr⁶⁺ stress in the presence of the selected Mn_xFe_{3-x}O₄ NPs

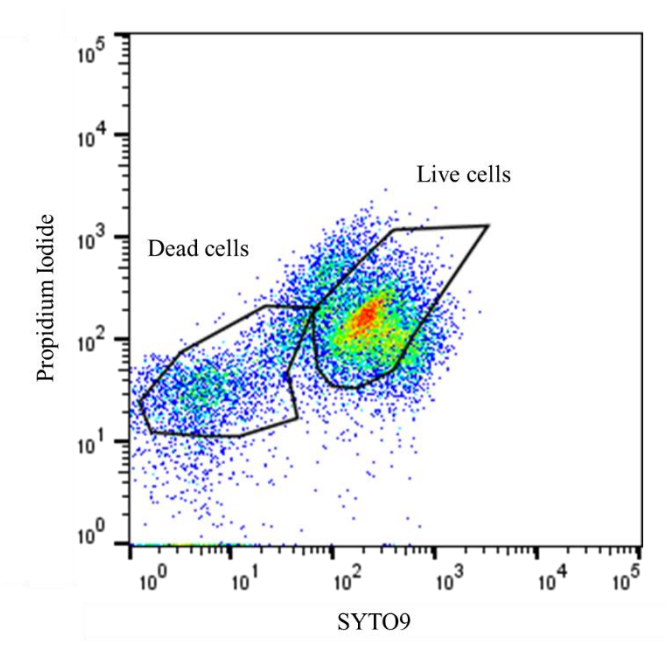


Figure 32: Gating strategy for identifying the live and dead cell bacterial populations acquired by flow cytometry.

The viability of the tested *Shewanella* was quantified via flow cytometry following live-dead gates, as shown in *Figure 32*. Gating is a method to define a category of data in flow cytometry. A dot plot represented the cell count, and each dot represented an event related to a cell.²²¹

A. Determination of lethal dose of Cr^{6+} for the tested Shewanella

Under redox conditions, our results revealed that the minimum inhibition concentrations (MICs) of Cr⁶⁺ for the tested wild-type *Shewanella* strains (*S. oneidensis* MR-1 and *S. loihica* PV-4) were 60 mg/L and 70 mg/L, respectively, as shown in *Figure*

33~A which was slightly within the reported range. 73,82 Cr $^{6+}$ uptake by *Shewanella* intracellularly caused cell lysis. 222 Cr $^{6+}$ could damage microbial DNA when they enter the cells. 222 The toxic effect of Cr $^{6+}$ appeared to be associated with extracellular interactions leading to a change in the cellular morphology and then a lethal effect. 78,82,92,222

The extracellular reduction of Cr⁶⁺ to Cr³⁺ promoted the survival of *S. oneidensis* MR-1 and *S. loihica* PV-4, as shown in *Figure 33 A*.^{78,82,92,222} The ability of *Shewanella* to transfer electrons to metal ions was known to take place via MtrCAB complex,¹⁰⁰ MtrFED complex,¹⁰¹ DmsEFA DMSO reductase system¹⁰² and SO4359–SO4360 system.¹⁰¹ The slightly higher tolerance of *S. loihica* PV-4 to Cr⁶⁺ than *S. oneidensis* MR-1 in our experiment (*Figure 33 A*) was thanks to their higher content of *c*-type cytochrome genes than *S. oneidensis* MR-1.²²³ In addition, *S. loihica* PV-4 cells were reported to be elongated and exhibited a rough surface upon exposure to Cr⁶⁺.²²² This adaptation of cellular morphology in response to Cr⁶⁺ can explain why *S. loihica* PV-4 showed higher resistance for Cr⁶⁺.

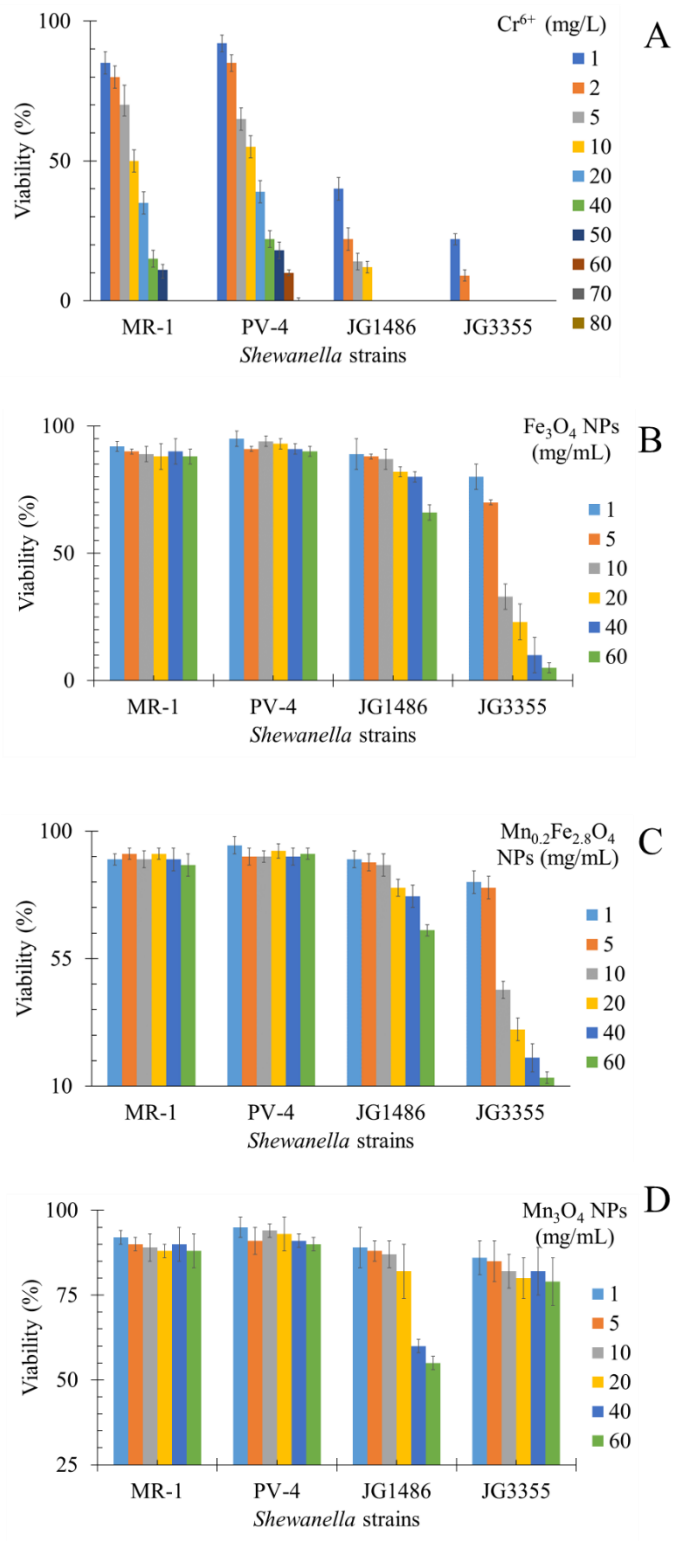


Figure 33: Viability of the tested Shewanella strains in response to (A) Cr^{6+} , (B) Fe_3O_4 NPs, (C) $Mn_{0.2}^{2+}Fe_{2.8}^{3+}O_4$ NPs and (D) Mn_3O_4 NPs.

The lower MIC of Cr^{6+} to *S. oneidensis* JG1486 (20 mg/L) than *S. oneidensis* MR-1 and *S. loihica* PV-4 could be a supportive argument for the critical role of the extracellular reduction of metal as a strategy by *Shewanella* for coping the bactericidal effect of Cr^{6+} . The missing responsible genes for the extracellular metal reduction in *S. oneidensis* JG1486 (Δ mtrCAB, Δ mtrFED, Δ omcA, Δ dmsE, Δ SO4360, Δ cctA and Δ recA) was reported to be the causative agent for inhibiting the viability of *S. oneidensis* JG1486 cannot respire metals. ¹⁰⁴ This could be the reason for the low tolerance level of *S. oneidensis* JG1486 to Cr^{6+} , as shown in *Figure 33 A*.

S. oneidensis JG1486 was more tolerant to Cr⁶⁺ than S. oneidensis JG3355 of MIC equal to 5 mg/L. S. oneidensis JG3355 lacked the responsible genes for regulating Fe²⁺ stress in anaerobic bacteria (ClpX and ClpP).²²⁴ ClpP gene encoded protease proteins which were reported to be expressed in response to the exposure of S. oneidensis MR-1 to Cr⁶⁺ for 24 h.²²⁵ The possibility of lacking metal-reducing responsible proteins¹⁰⁴ in S. oneidensis JG1486 and stress regulators made such protease^{224,225} in S. oneidensis JG3355 could be the reasons for the ability of both strains to survive under Cr⁶⁺ stress.

B. Cellular compatibility of the selected Mn_xFe_{3-x}O₄ NPs

In the absence of Cr⁶⁺, Fe₃O₄ NPs can sustain the viability of bacteria, as presented in *Figure 33 B. S. putrefaciens* can respire Fe₃O₄ under anaerobic conditions and convert millimolar amounts of Fe₃O₄ to soluble Fe²⁺ at pH 5-6 and a temperature range of 22-37 °C.^{224,226} So, the viability of *S. oneidensis* MR-1 and *S. loihica* PV-4 were maintained in the presence of the tested concentration range of Fe₃O₄ NPs under anaerobic conditions, as shown in *Figure 33 B*.

As described above, the *S. oneidensis* JG1486 strain cannot respire Fe₃O₄ NPs due to missing the responsible genes for extracellular metal reduction.¹⁰⁴ Under anaerobic conditions, the lethal effect of Fe²⁺ on *S. oneidensis* cells was attributed to the substitution of Mg²⁺ of lower protein binding affinity in metalloprotein by Fe²⁺. Protease enzymes that were encoded by ClpXP genes can detect and degrade mis-metallated, misfolded proteins.²²⁴ So, *S. oneidensis* JG3355 was sensitive to Fe₃O₄ NPs in our results due to the deletion of both ClpX and ClpP genes.²²⁴

Shewanella species can grow in the presence of Mn,²²⁷ which was supported by our results in *Figure 33 C* and *D*. The Mn content in the chemical structure of Mn_{0.2}²⁺Fe_{2.8}³⁺O₄ NPs and Mn₃O₄NPs improved the anti-oxidant activity of NPs and, in turn, the viability of cells.²²⁸ The ability of *S. oneidensis* MR-1 to respire Mn⁴⁺ and Mn³⁺ into Mn²⁺ has already been reported.^{229,230} The presence of Mn²⁺ in Mn_{0.2}²⁺Fe_{2.8}³⁺O₄ NPs decreased Fe²⁺ concentration in the solution and, in turn, decreased the lethal effect of Fe²⁺ on the viability of the tested *Shewanella* in general and *S. oneidensis* JG3355 in particular. Exposing *S. oneidensis* JG3355 to 1mg/mL of Fe₃O₄ NPs or Mn_{0.2}²⁺Fe_{2.8}³⁺O₄ NPs did not impact the viability of *S. oneidensis* JG3355. So, this concentration was applied for further experiments for all the tested *Shewanella* strains.

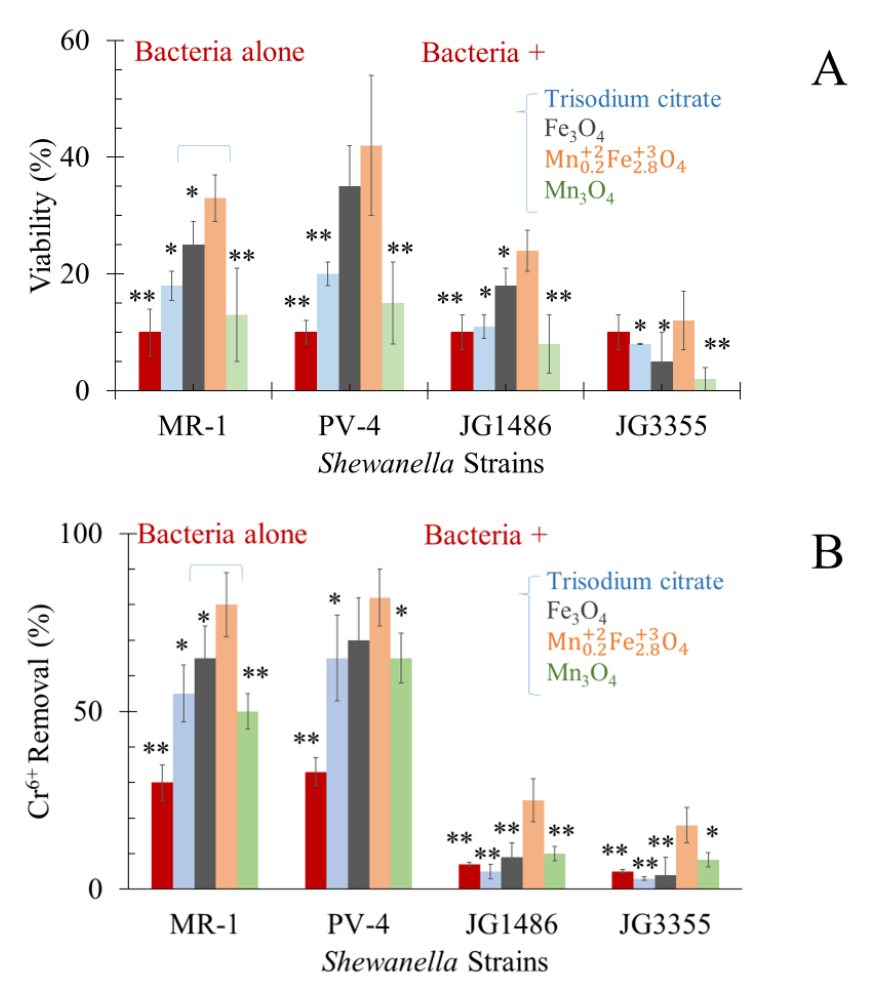


Figure 34: In the presence of the tested agents: (A) the viability of tested Shewanella under a sublethal dose of Cr^{6+} , (B) the removal of Cr^{6+} by Shewanella strains. *P < 0.05 and **P < 0.01 in relation to the impact of $Mn_{0.2}^{2+}Fe_{2.8}^{3+}O_4$ NPs in each data set separately.

C. Sustaining the viability of Shewanella at a sub-lethal concentration of Cr^{6+} by the selected $Mn_xFe_{3-x}O_4$ NPs

In the presence of citrate only, the viability of *S. oneidensis* MR-1 and *S. loihica* PV-4 bacteria was improved only 10-12 % at the sub-lethal dose of Cr^{6+} (50 mg/L), as

illustrated in *Figure 34 A*. Bencheikh-Latmani *et al.*²³¹ explained a similar observation due to the possible interaction between bio-reduction product (Cr^{3+}) and citrate.²³¹ The Formation of the Cr^{3+} -citrate complex restricted the availability of the toxic metal to bacterial cells.²³¹

Employing Mn²⁺_{2,8}Fe³⁺_{2,8}O₄ NPs as adsorbents can minimise the exposure of *Shewanella* cells to Cr^{6+, which can boost bacterial tolerance to Cr^{6+, 9,78} The positive relationship between Cr⁶⁺ adsorption and the viability of bacteria was reported. Cr⁶⁺ was adsorbed on Mn²⁺_{0,2}Fe³⁺_{2,8}O₄ NPs following Langmuir adsorption isotherm model (*Figure 26*). Based on this model, the possible continuous adsorption-desorption rate of Cr⁶⁺ can sustain a bombardment of Cr⁶⁺ from the surface of NPs, which makes the exposure of cells to Cr⁶⁺ occur at a gradual rate. In addition, our reported reduction of the highly toxic Cr⁶⁺ into less toxic Cr³⁺ by Mn²⁺_{0,2}Fe³⁺_{2,8}O₄ NPs, as approved in our results in *Figure 29*, can protect bacterial cells from the toxic effect of Cr⁶⁺. Moreover, the binding affinity of Mn²⁺ to proteins was ranked lower than Fe²⁺ according to the natural order of stability for divalent transition metals. ^{232,233} This weak contact between the adsorbed Cr⁶⁺ on Mn²⁺_{0,2}Fe³⁺_{2,8}O₄ NPs and bacterial cells can enable *S. oneidensis* MR-1 to survive under Cr⁶⁺. This controlled attachment can avoid the reported disruption of the electron transfer from *S. oneidensis* MR-1 to Cr⁶⁺ due to the high affinity of *S. oneidensis* MR-1 and α-FeOOH. ⁷⁸}

The use of $Mn_{0.2}^{2+}Fe_{2.8}^{3+}O_4$ NPs improved the viability of *S. oneidensis* MR-1 under the sub-lethal concentration of Cr^{6+} by 2.3 times. In response to Cr^{6+} toxicity, the presence of $Mn_{0.2}^{2+}Fe_{2.8}^{3+}O_4$, Fe_3O_4 and Mn_3O_4 NPs improved the viability of *S. oneidensis* JG1486

strain by 5-, 3.5-, 2-fold, and of *S. oneidensis* JG5533 strain by 3.6-, 6.25-, 1.5-fold, respectively. The deletion of ClpP gene in *S. oneidensis* JG3355 224 affected the ability of the mentioned strain to respond to 24 h Cr $^{6+}$ exposure. 225

4.3.3 Bio-removal efficiency of Cr^{6+} by combining the tested *Shewanella* strains and the selected $Mn_xFe_{3-x}O_4$ NPs

The capability of *S. oneidensis* MR-1⁷⁸ to respire Cr^{6+} was affected by the initial concentration of the heavy metal. ^{9,78,234} These results were credited to the chromate dosedependent toxicity, which causes growth and viability inhibition. ^{9,78,234} Hence, our experiments were designed at high concentrations of Cr^{6+} , i.e. sub-lethal dose. The viability of the tested *Shewanella* and the bio-removal of Cr^{6+} was correlated, as shown in *Figure 34 A and B*.

A. Eliminating Cr^{6+} by the tested Shewanella alone

Our results (*Figure 34 B*) revealed a significant drop in the concentration of Cr^{6+} in the media supplemented by both wild types of the strain of interest (*S. oneidensis* MR-1) and positive control (*S. loihica* PV-4). The bio-removed Cr^{6+} by the abovementioned wild-type of *Shewanella* were 30 ± 5 % and 33 ± 4 %, respectively, in the reported range of 18.3-42 %.^{78,141} For all tested *Shewanella*, the percentages of viable cells were approximately similar (~ 10 %). However, the bio-removal of Cr^{6+} by the mutant stains (*S. oneidensis* JG1486 and *S. oneidensis* JG5533) were 7 ± 1 % and 5 ± 0.5 %, respectively. The efficiency of Cr^{6+} removal by *S. oneidensis* JG1486 and JG5533 (negative biological controls) was lower than what was removed via *S. oneidensis* MR-1

by approximate ranges from 3.13 to 5.53 times and from 5.63 to 6.85 times, respectively as shown in *Figure 34 B*. The low concentration of Cr⁶⁺ was suggested to induce mutations that caused non-reversible interaction with proteins that inhibited growth.⁸² More than one strategy for Cr⁶⁺ removal by *Shewanella* could be involved, such as the respiration of Cr⁶⁺ into Cr³⁺ form ^{79,92,235} and bio-sorption by bacterial cells, either absorption or adsorption.^{116,215}

B. Removing Cr^{6+} in the presence of Shewanella and tri-sodium citrate

The presence of tri-sodium citrate improved the bio-removal of Cr^{6+} via S. oneidensis MR-1 and S. loihica PV-4 by 1.8 and 2 times, respectively, as illustrated in Figure 34 B, which could be a result of the possible complexation $Cr^{3+}.^{231}$ Also, S. oneidensis JG1486 and S. oneidensis JG5533 strain to remove Cr^{6+} were minimised to 70 and 60 % by citrate, respectively.

C. Improving the bio-removal of Cr^{6+} by combining Shewanella and Fe_3O_4 NPs

Fe₃O₄ NPs increased the bio-removal of Cr⁶⁺ via *S. oneidensis* MR-1 and *S. loihica* PV-4 by 2.2 and 2.1 times, respectively, as illustrated in *Figure 34* B. The reactivity of Fe₃O₄ towards Cr⁺⁶ was enhanced by microbial reduction of Fe³⁺ via *Geobacter sulfurreducens*.¹³⁷ α-FeOOH boosted the Cr⁶⁺ detoxification by *S. oneidensis* MR-1 and *S. putrefaciens* CN32 20-30 %⁹ and 60%, respectively.¹¹ Fe₃O₄ NPs increased Cr⁶⁺ elimination via *S. oneidensis* JG1486 by 1.3 times. *S. oneidensis* JG5533 strain lost 20 % of its ability to remove Cr⁶⁺ in the presence of Fe₃O₄ NPs.

D. Enhancing the elimination efficiency of Cr^{6+} by using both Shewaenlla and Mn_3O_4 NPs

The presence of Mn₃O₄ NPs increased the bio-removal of Cr⁶⁺ via *S. oneidensis* MR-1 and *S. loihica* PV-4 by 1.7 and 2 times, respectively, as illustrated in *Figure 34 B*. Mn₃O₄ NPs boosted the efficiency of *S. oneidensis* JG1486 and *S. oneidensis* JG5533 to eliminate Cr⁶⁺ by 1.4 times and 1.7 times, respectively.

E. Boosting the removal efficiency of Shewanella for Cr^{6+} by $Mn_{0.2}^{2+}Fe_{2.8}^{3+}O_4$ NPs

The presence of $Mn_{0.2}^{2+}Fe_{2.8}^{2+}O_4$ nano-adsorbent was beneficial to microbial survival, as approved in our results in *Figure 34 A*, which was positively related to enhancing Cr^{6+} bio-removal via *S. oneidensis* MR-1 and *S. loihica* PV-4 by 2.7 and 2.5 times (*Figure 34 B*). $Mn_{0.2}^{2+}Fe_{2.8}^{3+}O_4$ NPs can facilitate the electron transfer from cells to the acceptor²³⁶ by electron-accepting and -donating through NPs. The affinity of $MnFe_2O_4$ NPs to bind proteins on the bacterial outer membrane can improve the contact area between a single bacterium and an external electron acceptor.¹⁵¹ The presence of $Mn_{0.2}^{2+}Fe_{2.8}^{3+}O_4$ NPs boosted the efficiency of *S. oneidensis* JG1486 and *S. oneidensis* JG5533 to eliminate Cr^{6+} by 3.6 times each strain.

Studying the morphological change of *S. oneidensis* MR-1 (the bacteria of interest) by SEM and the oxidation state of Cr elements by XPS after their interaction in the presence of $Mn_{0.2}^{2+}Fe_{2.8}^{3+}O_4$ NPs would achieve a better understanding of the promoting impact of NPs.

4.3.4 Enhanced morphological response of S. oneidensis MR-1 to Cr^{6+} by the selected $Mn_xFe_{3-x}O_4$ NPs

A. Rod shape of untreated S. oneidensis MR-1 cells

Before contacting with Cr⁶⁺, the wild-type *S. oneidensis* MR-1 was imaged as regular rod-shaped cells with smooth surfaces, as shown in *Figure 35 A*, which matched what was documented in other reports.^{78,82,92,222} A cell division ring (Z-ring) per bacterial cell was observed in *Figure 35 A*, an indicator for the earliest phase of cell division of *S. oneidensis* MR-1 cells.⁸² Parker et al.⁸² reported that the delay in separating daughter cells could be attributed to the limited availability of nutrients in the media.⁸² The presence of bacterial nanowires as extensions of the outer membrane and periplasm (*Figure 35 A*) was shown to be increased under oxygen-limited conditions.¹⁰⁸ Nanowires were reported to have the responsible multiheme cytochromes for extracellular electron transport pathways for external electron acceptor respiration.¹⁰⁸

B. Rupture of S. oneidensis MR-1 cells in response to Cr^{6+}

SEM images of *S. oneidensis* MR-1 revealed the inability of bacterial cells to produce nanowires after exposure to Cr^{6+} . The variation in the length of cells exposed to Cr^{6+} is presented in *Figure 35 B* and *Table 3* as a coping strategy for tolerating the stress induced by Cr^{6+} . The impact of exposure of *S. oneidensis* MR-1 to the sublethal dose of Cr^{6+} was observed on the rupture on the one pole of the cell as shown in *Figure 35 B* shrunken-surface shape and crack formation in bacterial cells were also observed after

the reaction with $Cr.^{78,82,92}$ The attempts of cell division were imaged for cells exposed to Cr^{6+} .

C. Cellular compatibility of $Mn_{0.2}^{2+}Fe_{2.8}^{3+}O_4$ NPs

Incubating bacterial cells with $Mn_{0.2}^{2+}Fe_{2.8}^{3+}O_4$ NPs resulted in an insignificant decrease in the length and diameter of the bacterial cells, as shown in *Figure 35* C and *Table 3*. The deposition of MnFe₂O₄ NPs on the surface of *S. putrefaciens* CN32 showed no morphological impact, which supported our results as shown in *Figure 35* C. The poles of *Shewanella* cells are attractive to the metal oxide/hydroxides under aerobic and anaerobic conditions, which explains the polar rupture of some cells. The capability of *Shewanella* to produce nanowires in the presence of $Mn_{0.2}^{2+}Fe_{2.8}^{3+}O_4$ NPs were seen.

D. Enhanced tolerance of Shewanella to Cr^{6+} by $Mn_{0.2}^{2+}Fe_{2.8}^{3+}O_4$ NPs

In the presence of $Mn_{0.2}^{2+}Fe_{2.8}^{3+}O_4$ NPs, the surface of the treated *S. oneidensis* MR-1 cells by Cr^{6+} retained a smooth but elongated morphology (see *Figure 35 D* and *Table 3*). Cr^{6+} induced the stretched shapes of cells for *S. loihica* PV-4 in the presence of a mixture containing both biochar and α -Fe₂O₃. 239 $Mn_{0.2}^{2+}Fe_{2.8}^{3+}O_4$ NPs provoked the formation of bacterial nanowires in the presence of Cr^{6+} , as depicted in *Figure 35 D*. The ability of NPs to regenerate the bacterial nanowire production agrees with the findings reported by Yu et al. 240 Such observation in response to the interaction between Mn_xFe_{3-} xO_4 NPs and cells was confirmed in the present work by EM.

Table 3: Quantitative variation in the length and diameter of S. oneidensis MR-1 bacterial cells in response to the tested treatment.

S. oneidensis MR-1	Cell length (μm) ^a	Cell diameter (µm) ^b
Untreated	2.15 ± 0.45	0.6 ± 0.06
Treated by Cr ⁶⁺ alone	2.3 ± 0.78	0.65 ± 0.15
Treated by Mn _{0.2} ²⁺ Fe _{2.8} ³⁺ O ₄ NPs alone	2.1 ± 0.85	0.56 ± 0.15
Treated by both Cr ⁶⁺ and Mn _{0.2} ²⁺ Fe _{2.8} ³⁺ O ₄ NPs	2.5 ± 0.9	0.7 ± 0.09

^aLength and ^bdiameter were presented as (mean \pm standard deviation) of 50 measured cells from SEM images.

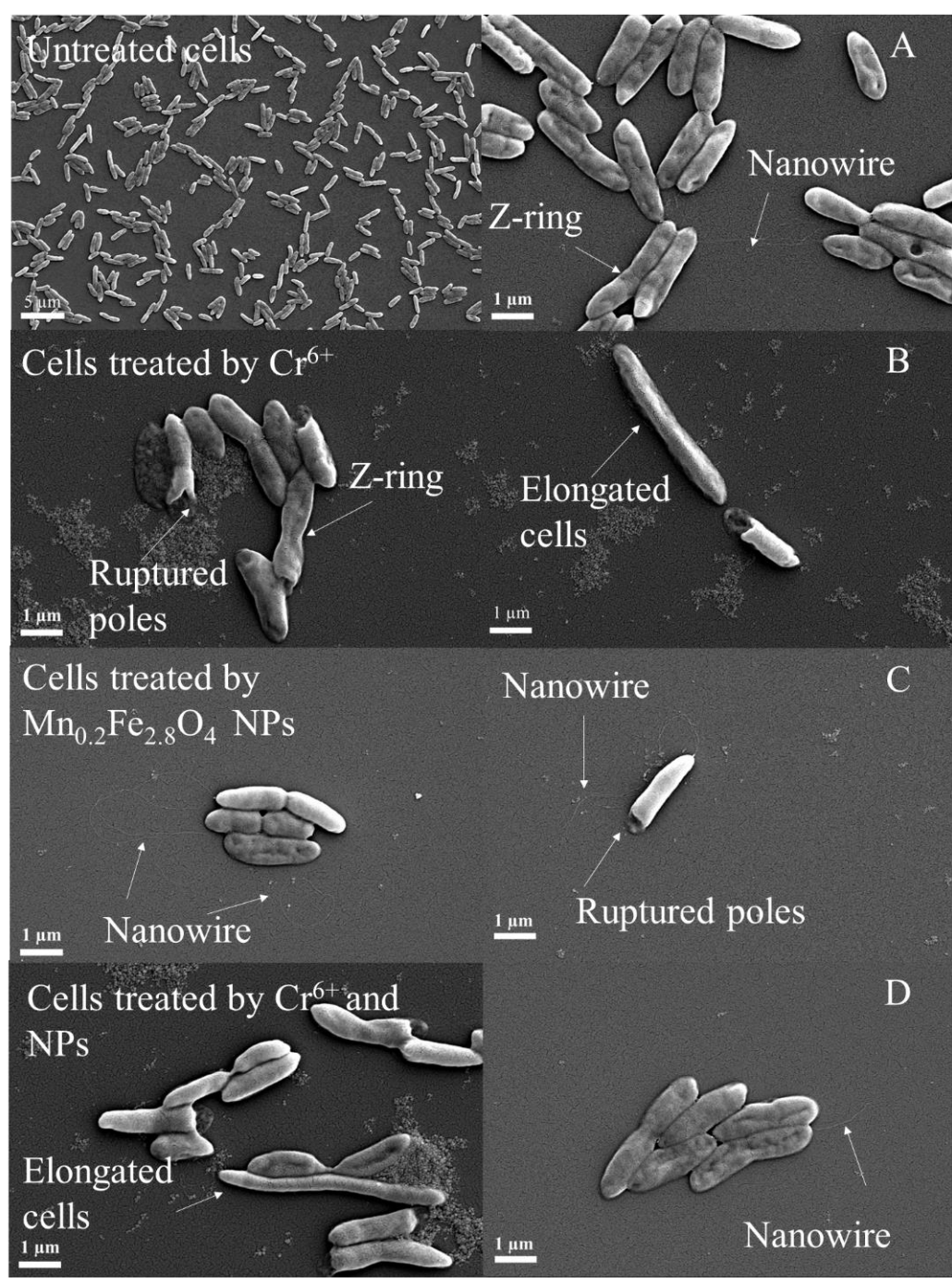
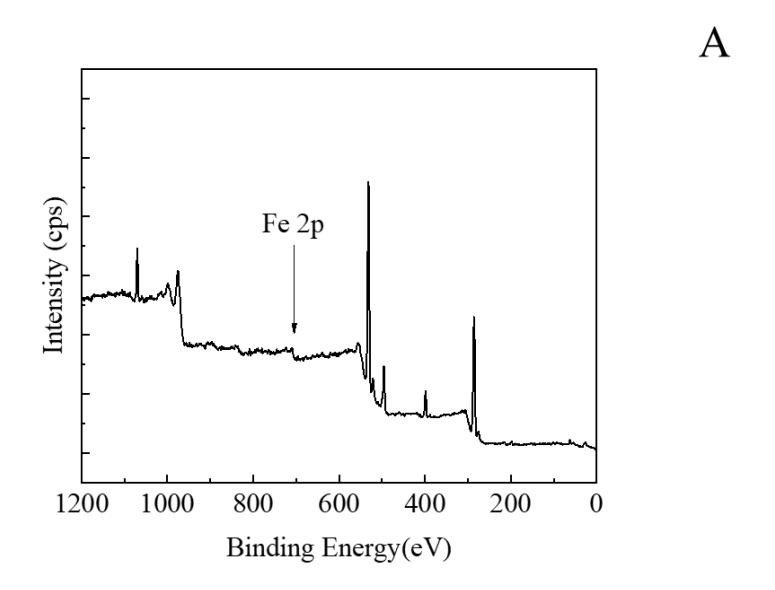


Figure 35: SEM micrographs of (A) untreated S. oneidensis MR-1 cells (B & C) treated cells by Cr^{6+} alone & $Mn_{0.2}^{2+}Fe_{2.8}^{3+}O_4$ NPs alone; respectively (D) treated cells by both Cr^{6+} and $Mn_{0.2}^{2+}Fe_{2.8}^{3+}O_4$ NPs.

4.3.5 Boosted respiration of Cr^{6+} via S. oneidensis MR-1 by the selected Mn_xFe_{3-} xO_4 NPs

A. Possible reduction of $Mn_{0.2}^{2+}Fe_{2.8}^{3+}O_4$ NPs by S. oneidensis MR-1



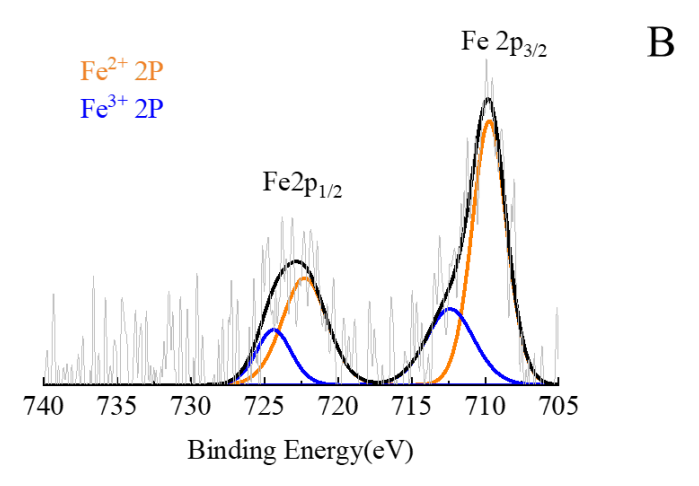


Figure 36: After being incubated with S. oneidensis MR-1, (A) XPS spectra of $\text{Mn}_{0.2}^{2+} \text{Fe}_{2.8}^{3+} \text{O}_4 NPs \ (B) \ high-resolution \ XPS \ spectrum \ of Fe \ 2p.$

Incubation of $Mn_{0.2}^{2+}Fe_{2.8}^{3+}O_4NPs$ with *S. oneidensis* MR-1 caused a slight shifting of the position of Binding Energy (BE) for Fe 2p to lower BE (709.9 eV), and the peak became narrower (FWHM = 1.8), as shown in *Figure 36 A* and *B*. After the interaction of Cr^{6+} and *S. oneidensis* MR-1 with $Mn_{0.2}^{2+}Fe_{2.8}^{3+}O_4NPs$, Mn in this sample could not be detected, which could be due to heterogeneity in the sample, its low concentration and possible uptake of NPs by *S. oneidensis* MR-1.

B. Reduction of Cr^{6+} by S. oneidensis MR-1

In *Figure 37 A*, XPS results showed the presence of peaks related to both Cr^{6+} and Cr^{3+} after exposing *S. oneidensis* MR-1 to Cr^{6+} . Peaks of Cr 2p XPS at BE 576.7 and 585.9 eV were associated with Cr^{3+} . The peaks at 579.2 and 588.6 eV were assigned to Cr^{6+} , as presented in *Figure 38 A & B*. The ratio between extracellular $[Cr^{3+}]$ and $[Cr^{6+}]$ was equal to 1.17. The presence of Cr^{3+} was attributed to using Cr^{6+} as a terminal electron acceptor during the respiration process of *S. oneidensis* MR-1.^{79,240}

C. Enhanced microbial reduction of Cr^{6+} by the selected $Mn_xFe_{3-x}O_4$ NPs

Figure 37 B revealed the occurrence of XPS peaks related to both Cr^{6+} and Cr^{3+} after incubation with S. oneidensis MR-1 in the presence of $Mn_{0.2}^{2+}Fe_{2.8}^{3+}O_4$ NPs. Peaks of Cr 2p XPS observed at BE 576.7 and 585 eV are related to Cr^{3+} . Cr^{6+} oxides are represented by one peak at 579.18 eV²⁰⁶, as illustrated in Figure 38 B. Similar results were reported due to respiring Cr^{6+} as a terminal electron acceptor by S. oneidensis MR-

 $1.^{79,240}$ The ratio between extracellular [Cr³⁺] and [Cr⁶⁺] was equal to 3.5. The production of biogenic Fe²⁺ via the reduction of Fe³⁺ hydroxides by bacteria can reduce Cr⁶⁺.^{69,60}

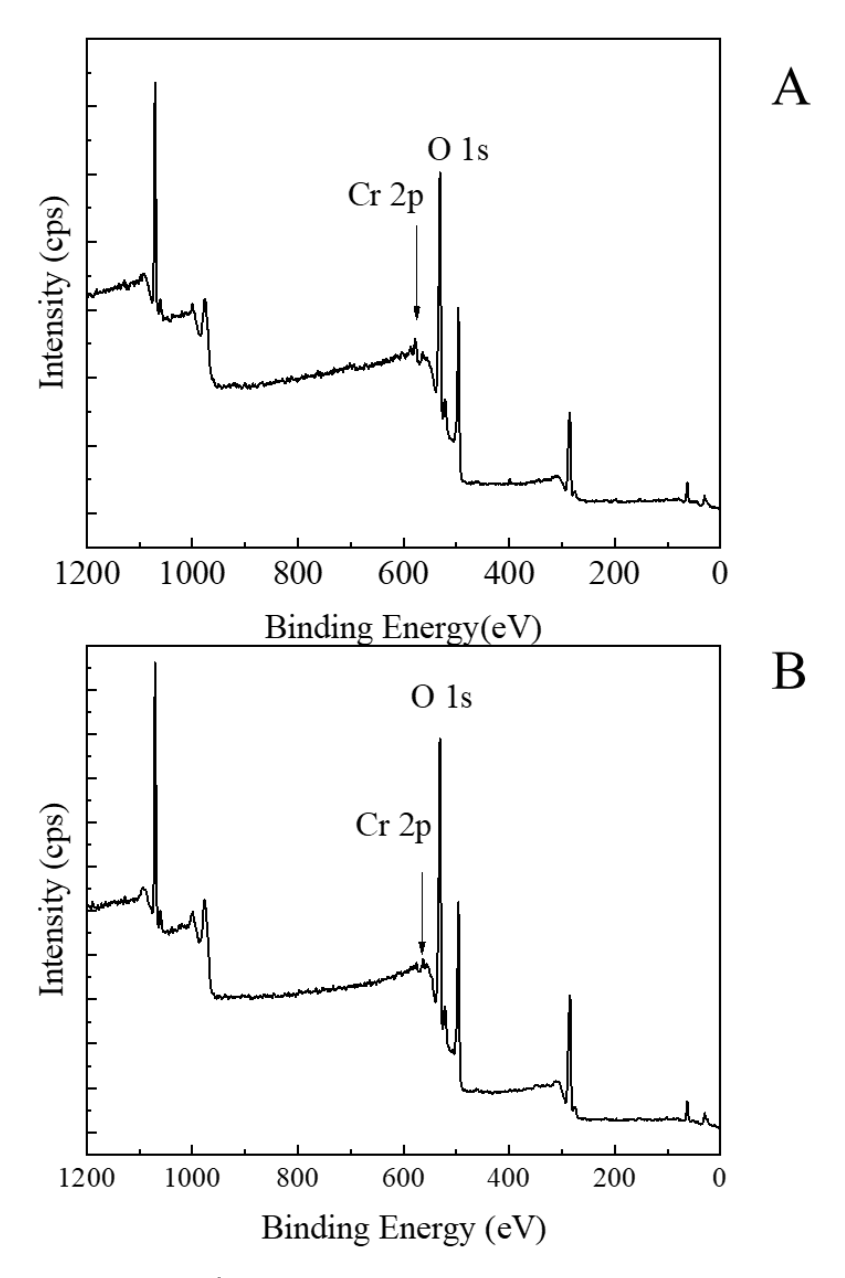
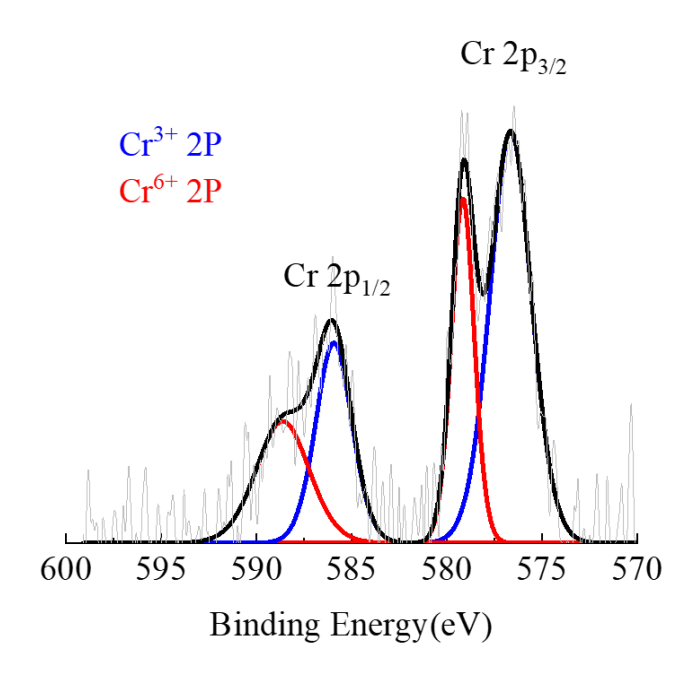


Figure 37: XPS spectra of Cr^{6+} after being (A) incubated with S. oneidensis MR-1 alone and (B) treated by both S. oneidensis MR-1 and $Mn_{0.2}^{2+}Fe_{2.8}^{3+}O_4$ NPs.





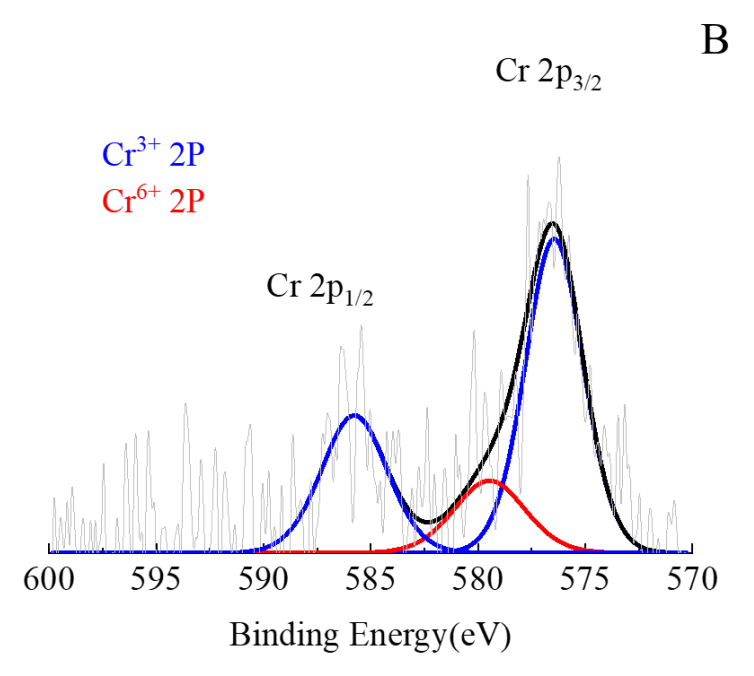


Figure 38: High-resolution XPS spectra of Cr 2p after incubating Cr^{6+} with (A) S. oneidensis MR-1 alone, (B) S. oneidensis MR-1 in the presence of $Mn_{0.2}^{2+}Fe_{2.8}^{3+}O_4NPs$.

From the present work, the presence of both *S. oneidensis* MR-1 and $Mn_{0.2}^{2+}Fe_{2.8}^{3+}O_4$ NPs improved the Cr^{6+} removal 1.4 times more than using NPs alone, as shown in Chapter 3. The presence of both microbes and Fe^0 can remove 85.6% of Cr^{6+} , 142 which matched our results of using both *S. oneidensis* MR-1 and $Mn_{0.2}^{2+}Fe_{2.8}^{3+}O_4$ NPs together, but our results showed a faster response (14 day 142 vs 18 h). The integrated use of microbes and Fe^0 increased the elimination of Cr^{6+} by 2.9 times compared to the sole use of $Fe^{0.142}$ Fe^0 NPs together with *S. oneidensis* MR-1 can detoxify Cr^{6+} into Cr^{3+} in the form of Cr^{3+} oxide, 91,141,142 Cr^{3+} hydroxides, 91,141,142 chromite ($FeCr_2O_4$) 91 , Cr-Fe hydroxides 142 and Cr^{3+} complex. 141

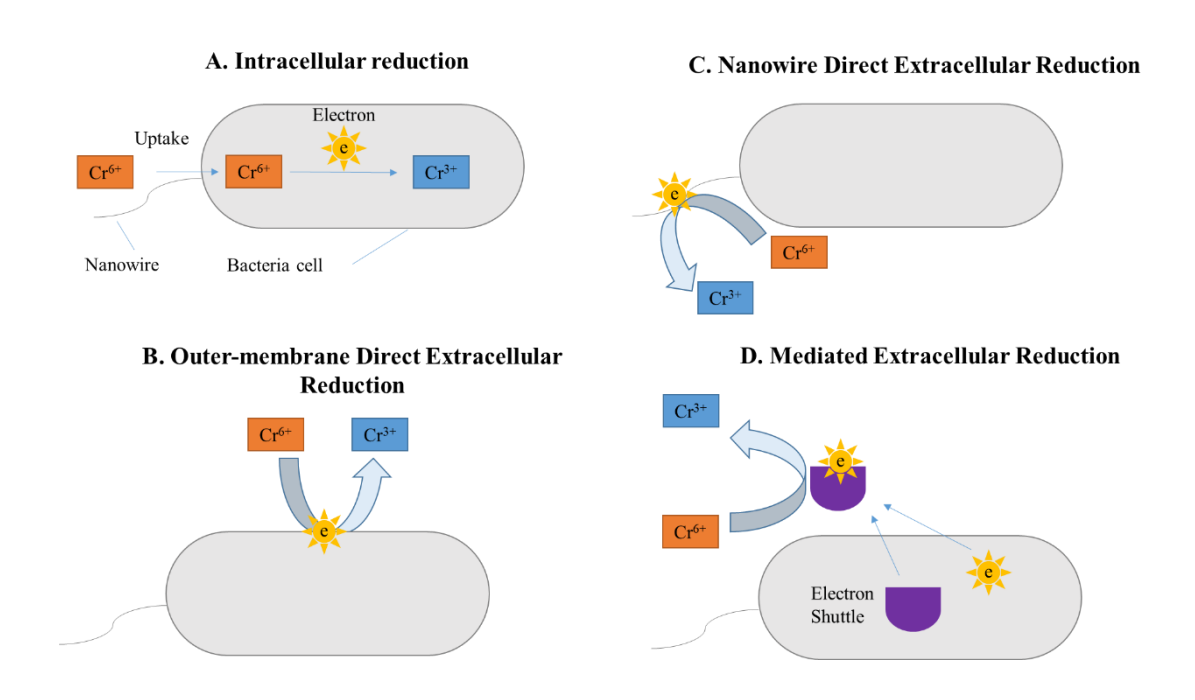


Figure 39: The possible mechanisms of Cr^{6+} reduction by S. oneidensis MR-1 to Cr^{3+} .

Redrawn from. ¹⁵⁶

Overall, *S. oneidensis* MR-1, as metal-reducing bacteria, can reduce Cr⁶⁺ to Cr³⁺, as was confirmed by our XPS results in *Figure 38* and supported by other kinds of literature.^{79,240} *S. oneidensis* MR-1 used multiple pathways for metal respiration, and *Figure 39* summarised some possible mechanisms for the microbial detoxification of Cr⁶⁺. *S. oneidensis* MR-1 can uptake Cr⁶⁺ to be reduced inside the cell to Cr³⁺,⁶⁷ as shown in *Figure 39 A*. However, our results did not confirm the intracellular reduction of Cr⁶⁺ due to the depth limitation (7-10 nm) of XPS.^{206,209} The extracellular reduction of Cr⁶⁺ can occur via direct contact of Cr⁶⁺ to the mtr-CAB complex on the cell surface (*Figure 39 B*) and nanowires (*Figure 39 C*). Also, *S. oneidensis* MR-1 can produce electron shuttles to promote MET between the cell and Cr⁶⁺ (*Figure 39 D*).

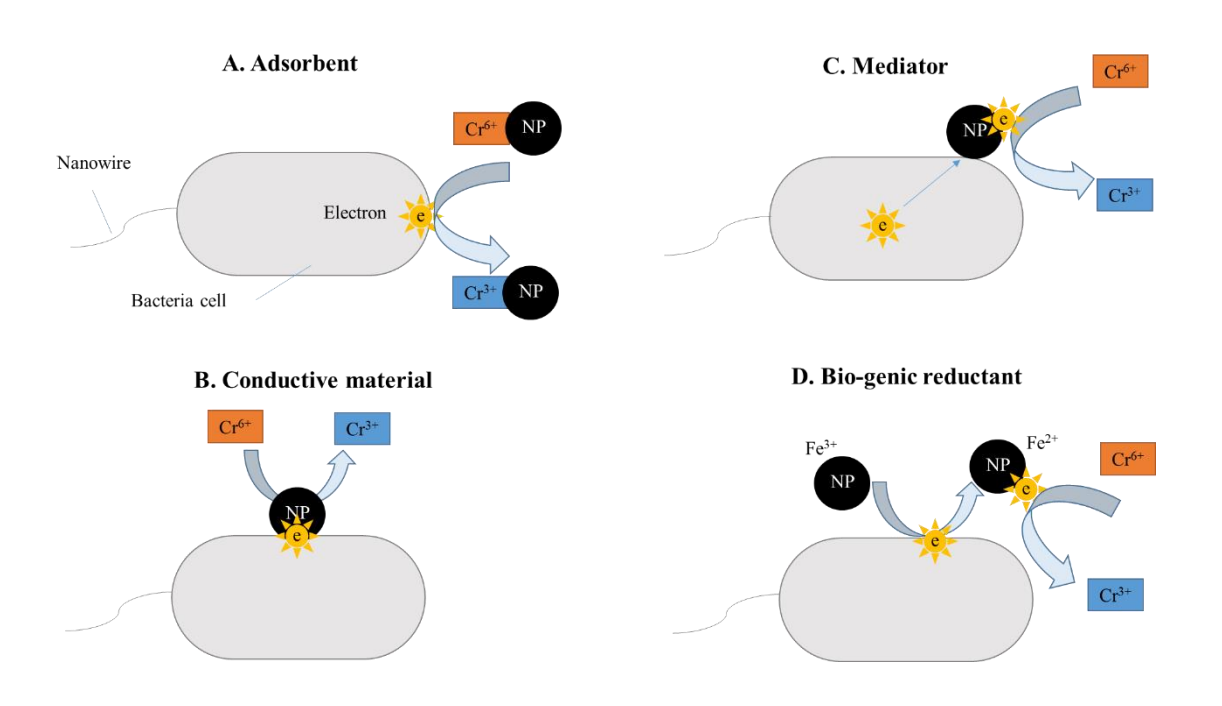


Figure 40: Possible synergistic scenarios of S. oneidensis MR-1 and $Mn_{0.2}^{2+}Fe_{2.8}^{3+}O_4$ NPs on Cr^{6+} reduction. Redrawn from. ¹⁵⁶

Some possible scenarios could explain how NPs enhanced the bio-reduction of *S. oneidensis* MR-1 from Cr^{6+} to Cr^{3+} ; however, the exact mechanism is not covered. NPs can act as a bridge between the bacterial cell and Cr^{6+} by adsorption to promote electron transfer, sa shown in *Figure 40 A.* $Mn_{0.2}^{2+}Fe_{2.8}^{3+}O_4$ NPs can adsorb Cr^{6+} via ion exchange from the aqueous solution solution and covalent bonding of Cr^{6+} on the surface of $Mn_{0.2}^{2+}Fe_{2.8}^{3+}O_4$ NPs 146 (*Figure 26-29*). Cr^{6+} adsorption on the surface of NPs and its reduction to Cr^{3+} decrease its accessibility and toxicity to the cells. The limited availability of adsorbed Cr^{6+} improved the efficiency of microbial respiration, sa was approved by our results in *Figure 34*. Since $MnFe_2O_4$ NPs have electro-chemical properties, so metal oxides can link *S. oneidensis* with Cr^{6+} to promote DET^{67} (*Figure 40 B*) and act as an electron mediator from the cell to Cr^{6+} as a terminal electron acceptor (*Figure 40 C*). In $MnFe_2O_4$, the existence of Mn and Fe in different oxidation states facilitates the redox processes on the nanoparticle surface. Si Finally, *S. oneidensis* MR-1 can reduce Fe^{3+} of $Mn_{0.2}^{2+}Fe_{2.8}^{3+}O_4$ NPs to Fe^{2+} (bio-genic Fe^{2+}), which can further reduce Cr^{6+} to Cr^{3+} , so shown in *Figure 40 D*.

4.4 Conclusion

 $Mn_{0.2}^{2+}Fe_{2.8}^{3+}O_4NPs$ (prepared from Mn^{2+} precursor at synthesis temperature at 250 °C for 6 h and showed the highest Cr^{6+} adsorption capacity (16.8 \pm 1.6 mg/g)) lead to 3.3 times improvement in the recovery of *S. oneidensis* MR-1 from the lethal effect of Cr^{6+} . Combining both *S. oneidensis* MR-1 and $Mn_{0.2}^{2+}Fe_{2.8}^{3+}O_4NPs$ improved the total removal of Cr^{6+} by 2.66 times using bacteria alone (based on colourimetric analysis). Integrating both *S. oneidensis* MR-1 and $Mn_{0.2}^{2+}Fe_{2.8}^{3+}O_4NPs$ boosted the detoxification of

the removed Cr^{6+} by 2.1 times by using *S. oneidensis* MR-1 alone and by 1.4 times of $Mn_{0.2}^{2+}Fe_{2.8}^{3+}O_4NPs$. Our results will open up new revenue for research using nanomaterials for boosting the bio-reduction of Cr^{6+} using bacteria.

Chapter 5. Conclusion and Future Outlook

Eliminating the carcinogenic hexavalent chromium (Cr^{6+}) from wastewater is crucial for health and environmental considerations. Combining adsorption and bioreduction is a promising treatment method for Cr^{6+} removal.

5.1 Summary

Enhancing the bio-detoxification of Cr^{6+} by *Shewanella oneidensis* bacteria to a less toxic trivalent form (Cr^{3+}) using manganese ferrite nanostructures $(Mn_xFe_{3-x}O_4\ NS)$ as adsorbents is the aim of the present PhD. This target was achieved by addressing gaps in the literature, which were:

- The impact of Mn doping level and the oxidation state of Mn precursor $(Mn^{2+} vs Mn^{3+})$ on the adsorption capacity (Qe) of $Mn_xFe_{3-x}O_4$ NS to Cr^{6+} .
- The effect of the selected $Mn_xFe_{3-x}O_4$ NS on the bio-detoxification efficiency of Cr^{6+} by *S. oneidensis* MR-1.

Our results revealed that using the polyol solvothermal method produced spherical Mn_xFe_{3-x}O₄ nanoparticles (NPs) with diameters ranging from 5 to 8 nm. Using Mn³⁺ as a source for Mn resulted in an insignificant decrease in the diameter and crystal size of NPs, which were synthesised at 250 °C. The synthesis temperature directed the shape of Mn_xFe_{3-x}O₄ NS from nanoflowers (NFs) at 200 °C to spherical NPs at 250 °C when using Mn³⁺ precursor. Under the outlined settings, our technology has the potential

for up-scaling because of the reproducibility, ease, and suitability of preparing Mn_xFe_{3-} $_xO_4$ NPs for various applications.

The non-stoichiometric structures of $Mn_xFe_{3-x}O_4$ NPs probably induced the slight shift in XRD patterns from the theoretical positions toward higher values. XRD results showed that a mixture of phases was formed when preparing NPs with [Mn(acac)_{2 or 3}] / [Fe(acac)₃] over 0.6.

Using Mn²⁺ precursor for preparing Mn_xFe_{3-x}O₄ NPs showed a lower Mn doping level than Mn³⁺. A positive relationship between the Mn doping level and [Mn(acac)_{2 or} $_3$] / [Fe(acac)₃] was observed, significantly influencing the chemical composition of Mn_xFe_{3-x}O₄ NPs prepared from the same Mn precursor. Mn substitution in magnetite crystal was limited in both Mn-used precursors (Mn_X^{2+} Fe_{3-x}O₄, $0.1 \le x \le 0.4 \pm 0.05$ and Mn_X^{3+} Fe_{3-x}O₄ $0.1 \le x \le 0.5 \pm 0.1$).

 $Mn_xFe_{3-x}O_4$ NPs prepared from Mn^{2+} precursor showed a higher Cr^{6+} adsorption capacity than those designed from Mn^{3+} source. $Mn_{0.2}^{2+}Fe_{2.8}^{3+}O_4$ NPs prepared from divalent manganese precursor at a synthesis temperature of 250 °C for 6 demonstrated the highest Cr^{6+} adsorption capacity (16.8 \pm 1.6 mg/g). Approximately 61% of the adsorbed Cr^{6+} by $Mn_{0.2}^{2+}Fe_{2.8}^{3+}O_4$ NPs were detoxified into Cr^{3+} , as shown in Chapter 3. As presented in Chapter 4, $Mn_{0.2}^{2+}Fe_{2.8}^{3+}O_4$ NPs lead to a 3.3 times improvement in the recovery of S. oneidensis MR-1 from the lethal effect of Cr^{6+} . The total removal of Cr^{6+} by combining both S. oneidensis MR-1 and $Mn_{0.2}^{2+}Fe_{2.8}^{3+}O_4$ NPs were enhanced 2.66 times by using bacteria alone (based on colourimetric analysis). Integrating both S. oneidensis MR-1 and

 $Mn_{0.2}^{2+}Fe_{2.8}^{3+}O_4NPs$ boosted the detoxification of the removed Cr^{6+} by 2.06 times by using *S. oneidensis* MR-1 alone and by 1.37 times by using $Mn_{0.2}^{2+}Fe_{2.8}^{3+}O_4NPs$.

5.2 Conclusion

The original contribution to the knowledge of the present project is that: $Mn_{0.2}^{2+}Fe_{2.8}^{3+}O_4NPs$ showed the highest Qe for Cr^{6+} among the tested $Mn_xFe_{3-x}O_4NS$ and enhanced the bio-detoxification of Cr^{6+} by *S. oneidensis* MR-1. Using nanomaterials to enhance microbial viability during the bio-remediation process helps resolve the lack of inexpensive and effective technologies for wastewater treatment. This will open up new revenue for research applying NS to boost the bio-reduction of Cr^{6+} using bacteria.

5.3 Future work

The findings of this PhD project revealed that $Mn_{0.2}^{2+}Fe_{2.8}^{3+}O_4NPs$ improved the recovery of *S. oneidensis* MR-1 from the sub-lethal dose of Cr^{6+} by 3.3 times and enhanced Cr^{6+} removal and reduction by 2.66 and 2.06 times, respectively, using *S. oneidensis* MR-1. Therefore, further studies should be conducted as described as follows.

Exploring the impact of interfering materials on the adsorption of Cr⁶⁺ by
 NPs

Our findings for Cr^{6+} elimination and bio-reduction were obtained from spiked water with Cr^{6+} . Various pollutants in real-world samples can impede the binding of Cr^{6+} to the adsorbent, such as sulfate, phosphate and carbonate. ^{154,241} In addition, the

unspecific bio-reduction of terminal electron acceptors by *S. oneidensis* MR-1 can hinder the detoxification efficiency of Cr^{6+} .²⁴² The environmental samples have microbial communities, which generate competition among organisms and suppress microbial growth.²⁴³ Such competitiveness limits the removal and reduction efficiency of nanoadsorbents and bacteria for Cr^{6+} .⁵⁴ So, exploring the impact of such interfering materials on the adsorption capacity of $Mn_{0.2}^{2+}Fe_{2.8}^{3+}O_4$ NPs and bio-reduction efficiency of *S. oneidensis* MR-1 to Cr^{6+} will be a step toward mimicking real-world environments.

Optimising the process of integrated adsorption and bio-reduction for Cr⁶⁺

In Chapter 3 and Chapter 4, Cr^{6+} removal and bio-reduction were investigated under controlled conditions, such as room temperature and neutral pH. The presented outputs of Cr^{6+} reduction and bio-reduction were acquired at a lab scale. Using $Mn_{0.2}^{2+}Fe_{2.8}^{3+}O_4$ NPs improved the viability of bacteria and the bio-reduction efficiency, as shown in our results.

Many physical parameters affect the adsorption and bio-remediation of Cr⁶⁺. Electrostatic attraction between Cr⁶⁺ and adsorbents showed high removal efficiencies at low pH values. The bio-reduction of Cr⁶⁺ was reported to be maximised at pH 8. The pH of tannery effluents as industrial wastewater also ranged from 3.8 to 13.67. Studying the impact of temperature on the adsorption capacities, and bio-reduction tested the reaction's spontaneity. The temperature of tannery effluents varied between 11 °C to 50 °C, 244, 245 depending on the manufacturing stages. The kinetics of Cr⁶⁺ removal is always studied for all adsorbents to infer the process's reaction mechanism. So, exploring the impact of pH, temperature, kinetics, and other factors on the adsorption and

bio-reduction of Cr^{6+} will be involved to maximise the effectiveness of Cr^{6+} removal, mimic the real-world samples and describe the mechanism of Cr^{6+} elimination.

• Scaling up Cr⁶⁺ removal by nano-adsorbents

The potential of applying the adsorption process of Cr⁶⁺ using Mn_{0.2}²⁺Fe_{2.8}²⁺O₄ NPs for an industrial scale should be studied to show the correlation between the results of lab-scale and mass-scale.^{247–250} The adsorption experiments will proceed via laboratory fixed-bed columns and a larger scale column as a typical system design for scaling up tests.^{247–250} The scaling-up adsorption experiments depend on the mass transfer phenomena and hydraulic performance. Several factors related to the fixed-bed columns will be implemented, including the flow rate, pollutant concentration, and others. Conducting studies in a larger scale column should describe how the scale can manage the adsorption capacity, saturation time, and others.^{247–250}

 Investigating the impact of modifying the surface of Mn_xFe_{3-x}O₄ NS by different functional groups on Cr⁶⁺ adsorption and bio-reduction

Using tri-sodium citrate as a functional group on the surface of $Mn_xFe_{3-x}O_4$ demonstrated a stable dispersion of the nanomaterials in a water medium, as was presented in Chapter 2. Nevertheless, citrate granted the nano-adsorbents a negatively charged surface which could cause repulsive force with chromate. So, in future studies, positively charged ligands can be used as a functional group on the NPs to induce attractiveness between the adsorbents and Cr^{6+} .

• Studying the effect of co-dopants on the adsorption capacity and reduction efficiency of $Mn_xFe_{3-x}O_4$ NS to Cr^{6+} to avoid the extra cost of microbial treatment of Cr^{6+}

 $Mn_{0.2}^{2+}Fe_{2.8}^{3+}O_4NPs$ enhanced Cr^{6+} bio-removal and bio-reduction by 2.66 and 2.06 times of using bacteria alone, as shown in Chapters 3 and 4. While $Mn_{0.2}^{2+}Fe_{2.8}^{3+}O_4NPs$ alone can act as adsorbing and reducing agents for Cr^{6+} . So, studying the impact of dopants on the NPs to induce the safe removal of Cr^{6+} is promising to avoid using bacteria that will minimise the hydrocarbon-containing waste and save the added cost of biological treatment.

Probing the interaction between bacteria and Cr⁶⁺

In the current project, X-ray photoelectron spectroscopy (XPS) was used to assay the reduction of Cr⁶⁺ to Cr³⁺, as shown in Chapter 3 and Chapter 4. XPS is a surface analysis technique used for compositional and chemical state analysis.^{206,209} The detection limits for elements by XPS are in the parts per thousand range, but it probes the sample's surface to a depth of 7-10 nm.^{206,209} At this depth, the possible absorbed Cr inside the bacterial cells was not considered. So, combining various microscopic and spectroscopic techniques to determine the cellular metal content and the metal distribution within cells is fruitful in better understanding the process of Cr⁶⁺ bio-reduction and the ways to improve its efficiency.

TEM can reveal the impact of both Cr^{6+} and $Mn_{0.2}^{2+}Fe_{2.8}^{3+}O_4$ NPs on the ultrastructure of cells and the localisation of metals inside cells.²⁵¹ Energy-dispersive X-

ray spectroscopy can define the elemental composition of metals on the surface of bacterial cells and inside the cells.⁷⁸ Electron Paramagnetic Resonance spectroscopy can probe the C^{6+} reduction mechanism by determining the possible presence of free radicals such as pentavalent chromium (Cr^{5+}) .⁷⁸

• Exploring new metal-reducing and metal-tolerating bacterial species

Our findings revealed the ability of *S. oneidensis* MR-1 to bio-sorb and bio-reduce Cr^{6+} , where the initial concentration of Cr^{6+} was 50 mg/L, as presented in Chapter 4. However, the concentration of Cr^{6+} in industrial effluents is 788 ± 3.5 mg/L.²⁷ So, exploring other metal-reducing bacteria that can tolerate such high concentrations of Cr^{6+} will be fruitful in producing minimal Cr-containing sludge.

 Applying microbial fuel cells (MFCs) for heavy metal removal and power production

An output of the present project is that $Mn_{0.2}^{2+}Fe_{2.8}^{3+}O_4$ NPs contain the lowest Mn doping level and have the best Qe for Cr^{6+} adsorption capacity among the tested $Mn_x^{2+ \text{ or } 3+}Fe_{3-x}^{3+}O_4$ NS. $Mn_xFe_{3-x}O_4$ NS has the highest Qe for Cr^{6+} among many tested ferrites, revealing bio-compatibility to human cell lines. $Mn_xFe_{3-x}O_4$ NS as electron mediators and electrodes are endorsed for wastewater treatment using bio-electrochemical systems such as MFCs. $Mn_xFe_{3-x}O_4$ NS.

As stated in Chapter 1, MFCs are bio-electrochemical systems which can be used for electricity production and waste treatment. The critical advantage of MFCs compared

to conventional fuel cells is the mild operation conditions. 130,253 The pollutants' lethal effect still limits applying MFCs for Cr^{6+} detoxification. 132,253 MnFe₂O₄ NPs can improve the accumulation of *S. putrefaciens* on the anode surface 151,152 and the power generation of MFCs, 152 as reviewed in Chapter 1. Hence, studying the effect of the chemical structural features of the Mn_xFe_{3-x}O₄ NPs on the electrochemical activity of electrodes of MFCs can enhance the productivity and bio-reduction of Cr^{6+} .

• Bio-genesis of chromium ferrite nanoparticles for Cr⁶⁺ recovery

Recycling heavy metals from wastewater as Cr-doped Fe₃O₄ NPs has gathered research interest.^{254–256} Biological synthesis of nanoparticles using plants, fungi, algae, and bacteria has been reported in the literature.^{257,258} *Shewanella* can biosynthesise Fe₃O₄ NPs doped by transition metals such as Cr, Mn, Co, Ni and Zn.²⁵⁹ So, optimising the doping level of Cr in the bio-genic magnetic Cr-doped Fe₃O₄ NPs will offer an opportunity to separate such heavy metals using external magnets.

• Expanding the use of Mn_xFe_{3-x}O₄ NS for medical applications

The present PhD project provides a robust method for synthesising $Mn_xFe_{3-x}O_4$ NS. From the literature, $Mn_xFe_{3-x}O_4$ NS is a magnetic nanomaterial which has been extensively used in various applications. Under the influence of an AC magnetic, clustered magnetic nanostructures generate superior heating characteristics than the smaller single crystals. Such heating energy generation is the basis of magnetic hyperthermia for cancer treatment. So, studying the hyperthermia properties of our $Mn_xFe_{3-x}O_4$ NFs will maximise the benefits of such materials for medical applications.

 Expanding the use of Mn_xFe_{3-x}O₄ NS as bio-ferrofluids in medical and biotechnology applications

Ferrofluids are ultra-stable colloidal suspensions of magnetic NPs, which own both fluid and magnetic properties.²⁶¹ Ferrofluids are applicable in many fields, such as bio-sensors, medical imaging techniques, hyperthermia, drug delivery, anti-microbial activities, heat transfer, and energy harvesting. The core diameter of NPs in ideal ferrofluids was 5–10 nm, and conventional (real) ferrofluids were 5–15 nm.²⁶¹ The core diameter of Mn_xFe_{3-x}O₄ NPs in the present project was 5 to 8, which is in the reported ideal range of ferrofluids. Mn_xFe_{3-x}O₄ NS has magnetic behaviour,^{159,161} but to consider Mn_xFe_{3-x}O₄ NPs of the present work as bio-ferrofluid, the magnetic properties and the fluid stability of NPs should be tested. The magnetic properties of a ferrofluid can be determined by tools such as Mössbauer Spectroscopy and magnetometry. From our results, the dispersed citrate-coated NPs in water have a zeta potential ranging from -25 to -35 eV, forming a stable suspension in water. However, different physiological media should characterise colloidal stability and particle aggregation.²⁶¹

References

- (1) Sikander, M.; Kumar, L.; Naqvi, S. A.; Arshad, M.; Jabeen, S. Sustainable Practices for Reduction of Environmental Footprint in Tanneries of Pakistan. *Case Stud. Chem. Environ. Eng.* **2021**, *4*, 100161–100166. https://doi.org/10.1016/j.cscee.2021.100161.
- (2) Monga, A.; Fulke, A. B.; Dasgupta, D. Recent Developments in Essentiality of Trivalent Chromium and Toxicity of Hexavalent Chromium: Implications on Human Health and Remediation Strategies. J. Hazard. Mater. Adv. 2022, 7, 100113–100130.
- (3) Pushkar, B.; Sevak, P.; Parab, S.; Nilkanth, N. Chromium Pollution and Its Bioremediation Mechanisms in Bacteria: A Review. *J. Environ. Manage.* **2021**, 287 (February), 112279–112298. https://doi.org/10.1016/j.jenvman.2021.112279.
- (4) Zhang, Y.; Zheng, P.; Su, Z.; Hu, G.; Jia, G. Perspectives of Genetic Damage and Epigenetic Alterations by Hexavalent Chromium: Time Evolution Based on a Bibliometric Analysis. *Chem. Res. Toxicol.* **2021**, *34* (3), 684–694. https://doi.org/10.1021/acs.chemrestox.0c00415.
- International Agency for Research on Cancer. List of Classifications—IARC
 Monographs on the Identification of Carcinogenic Hazards to Humans; 2020; Vol.
 1.

- (6) World Health Organization (WHO). The Public Health Impact of Chemicals: Knowns and Unknowns; 2016.
- (7) Zhang, K.; Li, N.; Liao, P.; Jin, Y.; Li, Q.; Gan, M.; Chen, Y.; He, P.; Chen, F.; Peng, M.; Zhu, J. Conductive Property of Secondary Minerals Triggered Cr(VI) Bioreduction by Dissimilatory Iron Reducing Bacteria. *Environ. Pollut.* 2021, 286, 117227–117236. https://doi.org/10.1016/j.envpol.2021.117227.
- (8) Liu, L.; Liu, G.; Zhou, J.; Jin, R. Interaction between Hexavalent Chromium and Biologically Formed Iron Mineral-Biochar Composites: Kinetics, Products and Mechanisms. J. Hazard. Mater. 2021, 405 (October 2020), 124246–124257. https://doi.org/10.1016/j.jhazmat.2020.124246.
- (9) Liu, X.; Chu, G.; Du, Y.; Li, J.; Si, Y. The Role of Electron Shuttle Enhances Fe(III)-Mediated Reduction of Cr(VI) by *Shewanella Oneidensis* MR-1. *World J. Microbiol. Biotechnol.* 2019, 35 (4), 1–8. https://doi.org/10.1007/s11274-019-2634-9.
- (10) Zhang, Q.; Amor, K.; Galer, S. J. G.; Thompson, I.; Porcelli, D. Using Stable Isotope Fractionation Factors to Identify Cr(VI) Reduction Pathways: Metal-Mineral-Microbe Interactions. Water Res. 2019, 151, 98–109. https://doi.org/10.1016/j.watres.2018.11.088.
- (11) Ghorbanzadeh, N.; Lakzian, A.; Halajnia, A.; Kumar, M. S.; Jeon, B. H. Removal of Chromium [Cr(VI)] from Contaminated Solutions by Using Biogenic Ferrous Iron in Bioreduced Minerals. *Geosystem Engineering*. Taylor & Francis 2014, pp

- 95–103. https://doi.org/10.1080/12269328.2014.928239.
- (12) Survey, U. S. G. *Mineral Commodity Summaries 2022*; Reston, VA, 2022. https://doi.org/10.3133/mcs2022.
- (13) Vaiopoulou, E.; Gikas, P. Regulations for Chromium Emissions to the Aquatic Environment in Europe and Elsewhere. *Chemosphere* **2020**, *254*, 126876. https://doi.org/10.1016/j.chemosphere.2020.126876.
- (14) Novotnik, B.; Ščančar, J.; Milačič, R.; Filipič, M.; Žegura, B. Cytotoxic and Genotoxic Potential of Cr(VI), Cr(III)-Nitrate and Cr(III)-EDTA Complex in Human Hepatoma (HepG2) Cells. *Chemosphere* **2016**, *154*, 124–131. https://doi.org/10.1016/j.chemosphere.2016.03.118.
- (15) Desmarias, T. L.; Costa, M. Toxicology Mechanisms of Chromium-Induced Toxicity. *Curr. Opin. Toxicol.* **2019**, *14*, 1–7. https://doi.org/10.1016/j.cotox.2019.05.003.
- (16) Wise, J. P.; Young, J. L.; Cai, J.; Cai, L. Current Understanding of Hexavalent Chromium [Cr(VI)] Neurotoxicity and New Perspectives. *Environ. Int.* **2022**, *158*, 106877–106894. https://doi.org/10.1016/j.envint.2021.106877.
- (17) International Agency for Research on Cancer. *Overall Evaluations of Carcinogenicity: An Updating of IARC Monographs Volumes 1 to 42*; International Agency for Research on Cancer: Lyon, France, 1987.

- (18) Vincent, J. B. Is the Pharmacological Mode of Action of Chromium(III) as a Second Messenger? *Biol. Trace Elem. Res.* **2015**, *166* (1), 7–12. https://doi.org/10.1007/s12011-015-0231-9.
- (19) Bagheri, S.; Gholamhosseini, A.; Banaee, M. Investigation of Different Nutritional Effects of Dietary Chromium in Fish: A Literature Review. *Biol. Trace Elem. Res.* **2022**, 1–9. https://doi.org/10.1007/s12011-022-03326-z.
- (20) Li, A.; Wang, Y.; Hao, J.; Wang, L.; Quan, L.; Duan, K.; Fakhar-e-Alam Kulyar, M.; Ullah, K.; Zhang, J.; Wu, Y.; Li, K. Long-Term Hexavalent Chromium Exposure Disturbs the Gut Microbial Homeostasis of Chickens. *Ecotoxicol. Environ. Saf.* 2022, 237 (April), 113532–113541. https://doi.org/10.1016/j.ecoenv.2022.113532.
- (21) Pal, H.; Priyanka, S. Chromium Toxicity and Tolerance in Plants. *Environ. Chem. Lett.* **2013**, *11* (3), 229–254. https://doi.org/10.1007/s10311-013-0407-5.
- (22) Moffat, I. V. Y.; Martinova, N.; Seidel, C.; Thompson, C. M. Hexavalent Chromium in Drinking Water. *Journal-American water Work. Assoc.* 2018, 110 (5), E22–E35. https://doi.org/10.1002/awwa.1044.
- (23) World Health Organization (WHO). Guidelines for Drinking-Water Quality; 2011.
- (24) Rada, E. C.; Schiavon, M.; Torretta, V. A Regulatory Strategy for the Emission Control of Hexavalent Chromium from Waste-to-Energy Plants. *J. Clean. Prod.*2021, 278, 123415–123423. https://doi.org/10.1016/j.jclepro.2020.123415.

- (25) Agency for Toxic Substances and Disease Registry. *Chromium Toxicity What Are*the Standards and Regulations for Chromium Exposure?; 2013.
- (26) Bearcock, J. M.; Smedley, P. L.; Fordyce, F. M.; Everett, P. A.; Ander, E. L. Controls on Surface Water Quality in the River Clyde Catchment, Scotland, UK, with Particular Reference to Chromium and Lead. *Earth Environ. Sci. Trans. R. Soc. Edinburgh* 2019, 108 (2–3), 249–267. https://doi.org/10.1017/S1755691018000397.
- (27) Fouda, A.; Hassan, S. E. D.; Saied, E.; Hamza, M. F. Photocatalytic Degradation of Real Textile and Tannery Effluent Using Biosynthesized Magnesium Oxide Nanoparticles (MgO-NPs), Heavy Metal Adsorption, Phytotoxicity, and Antimicrobial Activity. *J. Environ. Chem. Eng.* **2021**, *9* (4), 105346–105360. https://doi.org/10.1016/j.jece.2021.105346.
- (28) Bolaños-Benítez, V.; van Hullebusch, E. D.; Birck, J. L.; Garnier, J.; Lens, P. N. L.; Tharaud, M.; Quantin, C.; Sivry, Y. Chromium Mobility in Ultramafic Areas Affected by Mining Activities in Barro Alto Massif, Brazil: An Isotopic Study. *Chem. Geol.* 2021, 561 (December 2020), 120000–120011. https://doi.org/10.1016/j.chemgeo.2020.120000.
- (29) Islam, M. A.; Angove, M. J.; Morton, D. W. Recent Innovative Research on Chromium (VI) Adsorption Mechanism. *Environ. Nanotechnology, Monit. Manag.* 2019, 12 (August), 100267–100287. https://doi.org/10.1016/j.enmm.2019.100267.

- (30) Jones, A. S.; Marini, J.; Solo-Gabriele, H. M.; Robey, N. M.; Townsend, T. G. Arsenic, Copper, and Chromium from Treated Wood Products in the U.S. Disposal Sector. Waste Manag. 2019, 87, 731–740. https://doi.org/10.1016/j.wasman.2019.03.004.
- (31) Famielec, S. Chromium Concentrate Recovery from Solid Tannery Waste in a Thermal Process. *Materials* (*Basel*). **2020**, *13* (7), 1533–1545. https://doi.org/10.3390/ma13071533.
- (32) Wang, B.; Liu, B.; Gu, J.; Somers, M. A. J. Gaseous Carbonitriding of High Carbon Chromium Bearing Steel: Correlation between Composition, Microstructure and Stability. Surf. Coatings Technol. 2022, 438 (March), 128408–128422. https://doi.org/10.1016/j.surfcoat.2022.128408.
- (33) Tang, H.; Peng, Z.; Gu, F.; Yang, L.; Tian, W.; Zhong, Q.; Rao, M.; Li, G.; Jiang, T. Chromium-Promoted Preparation of Forsterite Refractory Materials from Ferronickel Slag by Microwave Sintering. *Ceram. Int.* 2021, 47 (8), 10809–10818. https://doi.org/10.1016/j.ceramint.2020.12.198.
- (34) Xing, J.; Pailthorpe, M. T. Chrome Dyeing of Cashmere with SCA-Cr as the Mordant. J. Soc. Dye. Colour. 2000, 116 (3), 91–93. https://doi.org/10.1111/j.1478-4408.2000.tb00026.x.
- (35) Wang, Z.; Bao, C.; Yan, K.; Song, Y.; Li, W. Study on Silica Coated Chrome Oxide Green Pigment and Its Performance. *J. Appl. Polym. Sci.* **2021**, *138* (17), 1–10. https://doi.org/10.1002/app.50281.

- (36) Sennaroglu, A.; Morova, Y. Divalent (Cr²⁺), Trivalent (Cr³⁺), and Tetravalent (Cr⁴⁺) Chromium Ion-Doped Tunable Solid-State Lasers Operating in the near and Mid-Infrared Spectral Regions. *Appl. Phys. B Lasers Opt.* **2022**, *128* (1), 1–25. https://doi.org/10.1007/s00340-021-07735-1.
- (37) Bratovcic, A.; Buksek, H.; Helix-Nielsen, C.; Petrinic, I. Concentrating Hexavalent Chromium Electroplating Wastewater for Recovery and Reuse by Forward Osmosis Using Underground Brine as Draw Solution. *Chem. Eng. J.* **2022**, *431* (P1), 133918–133927. https://doi.org/10.1016/j.cej.2021.133918.
- (38) Salman, S. A.; Elnazer, A. A. Assessment and Speciation of Chromium in Groundwater of South Sohag Governorate, Egypt. *Groundw. Sustain. Dev.* **2020**, *10* (December 2019), 100369–100375. https://doi.org/10.1016/j.gsd.2020.100369.
- (39) Kazakis, N.; Kantiranis, N.; Kalaitzidou, K.; Kaprara, M.; Mitrakas, M.; Frei, R.; Vargemezis, G.; Tsourlos, P.; Zouboulis, A.; Filippidis, A. Origin of Hexavalent Chromium in Groundwater: The Example of Sarigkiol Basin, Northern Greece. Sci. Total Environ. 2017, 593–594, 552–566. https://doi.org/10.1016/j.scitotenv.2017.03.128.
- (40) Fernandes, H. R.; Ferreira, J. M. F. Recycling of Chromium-Rich Leather Ashes in Porcelain Tiles Production. *J. Eur. Ceram. Soc.* **2007**, 27 (16), 4657–4663. https://doi.org/10.1016/j.jeurceramsoc.2007.03.037.
- (41) Li, W.; Ma, Z.; Huang, Q.; Jiang, X. Distribution and Leaching Characteristics of Heavy Metals in a Hazardous Waste Incinerator. *Fuel* **2018**, *233* (May), 427–441.

- https://doi.org/10.1016/j.fuel.2018.06.041.
- (42) Yu, S.; Zhang, H.; Lü, F.; Shao, L.; He, P. Flow Analysis of Major and Trace Elements in Residues from Large-Scale Sewage Sludge Incineration. *J. Environ. Sci. (China)* **2021**, *102*, 99–109. https://doi.org/10.1016/j.jes.2020.09.023.
- (43) Popiolski, A. S.; Demaman Oro, C. E.; Steffens, J.; Bizzi, C. A.; Santos, D.; Alessio, K. O.; Flores, É. M. M.; Duarte, F. A.; Dallago, R. M. Microwave-Assisted Extraction of Cr from Residual Tanned Leather: A Promising Alternative for Waste Treatment from Tannery Industry. *J. Environ. Chem. Eng.* 2022, 10 (1), 6–11. https://doi.org/10.1016/j.jece.2021.107081.
- (44) Pringle, T.; Barwood, M.; Rahimifard, S. The Challenges in Achieving a Circular Economy within Leather Recycling. *Procedia CIRP* **2016**, *48*, 544–549. https://doi.org/10.1016/j.procir.2016.04.112.
- (45) Rajesh, R.; Kanakadhurga, D.; Prabaharan, N. Electronic Waste: A Critical Assessment on the Unimaginable Growing Pollutant, Legislations and Environmental Impacts. *Environ. Challenges* **2022**, 7 (August 2021), 100507–100521. https://doi.org/10.1016/j.envc.2022.100507.
- (46) Roy, H.; Rahman, T. U.; Suhan, M. B. K.; Al-Mamun, M. R.; Haque, S.; Islam, M. S. A Comprehensive Review on Hazardous Aspects and Management Strategies of Electronic Waste: Bangladesh Perspectives. *Heliyon* 2022, 8 (7), e09802-e9814. https://doi.org/10.1016/j.heliyon.2022.e09802.

- (47) Hang, J. G.; Dong, J. J.; Feng, H.; Huang, J. Z.; Wang, Z.; Shen, B.; Nakayama, S. F.; Kido, T.; Jung, C.-R.; Ma, C.; Sun, X. L. Evaluating Postnatal Exposure to Six Heavy Metals in a Chinese E-Waste Recycling Area. *Chemosphere* 2022, 308 (P2), 136444–136449. https://doi.org/10.1016/j.chemosphere.2022.136444.
- (48) Elnazer, A. A.; Mostafa, A.; Salman, S. A.; Seleem, E. M.; Al-Gamal, A. G.-A. Temporal and Spatial Evaluation of the River Nile Water Quality between Qena and Sohag Cities, Egypt. *Bull. Natl. Res. Cent.* **2018**, *42* (1), 1–7. https://doi.org/10.1186/s42269-018-0005-6.
- (49) Kazakis, N.; Kantiranis, N.; Kalaitzidou, K.; Kaprara, E.; Mitrakas, M.; Frei, R.; Vargemezis, G.; Vogiatzis, D.; Zouboulis, A.; Filippidis, A. Environmentally Available Hexavalent Chromium in Soils and Sediments Impacted by Dispersed Fly Ash in Sarigkiol Basin (Northern Greece). *Environ. Pollut.* 2018, 235, 632–641. https://doi.org/10.1016/j.envpol.2017.12.117.
- (50) Awang, N. A.; Salleh, W. N. W.; Ismail, A. F.; Yusof, N.; Aziz, F.; Jaafar, J. Adsorption Behavior of Chromium(VI) onto Regenerated Cellulose Membrane. *Ind. Eng. Chem. Res.* 2019, 58 (2), 720–728.
 https://doi.org/10.1021/acs.iecr.8b02366.
- (51) Villalobos-lara, A. D.; Alvarez, F.; Gami, Z.; Navarro, R.; Peralta-hern, J. M. Electrocoagulation Treatment of Industrial Tannery Wastewater Employing a Modified Rotating Cylinder Electrode Reactor. *Chemosphere* 2021, 264, 128491–128499. https://doi.org/10.1016/j.chemosphere.2020.128491.

- (52) El-Dib, F. I.; Mohamed, D. E.; El-Shamy, O. A. A.; Mishrif, M. R. Study the Adsorption Properties of Magnetite Nanoparticles in the Presence of Different Synthesized Surfactants for Heavy Metal Ions Removal. *Egypt. J. Pet.* **2020**, 29 (1), 1–7. https://doi.org/10.1016/j.ejpe.2019.08.004.
- (53) Id, Z. Q.; Dong, W.; Chen, Y.; Dong, G.; Zhu, S.; Yu, Y.; Bian, D. Upcycling of Groundwater Treatment Sludge to Magnetic Fe/Mn-Bearing Nanorod for Chromate Adsorption from Wastewater Treatment. *PLoS One* 2020, *15* (6), 1–17. https://doi.org/10.1371/journal.pone.0234136.
- (54) Pakade, V. E.; Tavengwa, T.; Madikizela, L. M. Recent Advances in Hexavalent Chromium Removal from Aqueous Solutions by Adsorptive Methods. *RSC Adv.*2019, 9 (45), 26142–26164. https://doi.org/10.1039/c9ra05188k.
- (55) Qu, M.; Chen, J.; Huang, Q.; Chen, J.; Xu, Y.; Luo, J.; Wang, K.; Gao, W.; Zheng, Y. Bioremediation of Hexavalent Chromium Contaminated Soil by a Bioleaching System with Weak Magnetic Fields. *Int. Biodeterior. Biodegrad.* 2018, 128, 41–47. https://doi.org/10.1016/j.ibiod.2016.08.022.
- (56) Singh, P.; Itankar, N.; Patil, Y. Biomanagement of Hexavalent Chromium: Current Trends and Promising Perspectives. *J. Environ. Manage.* **2021**, *279* (February 2020), 111547–111558. https://doi.org/10.1016/j.jenvman.2020.111547.
- (57) Chen, J.; Tian, Y. Hexavalent Chromium Reducing Bacteria: Mechanism of Reduction and Characteristics. *Environ. Sci. Pollut. Res.* **2021**, 28 (17), 20981–20997. https://doi.org/10.1007/s11356-021-13325-7.

- (58) Tang, X.; Huang, Y.; Li, Y.; Wang, L.; Pei, X.; Zhou, D.; He, P.; Hughes, S. S. Study on Detoxification and Removal Mechanisms of Hexavalent Chromium by Microorganisms. *Ecotoxicol. Environ. Saf.* 2021, 208, 111699–111711. https://doi.org/10.1016/j.ecoenv.2020.111699.
- (59) Ahmad, W. A.; Venil, C. K.; Nkhalambayausi Chirwa, E. M.; Wang, Y. T.; Sani, M. H.; Samad, A. F. A.; Kamaroddin, M. F. A.; Donati, E. R.; Urbieta, M. S.; Zakaria, Z. A. Bacterial Reduction of Cr(VI): Operational Challenges and Feasibility. *Curr. Pollut. Reports* 2021, 7 (2), 115–127. https://doi.org/10.1007/s40726-021-00174-8.
- (60) Singh, V.; Mishra, V. Microbial Removal of Cr(VI) by a New Bacterial Strain Isolated from the Site Contaminated with Coal Mine Effluents. *J. Environ. Chem.*Eng. 2021, 9 (5), 106279–106287. https://doi.org/10.1016/j.jece.2021.106279.
- (61) Fu, L. M.; Fu-Liu, C. S. Is Mycobacterium Tuberculosis a Closer Relative to Gram-Positive or Gram-Negative Bacterial Pathogens? *Tuberculosis* **2002**, 82 (2–3), 85–90. https://doi.org/10.1054/tube.2002.0328.
- (62) Bansal, N.; Coetzee, J. J.; Chirwa, E. M. N. In Situ Bioremediation of Hexavalent Chromium in Presence of Iron by Dried Sludge Bacteria Exposed to High Chromium Concentration. *Ecotoxicol. Environ. Saf.* 2019, 172 (January), 281–289. https://doi.org/10.1016/j.ecoenv.2019.01.094.
- Qin, S.; Xiao, W.; Zhou, C.; Pu, Q.; Deng, X.; Lan, L.; Liang, H.; Song, X.; Wu,M. *Pseudomonas Aeruginosa*: Pathogenesis, Virulence Factors, Antibiotic

- Resistance, Interaction with Host, Technology Advances and Emerging Therapeutics. *Signal Transduct. Target. Ther.* **2022**, 7 (1), 1–27. https://doi.org/10.1038/s41392-022-01056-1.
- (64) Naveenkumar, M.; Senthilkumar, K. Biomass and Bioenergy Microbial Fuel Cell for Harvesting Bio-Energy from Tannery Effluent Using Metal Mixed Biochar Electrodes. *Biomass and Bioenergy* 2021, 149 (December 2020), 106082–106089. https://doi.org/10.1016/j.biombioe.2021.106082.
- Gang, H.; Xiao, C.; Xiao, Y.; Yan, W.; Bai, R.; Ding, R.; Yang, Z.; Zhao, F. Proteomic Analysis of the Reduction and Resistance Mechanisms of *Shewanella Oneidensis* MR-1 under Long-Term Hexavalent Chromium Stress. *Environ. Int.*2019, 127 (November 2018), 94–102. https://doi.org/10.1016/j.envint.2019.03.016.
- (66) Han, R.; Li, F.; Liu, T.; Li, X.; Wu, Y.; Wang, Y.; Chen, D. Effects of Incubation Conditions on Cr(VI) Reduction by c-Type Cytochromes in Intact *Shewanella Oneidensis* MR-1 Cells. *Front. Microbiol.* **2016**, 7 (MAY), 1–12. https://doi.org/10.3389/fmicb.2016.00746.
- Yin, Y., Liu, C., Zhao, G., Chen, Y. Versatile Mechanisms and Enhanced Strategies of Pollutants Removal Mediated by *Shewanella Oneidensis*: A Review.
 J. Hazard. Mater. 2022, 440, 165187–165211.
 https://doi.org/10.1016/j.jhazmat.2022.129703.
- (68) Dikow, R. B. Genome-Level Homology and Phylogeny of Shewanella

- (Gammaproteobacteria: Lteromonadales: Shewanellaceae). *BMC Genomics* **2011**, *12*, 1–14. https://doi.org/10.1186/1471-2164-12-237.
- (69) Thorell, K.; Meier-Kolthoff, J. P.; Sjöling, Å.; Martín-Rodríguez, A. J. Whole-Genome Sequencing Redefines *Shewanella* Taxonomy. *Front. Microbiol.* **2019**, *10* (AUG), 1–14. https://doi.org/10.3389/fmicb.2019.01861.
- (70) Dai, J.; Liu, Y.; Liu, S.; Li, S.; Gao, N.; Wang, J.; Zhou, J.; Qiu, D. Differential Gene Content and Gene Expression for Bacterial Evolution and Speciation of Shewanella in Terms of Biosynthesis of Heme and Heme-Requiring Proteins. *BMC Microbiol.* **2019**, *19* (1), 1–19. https://doi.org/10.1186/s12866-019-1549-9.
- (71) Wu, G.; Jin, F. Pellicle Development of *Shewanella Oneidensis* Is an Aerotaxis-Piloted and Energy-Dependent Process. *Biochem. Biophys. Res. Commun.* **2019**, 519 (1), 127–133. https://doi.org/10.1016/j.bbrc.2019.08.144.
- (72) Lovley, D. R. The Microbe Electric: Conversion of Organic Matter to Electricity.

 *Curr. Opin. Biotechnol. 2008, 19 (6), 564–571.

 https://doi.org/10.1016/j.copbio.2008.10.005.
- (73) Kheirabadi, M.; Mahmoodi, R.; Mollania, N.; Kheirabadi, M. Fast Chromium Removal by *Shewanella* Sp.: An Enzymatic Mechanism Depending on Serine Protease. *Int. J. Environ. Sci. Technol.* **2020**, *17* (1), 143–152. https://doi.org/10.1007/s13762-019-02338-y.
- (74) Zhang, S.; Zhang, L.; Chen, P.; Rong, H.; Li, S. Deciphering the Microbial Patterns

- of Anammox Process under Hexavalent Chromium Stress: Abundant and Rare Subcommunity Respond Differently. *J. Hazard. Mater.* **2021**, *416* (April), 125850–125860. https://doi.org/10.1016/j.jhazmat.2021.125850.
- (75) Baaziz, H.; Gambari, C.; Boyeldieu, A.; Chaouche, A. A.; Alatou, R.; Méjean, V.; Jourlin-Castelli, C.; Fons, M. ChrASO, the Chromate Efflux Pump of *Shewanella Oneidensis*, Improves Chromate Survival and Reduction. *PLoS One* **2017**, *12* (11), 1–15. https://doi.org/10.1371/journal.pone.0188516.
- (76) Lowe, K. L.; Straube, W.; Jones-Meehan, J. Aerobic and Anaerobic Reduction of Cr(VI) by *Shewanella Oneidensis*. *Acta Biotechnol.* **2003**, 23, 161–178.
- (77) Elahi, A.; Rehman, A. Multiple Metal Resistance and Cr⁶⁺ Reduction by Bacterium, *Staphylococcus Sciuri* A-HS1, Isolated from Untreated Tannery Effluent. *J. King Saud Univ. Sci.* **2019**, *31* (4), 1005–1013. https://doi.org/10.1016/j.jksus.2018.07.016.
- (78) Mohamed, A.; Yu, L.; Fang, Y.; Ashry, N.; Riahi, Y.; Uddin, I.; Dai, K.; Huang, Q. Iron Mineral-Humic Acid Complex Enhanced Cr(VI) Reduction by *Shewanella Oneidensis* MR-1. *Chemosphere* 2020, 247, 125902–125914. https://doi.org/10.1016/j.chemosphere.2020.125902.
- (79) Mohamed, A.; Sun, B.; Yu, C.; Gu, X.; Ashry, N.; Riahi, Y.; Dai, K.; Huang, Q. Size Effect of Hematite Particles on the Cr(VI) Reduction by *Shewanella Oneidensis* MR-1. *J. Environ. Chem. Eng.* 2021, 9 (2), 105096–105106. https://doi.org/10.1016/j.jece.2021.105096.

- (80) Cheng, H.; Jing, Z.; Yang, L.; Lu, A.; Ren, G.; Liu, J. Sunlight-Triggered Synergy of Hematite and *Shewanella Oneidensis* MR-1 in Cr(VI) Removal. *Geochim. Cosmochim. Acta* **2021**, *305*, 19–32. https://doi.org/10.1016/j.gca.2021.04.034.
- (81) Schröder, U. Anodic Electron Transfer Mechanisms in Microbial Fuel Cells and Their Energy Efficiency. *Phys. Chem. Chem. Phys.* 2007, 9 (21), 2619–2629. https://doi.org/10.1039/b703627m.
- (82) Parker, D. L.; Borer, P.; Bernier-Latmani, R. The Response of *Shewanella Oneidensis* MR-1 to Cr(III) Toxicity Differs from That to Cr(VI). *Front. Microbiol.* **2011**, 2 (NOV), 1–14. https://doi.org/10.3389/fmicb.2011.00223.
- (83) Coursolle, D.; Baron, D. B.; Bond, D. R.; Gralnick, J. A. The Mtr Respiratory Pathway Is Essential for Reducing Flavins and Electrodes in *Shewanella Oneidensis*. *J. Bacteriol.* **2010**, 192 (2), 467–474. https://doi.org/10.1128/JB.00925-09.
- Bill, M.; Conrad, M. E.; Faybishenko, B.; Larsen, J. T.; Geller, J. T.; Borglin, S. E.; Beller, H. R. Use of Carbon Stable Isotopes to Monitor Biostimulation and Electron Donor Fate in Chromium-Contaminated Groundwater. *Chemosphere*2019, 235, 440–446. https://doi.org/10.1016/j.chemosphere.2019.06.056.
- (85) Pinchuk, G. E.; Rodionov, D. A.; Yang, C.; Li, X.; Osterman, A. L.; Dervyn, E.; Geydebrekht, O. V.; Reed, S. B.; Romine, M. F.; Collart, F. R.; Scott, J. H.; Fredrickson, J. K.; Beliaev, A. S. Genomic Reconstruction of *Shewanella Oneidensis* MR-1 Metabolism Reveals a Previously Uncharacterized Machinery

- for Lactate Utilization. *Proc. Natl. Acad. Sci. U. S. A.* **2009**, *106* (8), 2874–2879. https://doi.org/10.1073/pnas.0806798106.
- (86) Pinchuk, G. E.; Geydebrekht, O. V.; Hill, E. A.; Reed, J. L.; Konopka, A. E.; Beliaev, A. S.; Fredrickson, J. K. Pyruvate and Lactate Metabolism by *Shewanella Oneidensis* MR-1 under Fermentation, Oxygen Limitation, and Fumarate Respiration Conditions. *Appl. Environ. Microbiol.* 2011, 77 (23), 8234–8240. https://doi.org/10.1128/AEM.05382-11.
- (87) Brutinel, E. D.; Gralnick, J. A. Preferential Utilization of D-Lactate by *Shewanella Oneidensis*. *Appl. Environ. Microbiol.* **2012**, 78 (23), 8474–8476. https://doi.org/10.1128/AEM.02183-12.
- (88) Serres, M. H.; Riley, M. Genomic Analysis of Carbon Source Metabolism of *Shewanella Oneidensis* MR-1: Predictions versus Experiments. *J. Bacteriol.* **2006**, *188* (13), 4601–4609. https://doi.org/10.1128/JB.01787-05.
- (89) Kouzuma, A.; Kasai, T.; Hirose, A.; Watanabe, K. Catabolic and Regulatory Systems in *Shewanella Oneidensis* MR-1 Involved in Electricity Generation in Microbial Fuel Cells. *Front. Microbiol.* **2015**, *6*, 1–11. https://doi.org/10.3389/fmicb.2015.00609.
- (90) Kane, A. L.; Brutinel, E. D.; Joo, H.; Maysonet, R.; VanDrisse, C. M.; Kotloski, N. J.; Gralnick, J. A. Formate Metabolism in *Shewanella Oneidensis* Generates Proton Motive Force and Prevents Growth without an Electron Acceptor. *J. Bacteriol.* 2016, 198 (8), 1337–1346. https://doi.org/10.1128/JB.00927-15.

- (91) Ma, L.; Du, Y.; Chen, S.; Du, D.; Ye, H.; Zhang, T. C. Highly Efficient Removal of Cr(VI) from Aqueous Solution by Pinecone Biochar Supported Nanoscale Zero-Valent Iron Coupling with *Shewanella Oneidensis* MR-1. *Chemosphere* 2022, 287 (P2), 132184. https://doi.org/10.1016/j.chemosphere.2021.132184.
- (92) Ri, C.; Tang, J.; Liu, F.; Lyu, H.; Li, F. Enhanced Microbial Reduction of Aqueous Hexavalent Chromium by *Shewanella Oneidensis* MR-1 with Biochar as Electron Shuttle. *J. Environ. Sci. (China)* **2022**, *113*, 12–25. https://doi.org/10.1016/j.jes.2021.05.023.
- (93) Cheng, Z. H.; Xiong, J. R.; Min, D.; Cheng, L.; Liu, D. F.; Li, W. W.; Jin, F.; Yang, M.; Yu, H. Q. Promoting Bidirectional Extracellular Electron Transfer of *Shewanella Oneidensis* MR-1 for Hexavalent Chromium Reduction via Elevating Intracellular CAMP Level. *Biotechnol. Bioeng.* 2020, 117 (5), 1294–1303. https://doi.org/10.1002/bit.27305.
- (94) Kouzuma, A. Molecular Mechanisms Regulating the Catabolic and Electrochemical Activities of *Shewanella Oneidensis* MR-1. *Biosci. Biotechnol. Biochem.* **2021**, 85 (7), 1572–1581. https://doi.org/10.1093/bbb/zbab088.
- (95) Tang, Y. J.; Hwang, J. S.; Wemmer, D. E.; Keasling, J. D. Shewanella Oneidensis
 MR-1 Fluxome under Various Oxygen Conditions. Appl. Environ. Microbiol.
 2007, 73 (3), 718–729. https://doi.org/10.1128/AEM.01532-06.
- (96) Hunt, K. A.; Flynn, J. M.; Naranjo, B.; Shikhare, I. D.; Gralnick, J. A. Substrate-Level Phosphorylation Is the Primary Source of Energy Conservation during

- Anaerobic Respiration of *Shewanella Oneidensis* Strain MR-1. *J. Bacteriol.* **2010**, 192 (13), 3345–3351. https://doi.org/10.1128/JB.00090-10.
- (97) Scott, J. H.; Nealson, K. H. A Biochemical Study of the Intermediary Carbon Metabolism of *Shewanella Putrefaciens*. *J. Bacteriol*. **1994**, *176* (11), 3408–3411. https://doi.org/10.1128/jb.176.11.3408-3411.1994.
- (98) Beliaev, A. S.; Klingeman, D. M.; Klappenbach, J. A.; Wu, L.; Romine, M. F.; Tiedje, J. M.; Nealson, K. H.; Fredrickson, J. K.; Zhou, J. Global Transcriptome Analysis of *Shewanella Oneidensis* MR-1 Exposed to Different Terminal Electron Acceptors. *J. Bacteriol.* 2005, 187 (20), 7138–7145. https://doi.org/10.1128/JB.187.20.7138-7145.2005.
- (99) Hartshorne, R. S.; Jepson, B. N.; Clarke, T. A.; Field, S. J.; Fredrickson, J.; Zachara, J.; Shi, L.; Butt, J. N.; Richardson, D. J. Characterization of *Shewanella Oneidensis* MtrC: A Cell-Surface Decaheme Cytochrome Involved in Respiratory Electron Transport to Extracellular Electron Acceptors. *J. Biol. Inorg. Chem.* 2007, 12 (7), 1083–1094. https://doi.org/10.1007/s00775-007-0278-y.
- (100) Richardson, D. J.; Butt, J. N.; Fredrickson, J. K.; Zachara, J. M.; Shi, L.; Edwards, M. J.; White, G.; Baiden, N.; Gates, A. J.; Marritt, S. J.; Clarke, T. A. The "porin-Cytochrome" Model for Microbe-to-Mineral Electron Transfer. *Mol. Microbiol.* 2012, 85 (2), 201–212. https://doi.org/10.1111/j.1365-2958.2012.08088.x.
- (101) McLean, J. S.; Majors, P. D.; Reardon, C. L.; Bilskis, C. L.; Reed, S. B.; Romine,M. F.; Fredrickson, J. K. Investigations of Structure and Metabolism within

- Shewanella Oneidensis MR-1 Biofilms. J. Microbiol. Methods **2008**, 74 (1), 47–56. https://doi.org/10.1016/j.mimet.2008.02.015.
- (102) Gralnick, J. A.; Vali, H.; Lies, D. P.; Newman, D. K. Extracellular Respiration of Dimethyl Sulfoxide by *Shewanella Oneidensis* Strain MR-1. *Proc. Natl. Acad. Sci. U. S. A.* 2006, *103* (12), 4669–4674. https://doi.org/10.1073/pnas.0505959103.
- (103) Hartshorne, R. S.; Reardon, C. L.; Ross, D.; Nuester, J.; Clarke, T. A.; Gates, A. J.; Mills, P. C.; Fredrickson, J. K.; Zachara, J. M.; Shi, L.; Beliaev, A. S.; Marshall, M. J.; Tien, M.; Brantley, S.; Butt, J. N.; Richardson, D. J. Characterization of an Electron Conduit between Bacteria and the Extracellular Environment. *Proc. Natl. Acad. Sci. U. S. A.* 2009, 106 (52), 22169–22174. https://doi.org/10.1073/pnas.0900086106.
- (104) Coursolle, D.; Gralnick, J. A. Reconstruction of Extracellular Respiratory Pathways for Iron (III) Reduction in *Shewanella Oneidensis* Strain MR-1. *Front. Microbiol.* **2012**, *3* (February), 1–11. https://doi.org/10.3389/fmicb.2012.00056.
- (105) Clarke, T. A.; Edwards, M. J.; Gates, A. J.; Hall, A.; White, G. F.; Bradley, J.; Reardon, C. L.; Shi, L.; Beliaev, A. S.; Marshall, M. J.; Wang, Z.; Watmough, N. J.; Fredrickson, J. K.; Zachara, J. M.; Butt, J. N.; Richardson, D. J. Structure of a Bacterial Cell Surface Decaheme Electron Conduit. *Proc. Natl. Acad. Sci. U. S. A.* 2011, 108 (23), 9384–9389. https://doi.org/10.1073/pnas.1017200108.
- (106) Slate, A. J.; Whitehead, K. A.; Brownson, D. A. C.; Banks, C. E. Microbial Fuel Cells: An Overview of Current Technology. *Renew. Sustain. Energy Rev.* **2019**,

- 101 (March 2018), 60–81. https://doi.org/10.1016/j.rser.2018.09.044.
- (107) Maruthupandy, M.; Anand, M.; Maduraiveeran, G.; Sait, A.; Beevi, H.; Priya, R. J. Electrical Conductivity Measurements of Bacterial Electrical Conductivity Measurements of Bacterial Nanowires from *Pseudomonas Aeruginosa*. Adv. Nat. Sci. Nanosci. Nanotechnol. 2015, 6, 045007–045014.
- (108) Pirbadian, S.; Barchinger, S. E.; Leung, K. M.; Byun, H. S.; Jangir, Y.; Bouhenni, R. A.; Reed, S. B.; Romine, M. F.; Saffarini, D. A.; Shi, L.; Gorby, Y. A.; Golbeck, J. H.; El-Naggar, M. Y. *Shewanella Oneidensis* MR-1 Nanowires Are Outer Membrane and Periplasmic Extensions of the Extracellular Electron Transport Components. *Proc. Natl. Acad. Sci. U. S. A.* 2014, *111* (35), 12883–12888. https://doi.org/10.1073/pnas.1410551111.
- (109) Rabaey, K.; Boon, N.; Höfte, M.; Verstraete, W. Microbial Phenazine Production Enhances Electron Transfer in Biofuel Cells. *Environ. Sci. Technol.* **2005**, *39* (9), 3401–3408. https://doi.org/10.1021/es0485630.
- (110) Logan, B. E.; Hamelers, B.; Rozendal, R.; Schröder, U.; Keller, J.; Freguia, S.; Aelterman, P.; Verstraete, W.; Rabaey, K. Microbial Fuel Cells: Methodology and Technology. *Environ. Sci. Technol.* 2006, 40 (17), 5181–5192. https://doi.org/10.1021/es0605016.
- (111) Carra, A.; Villalta, P. W.; He, J.; Yao, X.; Hamers, R. J.; Balbo, S.; Vivian, Z.; Haynes, C. L. Nanoscale Battery Cathode Materials Induce DNA Damage in Bacteria. *Chem. Sci.* **2020**, *11*, 11244–11258. https://doi.org/10.1039/d0sc02987d.

- (112) Mitchell, S. L.; Hudson-Smith, N. V; Cahill, M. S.; Reynolds, B. N.; Frand, S. D.; Green, C. M.; Wang, C.; Hang, M. N.; Hernandez, R. T.; Hamers, R. J. Chronic Exposure to Complex Metal Oxide Nanoparticles Elicits Rapid Resistance in *Shewanella Oneidensis* MR-1. *Chem. Sci.* 2019, 10 (42), 9768–9781.
- (113) Hang, M. N.; Gunsolus, I. L.; Wayland, H.; Melby, E. S.; Mensch, A. C.; Hurley, K. R.; Pedersen, J. A.; Haynes, C. L.; Hamers, R. J. Impact of Nanoscale Lithium Nickel Manganese Cobalt Oxide (NMC) on the Bacterium *Shewanella Oneidensis* MR-1. *Chem. Mater.* 2016, 28, 1092–1100. https://doi.org/10.1021/acs.chemmater.5b04505.
- (114) Liu, T.; Li, X.; Li, F.; Han, R.; Wu, Y.; Yuan, X.; Wang, Y. In Situ Spectral Kinetics of Cr(VI) Reduction by c-Type Cytochromes in A Suspension of Living *Shewanella Putrefaciens* 200. *Sci. Rep.* **2016**, *6*, 1–11. https://doi.org/10.1038/srep29592.
- (115) Mpofu, A. B.; Oyekola, O. O.; Welz, P. J. Anaerobic Treatment of Tannery Wastewater in the Context of a Circular Bioeconomy for Developing Countries. *J. Clean. Prod.* 2021, 296, 126490–126504. https://doi.org/10.1016/j.jclepro.2021.126490.
- (116) Xiao, Y.; Xiao, C.; Zhao, F. Long-Term Adaptive Evolution of *Shewanella Oneidensis* MR-1 for Establishment of High Concentration Cr(VI) Tolerance. *Front. Environ. Sci. Eng.* **2020**, *14* (1), 1–11. https://doi.org/10.1007/s11783-019-1182-8.

- (117) Du, Q.; Li, T.; Li, N.; Wang, X. Protection of Electroactive Biofilm from Extreme Acid Shock by Polydopamine Encapsulation. *Environ. Sci. Technol. Lett.* **2017**, *4* (8), 345–349. https://doi.org/10.1021/acs.estlett.7b00242.
- (118) Xue, Y.; Chen, Y. X.; Yu, Y. Y.; Yong, Y. C. Bacterial Nanoencapsulation with Cytocompatible Atom Transfer Radical Polymerization for Improved Cr(VI) Removal. *Chem. Eng. J.* **2020**, *387* (January), 124068–124074. https://doi.org/10.1016/j.cej.2020.124068.
- (119) Chen, S.; Arnold, W. A.; Novak, P. J. Encapsulation Technology to Improve Biological Resource Recovery: Recent Advancements and Research Opportunities. *Environ. Sci. Water Res. Technol.* **2021**, 7 (1), 16–23. https://doi.org/10.1039/d0ew00750a.
- (120) Cheng, L.; He, R.; Min, D.; Li, W.; Liu, D.; Yu, H. Engineering a Rhamnose-Inducible System to Enhance the Extracellular Electron Transfer Ability of *Shewanella* Genus for Improved Cr(VI) Reduction. *ACS ES&T Eng.* **2021**, *1* (5), 842–850. https://doi.org/10.1021/acsestengg.0c00125.
- (121) Borges, C.; Gutterres, M. Tannery Wastewater as Nutrient Supply in Production of Biogas from Solid Tannery Wastes Mixed through Anaerobic Co-Digestion.
 Process Saf. Environ. Prot. 2020, 135, 38–45.
 https://doi.org/10.1016/j.psep.2019.11.037.
- (122) An, H.; Tian, T.; Wang, Z.; Jin, R.; Zhou, J. Role of Extracellular Polymeric Substances in the Immobilization of Hexavalent Chromium by *Shewanella*

- *Putrefaciens* CN32 Unsaturated Biofilms. *Sci. Total Environ.* **2021**, No. 810, 151184–151192. https://doi.org/10.1016/j.scitotenv.2021.151184.
- (123) Yu, C.; Zhang, Y.; Fang, Y.; Tan, Y.; Dai, K.; Liu, S.; Huang, Q. Shewanella Oneidensis MR-1 Impregnated Ca-Alginate Capsule for Efficient Cr(VI) Reduction and Cr(III) Adsorption. *Environ. Sci. Pollut. Res.* **2020**, *27* (14), 16745–16753.
- (124) Li, F.; Tang, Q.; Fan, Y.; Li, Y.; Li, J.; Wu, J.; Luo, C. Developing a Population-State Decision System for Intelligently Reprogramming Extracellular Electron Transfer in *Shewanella Oneidensis*. *Natl. Acad. Sci.* **2020**, *117* (37), 23001–23010. https://doi.org/10.1073/pnas.2006534117.
- (125) Li, F. H.; Min, D.; Cheng, Z. H.; Li, J.; Wu, J. H.; Tang, Q.; Yu, H. Q. Systematically Assessing Genetic Strategies for Engineering Electroactive Bacterium to Promote Bioelectrochemical Performances and Pollutant Removal. Sustain. Energy Technol. Assessments 2021, 47 (October 2020), 101506–101514. https://doi.org/10.1016/j.seta.2021.101506.
- (126) Li, J.; Tang, Q.; Li, Y.; Fan, Y. Y.; Li, F. H.; Wu, J. H.; Min, D.; Li, W. W.; Lam, P. K. S.; Yu, H. Q. Rediverting Electron Flux with an Engineered CRISPR-DdAsCpf1 System to Enhance the Pollutant Degradation Capacity of Shewanella Oneidensis. *Environ. Sci. Technol.* 2020, 54 (6), 3599–3608. https://doi.org/10.1021/acs.est.9b06378.
- (127) Hall-Stoodley, L.; Costerton, J. W.; Stoodley, P. Bacterial Biofilms: From the

- Natural Environment to Infectious Diseases. *Nat. Rev. Microbiol.* **2004**, 2 (2), 95–108. https://doi.org/10.1038/nrmicro821.
- (128) Kumar, A.; Hsu, L. H.-H.; Kavanagh, P.; Barrière, F.; Lens, P. N. L.; Lapinsonnière, L.; Lienhard V, J. H.; Schröder, U.; Jiang, X.; Leech, D. The Ins and Outs of Microorganism–Electrode Electron Transfer Reactions. *Nat. Rev. Chem.* **2017**, *1* (3), 0024–0036. https://doi.org/10.1038/s41570-017-0024.
- (129) Zhang, Y.; Liu, M.; Zhou, M.; Yang, H.; Liang, L.; Gu, T. Microbial Fuel Cell Hybrid Systems for Wastewater Treatment and Bioenergy Production: Synergistic Effects, Mechanisms and Challenges. Renew. Susta. Renew. Sustain. Energy Rev. 2019, 103 (December 2018), 13–29. https://doi.org/10.1016/j.rser.2018.12.027.
- (130) Hsu, L.; Masuda, S. A.; Nealson, K. H.; Pirbazari, M. Evaluation of Microbial Fuel Cell *Shewanella* Biocathodes for Treatment of Chromate Contamination. *RSC Adv.* **2012**, *2* (13), 5844–5855. https://doi.org/10.1039/c2ra20478a.
- (131) Nuryana, I. F.; Puspitasari, R.; Juliastuti, S. R. Study of Electrode Modification and Microbial Concentration for Microbial Fuel Cell Effectivity from Molasses Waste and Reduction of Heavy Metal Cr (VI) by Continue Dual Chamber Reactor. IOP Conf. Ser. Mater. Sci. Eng. 2020, 823 (1), 012016–012025. https://doi.org/10.1088/1757-899X/823/1/012016.
- (132) Liu, L.; Yuan, Y.; Li, F. bai; Feng, C. hua. In-Situ Cr(VI) Reduction with Electrogenerated Hydrogen Peroxide Driven by Iron-Reducing Bacteria.

 Bioresour. Technol.** 2011, 102 (3), 2468–2473.

- https://doi.org/10.1016/j.biortech.2010.11.013.
- (133) Wu, G.; Wan, F.; Fu, H.; Li, N.; Gao, H. A Matter of Timing: Contrasting Effects of Hydrogen Sulfide on Oxidative Stress Response in *Shewanella Oneidensis*. *J. Bacteriol.* **2015**, *197* (22), 3563–3572. https://doi.org/10.1128/JB.00603-15.
- (134) Chen, M.; Zhou, X.; Chen, X.; Cai, Q.; Zeng, R. J.; Zhou, S. Mechanisms of Nitrous Oxide Emission during Photoelectrotrophic Denitrification by Self-Photosensitized *Thiobacillus Denitrificans*. *Water Res.* **2020**, *172* (2), 115501–115508. https://doi.org/10.1016/j.watres.2020.115501.
- (135) Matharu, R. K.; Tabish, T. A.; Trakoolwilaiwan, T.; Mansfield, J.; Moger, J.; Wu, T.; Lourenço, C.; Chen, B.; Ciric, L.; Parkin, I. P.; Edirisinghe, M. Microstructure and Antibacterial Efficacy of Graphene Oxide Nanocomposite Fibres. *J. Colloid Interface Sci.* 2020, 571, 239–252. https://doi.org/10.1016/j.jcis.2020.03.037.
- (136) Chen, Y. X.; Liu, X.; Fang, Z.; Zhang, C. L.; Abbas, S. Z.; Yu, Y. Y.; Yong, Y. C. Self-Assembling of Shewanella@rGO@Pd Bionanohybrid for Synergistic Bio-Abiotic Removal of Cr(VI). *J. Chem. Technol. Biotechnol.* **2020**, *95* (8), 2222–2228. https://doi.org/10.1002/jctb.6409.
- (137) Sundman, A.; Vitzthum, A. L.; Adaktylos-surber, K.; Figueroa, A. I.; van der Laan, G.; Daus, B.; Kappler, A.; Byrne, J. M.; Laan, G. Van Der; Daus, B.; Kappler, A.; Byrne, J. M. Effect of Fe-Metabolizing Bacteria and Humic Substances on Magnetite Nanoparticle Reactivity towards Arsenic and Chromium. *J. Hazard. Mater.* 2020, 384 (October 2019), 121450–121456.

- https://doi.org/10.1016/j.jhazmat.2019.121450.
- (138) Arakha, M.; Pal, S.; Samantarrai, D.; Panigrahi, T. K. Antimicrobial Activity of Iron Oxide Nanoparticle upon Modulation of Nanoparticle-Bacteria Interface. *Sci. Rep.* **2015**, *5* (1), 1–12. https://doi.org/10.1038/srep14813.
- Qu, C.; Qian, S.; Chen, L.; Guan, Y.; Zheng, L.; Liu, S.; Chen, W.; Cai, P.; Huang,
 Q. Size-Dependent Bacterial Toxicity of Hematite Particles. *Environ. Sci. Technol.*2019, 53 (14), 8147–8156. https://doi.org/10.1021/acs.est.9b00856.
- (140) Zhou, Y.; Duan, J.; Jiang, J.; Yang, Z. Effect of TOC Concentration of Humic Substances as an Electron Shuttle on Redox Functional Groups Stimulating Microbial Cr(VI) Reduction. *Int. J. Environ. Res. Public Health* 2022, 19 (5), 2600-2610. https://doi.org/10.3390/ijerph19052600.
- (141) Ma, L.; Du, Y.; Chen, S.; Zhang, F.; Zhan, W.; Du, D.; Zhang, T. C. Nanoscale Zero-Valent Iron Coupling with *Shewanella Oneidensis* MR-1 for Enhanced Reduction/Removal of Aqueous Cr(VI). *Sep. Purif. Technol.* **2021**, 277 (August), 119488. https://doi.org/10.1016/j.seppur.2021.119488.
- (142) Liu, L.; Zhao, J.; Yin, W.; Lv, S.; Su, M.; Li, P.; Zheng, X.; Chiang, P.; Wu, J. Enhanced Immobilization of Cr(VI) by a Fe⁰–Microorganisms Composite System:

 Benchmark and Pot Experiments. *J. Environ. Qual.* **2021**, *50* (5), 1123–1134. https://doi.org/10.1002/jeq2.20261.
- (143) Wu, H.; Wu, Q.; Zhang, J.; Gu, Q.; Wei, L.; Guo, W.; He, M. Chromium Ion

- Removal from Raw Water by Magnetic Iron Composites and *Shewanella Oneidensis* MR-1. *Sci. Rep.* **2019**, *9* (1), 1–16. https://doi.org/10.1038/s41598-018-37470-1.
- (144) Dong, H.; Li, L.; Lu, Y.; Cheng, Y.; Wang, Y.; Ning, Q.; Wang, B.; Zhang, L.; Zeng, G. Integration of Nanoscale Zero-Valent Iron and Functional Anaerobic Bacteria for Groundwater Remediation: A Review. *Environ. Int.* 2019, 124, 265–277. https://doi.org/10.1016/j.envint.2019.01.030.
- (145) Wang, Y.; Yang, J.; Han, H.; Hu, Y.; Wang, J.; Feng, Y.; Yu, B.; Xia, X.; Darma, A. Differential Transformation Mechanisms of Exotic Cr(VI) in Agricultural Soils with Contrasting Physio-Chemical and Biological Properties. *Chemosphere* 2021, 279 (12), 130546. https://doi.org/10.1016/j.chemosphere.2021.130546.
- (146) Eyvazi, B.; Jamshidi-zanjani, A.; Khodadadi, A. Synthesis of Nano-Magnetic MnFe₂O₄ to Remove Cr(III) and Cr(VI) from Aqueous Solution: A Comprehensive Study. *Environ. Pollut.* **2020**, 265, 113685–113695. https://doi.org/10.1016/j.envpol.2019.113685.
- (147) Peng, Y.; Wang, Z.; Liu, W.; Zhang, H.; Zuo, W.; Tang, H.; Chen, F.; Wang, B. Size- and Shape-Dependent Peroxidase-like Catalytic Activity of MnFe₂O₄ Nanoparticles and Their Applications in Highly Efficient Colorimetric Detection of Target Cancer Cells. *Dalt. Trans.* 2015, 44 (28), 12871–12877. https://doi.org/10.1039/c5dt01585e.
- (148) Wu, C. W.; Unnikrishnan, B.; Tseng, Y. T.; Wei, S. C.; Chang, H. T.; Huang, C.

- C. Mesoporous Manganese Oxide/Manganese Ferrite Nanopopcorns with Dual Enzyme Mimic Activities: A Cascade Reaction for Selective Detection of Ketoses.

 J. Colloid Interface Sci. 2019, 541, 75–85. https://doi.org/10.1016/j.jcis.2019.01.061.
- (149) Verma, V.; Kaur, M.; Sharma, S. Superoxide Dismutase Mimic Activity of Spinel Ferrite MFe₂O₄ (M = Mn, Co and Cu) Nanoparticles. *Bull. Mater. Sci.* **2019**, *42* (3), 1–6. https://doi.org/10.1007/s12034-019-1783-7.
- (150) Maeda, Y.; Wei, Z.; Ikezoe, Y.; Tam, E.; Matsui, H. Biomimetic Crystallization of MnFe₂O₄ Mediated by Peptide-Catalyzed Esterification at Low Temperature. *ChemNanoMat* 2016, 2 (5), 419–422. https://doi.org/10.1002/cnma.201500181.
- (151) Ma, Y.; Wu, X.; Shi, Z.; Li, X.; Qian, S.; Sun, X.; Sun, W.; Guo, C.; Li, C. M. Photoactive Manganese Ferrite-Modified Bacterial Anode to Simultaneously Boost Both Mediated and Direct Electron Transfer Processes in Microbial Fuel Cells. ACS Sustain. Chem. Eng. 2022, 10 (10), 3355–3362. https://doi.org/10.1021/acssuschemeng.1c08683.
- (152) Khilari, S.; Pandit, S.; Varanasi, J. L.; Das, D.; Pradhan, D. Bifunctional Manganese Ferrite/Polyaniline Hybrid as Electrode Material for Enhanced Energy Recovery in Microbial Fuel Cell. ACS Appl. Mater. Interfaces 2015, 7 (37), 20657–20666. https://doi.org/10.1021/acsami.5b05273.
- (153) Hu, J.; Lo, I. M. C.; Chen, G. Comparative Study of Various Magnetic Nanoparticles for Cr (VI) Removal. Sep. Purif. Technol. 2007, 56 (3), 249–256.

- https://doi.org/10.1016/j.seppur.2007.02.009.
- (154) Hu, J.; Lo, I. M. C.; Chen, G. Fast Removal and Recovery of Cr(VI) Using Surface-Modified Jacobsite (MnFe₂O₄) Nanoparticles. *Langmuir* **2005**, *21* (24), 11173–11179. https://doi.org/10.1021/la051076h.
- (155) Luther, S.; Brogfeld, N.; Kim, J.; Parsons, J. G. Study of the Thermodynamics of Chromium(III) and Chromium(VI) Binding to Iron(II/III) Oxide or Magnetite or Ferrite and Magnanese(II) Iron(III) Oxide or Jacobsite or Manganese Ferrite Nanoparticles. *J. Colloid Interface Sci.* **2013**, *400*, 97–103. https://doi.org/10.1016/j.jcis.2013.02.036.
- (156) Wang, J.; Xu, Q.; Yin, W.; Hou, J.; Wang, S.; Wang, X. Mechanism Analysis of MnFe₂O₄/FeSX for Removal of Cr(VI) from Aqueous Phase. *Ecotoxicol. Environ.*Saf. 2021, 217 (November 2020), 112209–112216. https://doi.org/10.1016/j.ecoenv.2021.112209.
- (157) Cui, H. J.; Shi, J. W.; Yuan, B.; Fu, M. L. Synthesis of Porous Magnetic Ferrite Nanowires Containing Mn and Their Application in Water Treatment. *J. Mater. Chem. A* **2013**, *1* (19), 5902–5907. https://doi.org/10.1039/c3ta01692g.
- (158) Ahalya, K.; Suriyanarayanan, N.; Ranjithkumar, V. Effect of Cobalt Substitution on Structural and Magnetic Properties and Chromium Adsorption of Manganese Ferrite Nano Particles. *J. Magn. Magn. Mater.* 2014, 372, 208–213. https://doi.org/10.1016/j.jmmm.2014.07.030.

- (159) Vamvakidis, K.; Katsikini, M.; Vourlias, G.; Angelakeris, M.; Paloura, E. C.; Dendrinou-Samara, C. Composition and Hydrophilicity Control of Mn-Doped Ferrite (Mn_xFe_{3-x}O₄) Nanoparticles Induced by Polyol Differentiation. *Dalt. Trans.* **2015**, *44* (12), 5396–5406. https://doi.org/10.1039/c5dt00212e.
- (160) Martinez-Vargas, S.; Martínez, A. I.; Hernández-Beteta, E. E.; O. F. Mijangos-Ricardez, V. Vázquez-Hipólito, C. Patiño-Carachure, H. H.-F.; López-Luna, J. Arsenic Adsorption on Cobalt and Manganese Ferrite Nanoparticles. *J. Mater. Sci.* 2017, 52 (11), 6205–6215. https://doi.org/10.1007/s10853-017-0852-9.
- (161) Shebha Anandhi, J.; Antilen Jacob, G.; Justin Joseyphus, R. Factors Affecting the Heating Efficiency of Mn-Doped Fe₃O₄ Nanoparticles. *J. Magn. Magn. Mater.*2020, 512 (December 2019), 166992–167001. https://doi.org/10.1016/j.jmmm.2020.166992.
- (162) Li, M.; Gao, Q.; Wang, T.; Gong, Y. S.; Han, B.; Xia, K. S.; Zhou, C. G. Solvothermal Synthesis of Mn_xFe_{3-x}O₄ Nanoparticles with Interesting Physicochemical Characteristics and Good Catalytic Degradation Activity. *Mater. Des.* **2016**, *97*, 341–348. https://doi.org/10.1016/j.matdes.2016.02.103.
- (163) Lasheras, X.; Insausti, M.; De La Fuente, J. M.; Gil De Muro, I.; Castellanos-Rubio, I.; Marcano, L.; Fernández-Gubieda, M. L.; Serrano, A.; Martín-Rodríguez, R.; Garaio, E.; García, J. A.; Lezama, L. Mn-Doping Level Dependence on the Magnetic Response of Mn_xFe_{3-x}O₄ Ferrite Nanoparticles. *Dalt. Trans.* 2019, 48 (30), 11480–11491. https://doi.org/10.1039/c9dt01620a.

- (164) Asdrubali, F.; Alessandro, F. D.; Schiavoni, S. Sustainable Materials and Technologies A Review of Unconventional Sustainable Building Insulation Materials. *Sustain. Mater. Technol.* **2020**, *4* (2015), 1–17. https://doi.org/10.1016/j.susmat.2015.05.002.
- (165) Zuazua-ros, A.; Vidaurre-arbizu, M.; Silvia, P. From the Leather Industry to Building Sector: Exploration of Potential Applications of Discarded Solid Wastes. J. Clean. Prod. 2021, 291, 125960–125971. https://doi.org/10.1016/j.jclepro.2021.125960.
- (166) Lin, H.; Zhang, P.; Zeng, L.; Jiao, B.; Shiau, Y.; Li, D. Preparation of Glass-Ceramics via Cosintering and Solidification of Hazardous Waste Incineration Residue and Chromium-Containing Sludge. ACS Omega 2021, 6 (37), 23723–23730. https://doi.org/10.1021/acsomega.1c01659.
- (167) Majee, S.; Halder, G.; Mandal, D. D.; Tiwari, O. N.; Mandal, T. Transforming Wet Blue Leather and Potato Peel into an Eco-Friendly Bio-Organic NPK Fertilizer for Intensifying Crop Productivity and Retrieving Value-Added Recyclable Chromium Salts. *J. Hazard. Mater.* 2021, 411 (January), 125046–125057. https://doi.org/10.1016/j.jhazmat.2021.125046.
- (168) Mensah, M. B.; Lewis, D. J.; Boadi, N. O.; Awudza, J. A. M. Heavy Metal Pollution and the Role of Inorganic Nanomaterials in Environmental Remediation.

 R. Soc. Open Sci. 2021, 8 (10), 201485–201505. https://doi.org/10.1098/rsos.201485.

- (169) Qin, H.; He, Y.; Xu, P.; Huang, D.; Wang, Z.; Wang, H. Spinel Ferrites (MnFe₂O₄): Synthesis, Improvement and Catalytic Application in Environment and Energy Field. *Adv. Colloid Interface Sci.* **2021**, 294 (July), 102486–102507. https://doi.org/10.1016/j.cis.2021.102486.
- (170) Fiévet, F.; Ammar-Merah, S.; Brayner, R.; Chau, F.; Giraud, M.; Mammeri, F.; Peron, J.; Piquemal, J.-Y.; Sicard, L.; Viau, G. The Polyol Process: A Unique Method for Easy Access to Metal Nanoparticles with Tailored Sizes, Shapes and Compositions. *Chem. Soc. Rev.* 2018, 47 (14), 5187–5233.
- (171) Dong, H.; Chen, Y. C.; Feldmann, C. Polyol Synthesis of Nanoparticles: Status and Options Regarding Metals, Oxides, Chalcogenides, and Non-Metal Elements. *Green Chem.* **2015**, *17* (8), 4107–4132. https://doi.org/10.1039/c5gc00943j.
- (172) Hachani, R.; Lowdell, M.; Birchall, M.; Hervault, A.; Mertz, D.; Begin-Colin, S.; Thanh, N. T. B. D. K. Polyol Synthesis, Functionalisation, and Biocompatibility Studies of Superparamagnetic Iron Oxide Nanoparticles as Potential MRI Contrast Agents. *Nanoscale* 2016, 8 (6), 3278–3287. https://doi.org/10.1039/c5nr03867g.
- (173) Fu, S.; Yang, R.; Ren, J.; Liu, J.; Zhang, L.; Xu, Z.; Kang, Y.; Xue, P. Catalytically Active CoFe₂O₄ Nanoflowers for Augmented Sonodynamic and Chemodynamic Combination Therapy with Elicitation of Robust Immune Response. *ACS Nano* **2021**, *15* (7), 11953–11969. https://doi.org/10.1021/acsnano.1c03128.
- (174) Antonoglou, O.; Dendrinou-Samara, C. Polyols as a Toolbox for the Preparation of Inorganic-Based Nanostructures. In *Reducing Agents in Colloidal Nanoparticle*

- *Synthesis*; 2021; pp 51–72.
- (175) Thanh, N. T. K.; Maclean, N.; Mahiddine, S. Mechanisms of Nucleation and Growth of Nanoparticles in Solution. *Chem. Rev.* **2014**, *114* (15), 7610–7630. https://doi.org/10.1021/cr400544s.
- (176) García-Soriano, D.; Amaro, R.; Lafuente-Gómez, N.; Milán-Rois, P.; Somoza, Á.; Navío, C.; Herranz, F.; Gutiérrez, L.; Salas, G. The Influence of Cation Incorporation and Leaching in the Properties of Mn-Doped Nanoparticles for Biomedical Applications. *J. Colloid Interface Sci.* 2020, 578, 510–521. https://doi.org/10.1016/j.jcis.2020.06.011.
- (177) Mathew, D. S.; Juang, R. S. An Overview of the Structure and Magnetism of Spinel Ferrite Nanoparticles and Their Synthesis in Microemulsions. *Chem. Eng. J.* **2007**, *129* (1–3), 51–65. https://doi.org/10.1016/j.cej.2006.11.001.
- (178) Sharifi Dehsari, H.; Ksenofontov, V.; Möller, A.; Jakob, G.; Asadi, K. Determining Magnetite/Maghemite Composition and Core-Shell Nanostructure from Magnetization Curve for Iron Oxide Nanoparticles. *J. Phys. Chem. C* 2018, 122 (49), 28292–28301. https://doi.org/10.1021/acs.jpcc.8b06927.
- (179) Ahmed, S. A. Structural, Optical, and Magnetic Properties of Mn-Doped ZnO Samples. *Results Phys.* **2017**, 7, 604–610. https://doi.org/10.1016/j.rinp.2017.01.018.
- (180) Khanna, L.; Verma, N. K. PEG/CaFe₂O₄ Nanocomposite: Structural,

- Morphological, Magnetic and Thermal Analyses. *Phys. B Phys. Condens. Matter* **2013**, *427*, 68–75. https://doi.org/10.1016/j.physb.2013.05.040.
- (181) Branda, F.; Buri, A.; Marotta, A.; Saiello, S. Thermal Analysis and Catalytic Study of Transition Metals Acetylacetonates. *Thermochim. Acta* **1984**, *93*, 65–68.
- (182) Vamvakidis, K.; Sakellari, D.; Angelakeris, M.; Dendrinou-Samara, C. Size and Compositionally Controlled Manganese Ferrite Nanoparticles with Enhanced Magnetization. *J. nanoparticle Res.* **2013**, *15* (6), 1743–1753.
- (183) Ge, J.; Hu, Y.; Biasini, M.; Beyermann, W. P.; Yin, Y. Superparamagnetic Magnetite Colloidal Nanocrystal Clusters. *Angew. Chemie Int. Ed.* **2007**, *46* (23), 4342–4345. https://doi.org/10.1002/anie.200700197.
- (184) Gavilán, H.; Sánchez, E. H.; Brollo, M. E. F.; Asín, L.; Moerner, K. K.; Frandsen, C.; Lázaro, F. J.; Serna, C. J.; Veintemillas-Verdaguer, S.; Morales, M. P.; Gutiérrez, L. Formation Mechanism of Maghemite Nanoflowers Synthesized by a Polyol-Mediated Process. ACS Omega 2017, 2 (10), 7172–7184. https://doi.org/10.1021/acsomega.7b00975.
- (185) Xie, Yili, Chen Tian, Weiyi Chen, Can Wu, Zhangbin Liu, Ping Ning, Hong Deng, and Z. L. Substitution-Mediated Enhanced Adsorption of Low Concentration As(V) from Water by Mesoporous Mn_xFe_{3-x}O₄ Microsphere. *Environ. Sci. Nano* **2019**, *6* (5), 1406–1417.
- (186) Xuan, S.; Wang, F.; Wang, Y. J.; Yu, C.; Leung, K. C. Facile Synthesis of Size-

- Controllable Monodispersed Ferrite Nanospheres. *J. Mater. Chem.* **2010**, *20* (24), 5086–5094. https://doi.org/10.1039/c0jm00159g.
- (187) Miguel-Sancho, N.; Bomati-Miguel, O.; Roca, A. G.; Martinez, G.; Arruebo, M.; Santamaria, J. Synthesis of Magnetic Nanocrystals by Thermal Decomposition in Glycol Media: Effect of Process Variables and Mechanistic Study. *Ind. Eng. Chem. Res.* 2012, 51 (25), 8348–8357. https://doi.org/10.1021/ie3002974.
- (188) LaMer, V. K.; Dinegar, R. H. Theory, Production and Mechanism of Formation of Monodispersed Hydrosols. *South. Med. J.* **1922**, *15* (3), 242–249. https://doi.org/10.1097/00007611-192203000-00016.
- (189) Qureashi, A.; Pandith, A. H.; Bashir, A.; Manzoor, T.; Malik, L. A.; Sheikh, F. A. Citrate Coated Magnetite: A Complete Magneto Dielectric, Electrochemical and DFT Study for Detection and Removal of Heavy Metal Ions. *Surfaces and Interfaces* 2021, 23 (December 2020), 101004–101019. https://doi.org/10.1016/j.surfin.2021.101004.
- (190) Mourdikoudis, S.; Pallares, R. M.; Thanh, N. T. K. Characterization Techniques for Nanoparticles: Comparison and Complementarity upon Studying Nanoparticle Properties. *Nanoscale* 2018, 10 (27), 12871–12934. https://doi.org/10.1039/c8nr02278j.
- (191) Chakraborty, I.; Majumder, D.; Talukdar, S.; Roy, S.; Mandal, K. Surface Engineered Magneto Fluorescent MnFe₂O₄ Nanoparticles in the Realm of Biomedical Applications. *Surfaces and Interfaces* **2017**, 9 (April), 154–159.

- https://doi.org/10.1016/j.surfin.2017.09.005.
- (192) Wyrzykowski, D.; Chmurzyński, L. Thermodynamics of Citrate Complexation with Mn²⁺, Co²⁺, Ni²⁺ and Zn²⁺ Ions. *J. Therm. Anal. Calorim.* **2010**, *102* (1), 61–64. https://doi.org/10.1007/s10973-009-0523-4.
- (193) Matzapetakis, M.; Karligiano, N.; Bino, A.; Dakanali, M.; Raptopoulou, C. P.; Tangoulis, V.; Terzis, A.; Giapintzakis, J.; Salifoglou, A. Manganese Citrate Chemistry: Syntheses, Spectroscopic Studies, and Structural Characterizations of Novel Mononuclear, Water-Soluble Manganese Citrate Complexes. *Inorg. Chem.* 2000, 39 (18), 4044–4051. https://doi.org/10.1021/ic9912631.
- (194) Justi, M.; de Freitas, M. P.; Silla, J. M.; Nunes, C. A.; Silva, C. A. Molecular Structure Features and Fast Identification of Chemical Properties of Metal Carboxylate Complexes by FTIR and Partial Least Square Regression. *J. Mol. Struct.* 2021, 1237, 130405–130417. https://doi.org/10.1016/j.molstruc.2021.130405.
- (195) Al-ghouti, M. A.; Da, D. A. Guidelines for the Use and Interpretation of Adsorption Isotherm Models: A Review. *J. Hazard. Mater.* **2020**, *393* (January), 122383–122404. https://doi.org/10.1016/j.jhazmat.2020.122383.
- (196) Han, J.; Kim, M.; Ro, H. M. Factors Modifying the Structural Configuration of Oxyanions and Organic Acids Adsorbed on Iron (Hydr)Oxides in Soils. A Review. *Environ. Chem. Lett.* **2020**, *18* (3), 631–662. https://doi.org/10.1007/s10311-020-00964-4.

- (197) Fortune, W. B., Mellon, M. G. Determination of Iron with O-Phenanthroline. *Ind. Eng. Chem. Anal. Ed.* 1938, 10 (2), 60–64. https://doi.org/10.1021/ac50118a003.
- (198) Sanchez-Hachair, A.; Hofmann, A. Hexavalent Chromium Quantification in Solution: Comparing Direct UV–Visible Spectrometry with 1,5-Diphenylcarbazide Colorimetry. *Comptes Rendus Chim.* **2018**, *21* (9), 890–896. https://doi.org/10.1016/j.crci.2018.05.002.
- (199) Urone, P. F. Stability of Colorimetric Reagent for Chromium, s-Diphenylcarbazide, in Various Solvents. *Anal. Chem.* **1955**, 27 (8), 1354–1355.
- (200) Shard, A. G. Practical Guides for X-Ray Photoelectron Spectroscopy: Quantitative XPS. *J. Vac. Sci. Technol. A* **2020**, *38* (4), 041201. https://doi.org/10.1116/1.5141395.
- (201) Gao, W. G.; Liu, X. C.; Chen, M. F. In Situ ATR-FTIR Investigation and Theoretical Calculation of the Interactions of Chromate and Citrate on the Surface of Haematite (α-Fe₂O₃). *RSC Adv.* **2017**, 7 (65), 41011–41016. https://doi.org/10.1039/c7ra04587e.
- (202) Cantu, Y.; Remes, A.; Reyna, A.; Martinez, D.; Villarreal, J.; Ramos, H.; Trevino, S.; Tamez, C.; Martinez, A.; Eubanks, T.; Parsons, J. G. Thermodynamics, Kinetics, and Activation Energy Studies of the Sorption of Chromium(III) and Chromium(VI) to a Mn₃O₄ Nanomaterial. *Chem. Eng. J.* 2014, 254, 374–383. https://doi.org/10.1016/j.cej.2014.05.110.

- (203) Kumar, H.; Maurya, K. L.; Gehlaut, A. K.; Singh, D.; Maken, S.; Gaur, A.; Kamsonlian, S. Adsorptive Removal of Chromium(VI) from Aqueous Solution Using Binary Bio-Polymeric Beads Made from Bagasse. *Appl. Water Sci.* **2020**, *10* (1), 1–10. https://doi.org/10.1007/s13201-019-1101-y.
- (204) Li, Y.; Wei, G.; Zhang, C.; Liang, X.; Chu, W.; He, H.; Stucki, J. W.; Ma, L.; Lin, X.; Zhu, J. Remarkable Effect of Co Substitution in Magnetite on the Reduction Removal of Cr(VI) Coupled with Aqueous Fe(II): Improvement Mechanism and Cr Fate. Sci. Total Environ. 2019, 656, 400–408. https://doi.org/10.1016/j.scitotenv.2018.11.344.
- (205) Phu, N. D.; Ngo, D. T.; Hoang, L. H.; Luong, N. H.; Chau, N.; Hai, N. H. Crystallization Process and Magnetic Properties of Amorphous Iron Oxide Nanoparticles. *J. Phys. D. Appl. Phys.* **2011**, *44* (34), 1–7. https://doi.org/10.1088/0022-3727/44/34/345002.
- (206) Biesinger, M. C.; Payne, B. P.; Grosvenor, A. P.; Lau, L. W. M.; Gerson, A. R.; Smart, R. S. C. Resolving Surface Chemical States in XPS Analysis of First Row Transition Metals, Oxides and Hydroxides: Cr, Mn, Fe, Co and Ni. *Appl. Surf. Sci.* **2011**, 257 (7), 2717–2730. https://doi.org/10.1016/j.apsusc.2010.10.051.
- (207) Zhang, Z.; Wang, Y.; Tan, Q.; Zhong, Z.; Su, F. Facile Solvothermal Synthesis of Mesoporous Manganese Ferrite (MnFe₂O₄) Microspheres as Anode Materials for Lithium-Ion Batteries. *J. Colloid Interface Sci.* **2013**, *398*, 185–192. https://doi.org/10.1016/j.jcis.2013.01.067.

- (208) Desai, I.; Nadagouda, M. N.; Elovitz, M.; Mills, M.; Boulanger, B. Synthesis and Characterization of Magnetic Manganese Ferrites. *Mater. Sci. Energy Technol.* **2019**, *2* (2), 150–160. https://doi.org/10.1016/j.mset.2019.01.009.
- (209) Yamashita, T.; Hayes, P. Analysis of XPS Spectra of Fe²⁺ and Fe³⁺ Ions in Oxide Materials. *Appl. Surf. Sci.* **2008**, *254* (8), 2441–2449. https://doi.org/10.1016/j.apsusc.2007.09.063.
- (210) Chang, J.; Wang, H.; Zhang, J.; Xue, Q.; Chen, H. New Insight into Adsorption and Reduction of Hexavalent Chromium by Magnetite: Multi-Step Reaction Mechanism and Kinetic Model Developing. *Colloids Surfaces A Physicochem. Eng. Asp.* 2021, 611 (August 2020), 125784–125793. https://doi.org/10.1016/j.colsurfa.2020.125784.
- (211) Zhang, J.; Zhang, C.; Wei, G.; Li, Y.; Liang, X.; Chu, W.; He, H.; Huang, D.; Zhu, J.; Zhu, R. Reduction Removal of Hexavalent Chromium by Zinc-Substituted Magnetite Coupled with Aqueous Fe(II) at Neutral PH Value. *J. Colloid Interface Sci.* 2017, 500, 20–29. https://doi.org/10.1016/j.jcis.2017.03.103.
- (212) Li, N.; Li, W.; Fu, F. Removal of Chromium(VI) by MnFe₂O₄ and Ferrous Ion: Synergetic Effects and Reaction Mechanism. *Environ. Sci. Pollut. Res.* **2019**, 26 (29), 30498–30507. https://doi.org/10.1007/s11356-019-06261-0.
- (213) Xie, J.; Gu, X.; Tong, F.; Zhao, Y.; Tan, Y. Surface Complexation Modeling of Cr(VI) Adsorption at the Goethite-Water Interface. *J. Colloid Interface Sci.* **2015**, 455, 55–62. https://doi.org/10.1016/j.jcis.2015.05.041.

- (214) Thesai, A. sakthi; Sangeetha, R.; Ashokkumar, L.; Palanivelan, R.; Rajakumar, S.; Ayyasamy, P. M. Evaluation of Cr(VI) Reducing Capability of *Shewanella Putrefaciens* (MTTC8410) and Optimization of Operational Parameters. *J. Pure Appl. Microbiol.* **2020**, *14* (4), 2715–2727. https://doi.org/10.22207/JPAM.14.4.49.
- (215) Cheng, J.; Gao, J.; Zhang, J.; Yuan, W.; Yan, S.; Zhou, J.; Zhao, J.; Feng, S. Optimization of Hexavalent Chromium Biosorption by *Shewanella Putrefaciens*Using the Box-Behnken Design. *Water. Air. Soil Pollut.* **2021**, 232 (3), 1–14. https://doi.org/10.1007/s11270-020-04947-7.
- (216) Xu, L.; Chen, H.; Canales, M.; Ciric, L. Use of Synthesized Double-Stranded Gene Fragments as QPCR Standards for the Quantification of Antibiotic Resistance Genes. J. Microbiol. Methods 2019, 164 (July), 105670–105676. https://doi.org/10.1016/j.mimet.2019.105670.
- (217) Wurzler, N.; David, J.; Wagner, R.; Dimper, M.; Lützenkirchen-hecht, D.; Ozcan, O. Abundance of Fe(III) during Cultivation Affects the Microbiologically Influenced Corrosion (MIC) Behaviour of Iron Reducing Bacteria *Shewanella Putrefaciens*. Corros. Sci. 2020, 174 (February), 108855–108862. https://doi.org/10.1016/j.corsci.2020.108855.
- (218) Kees, E. D.; Levar, C. E.; Miller, S. P.; Bond, D. R.; Gralnick, J. A.; Dean, A. M. Survival of the First Rather than the Fittest in a *Shewanella* Electrode Biofilm. *Commun. Biol.* **2021**, *4* (4), 1–9. https://doi.org/10.1038/s42003-021-02040-1.

- (219) Bankier, C.; Cheong, Y.; Mahalingam, S.; Edirisinghe, M.; Ren, G.; Cloutman-Green, E.; Ciric, L. A Comparison of Methods to Assess the Antimicrobial Activity of Nanoparticle Combinations on Bacterial Cells. *PLoS One* **2018**, *13* (2), 1–13. https://doi.org/10.1371/journal.pone.0192093.
- (220) Becce, M.; Klöckner, A.; Higgins, S. G.; Penders, J.; Hachim, D.; Bashor, C. J.; Edwards, A. M.; Stevens, M. M. Assessing the Impact of Silicon Nanowires on Bacterial Transformation and Viability of *Escherichia Coli. J. Mater. Chem. B* **2021**, *9* (24), 4906–4914. https://doi.org/10.1039/d0tb02762f.
- (221) Adan, A.; Alizada, G.; Kiraz, Y.; Baran, Y.; Nalbant, A. Flow Cytometry: Basic Principles and Applications. *Crit. Rev. Biotechnol.* **2017**, *37* (2), 163–176. https://doi.org/10.3109/07388551.2015.1128876.
- (222) Wang, G.; Zhang, B.; Li, S.; Yang, M.; Yin, C. Simultaneous Microbial Reduction of Vanadium (V) and Chromium (VI) by *Shewanella Loihica* PV-4. *Bioresour*. *Technol.* **2017**, 227, 353–358. https://doi.org/10.1016/j.biortech.2016.12.070.
- (223) Newton, G. J.; Mori, S.; Nakamura, R.; Hashimoto, K.; Watanabe, K. Analyses of Current-Generating Mechanisms of *Shewanella Loihica* PV-4 and *Shewanella Oneidensis* MR-1 in Microbial Fuel Cells. *Appl. Environ. Microbiol.* **2009**, *75* (24), 7674–7681. https://doi.org/10.1128/AEM.01142-09.
- (224) Bennett, B. D.; Redford, K. E.; Gralnick, J. A.; Gralnick, A. Survival of Anaerobic Fe⁺² Stress Requires the ClpXP Protease. *J. Bacteriol.* **2018**, *200* (8), 1–14. https://doi.org/10.1128/JB.00671-17.

- (225) Chourey, K.; Thompson, M. R.; Morrell-Falvey, J.; VerBerkmoes, N. C.; Brown, S. D.; Shah, M.; Zhou, J.; Doktycz, M.; Hettich, R. L.; Thompson, D. K. Global Molecular and Morphological Effects of 24-Hour Chromium(VI) Exposure on *Shewanella Oneidensis* MR-1. *Appl. Environ. Microbiol.* 2006, 72 (9), 6331–6344. https://doi.org/10.1128/AEM.00813-06.
- (226) Kostka, J. E.; Nealson, K. H. Dissolution and Reduction of Magnetite by Bacteria.

 Environ. Sci. Technol. 1995, 29 (10), 2535–2540.

 https://doi.org/10.1021/es00010a012.
- (227) Myers, C. R.; Nealson, K. H. Bacterial Manganese Reduction and Growth with Manganese Oxide as the Sole Electron Acceptor. *Science* (80-.). **1988**, 240 (4857), 1319–1321. https://doi.org/10.1126/science.240.4857.1319.
- (228) Gunsolus, I. L.; Hang, M. N.; Hudson-Smith, N. V; Buchman, J. T.; Bennett, J. W.; Conroy, D.; Mason, S. E.; Hamers, R. J.; Haynes, C. L. Influence of Nickel Manganese Cobalt Oxide Nanoparticle Composition on Toxicity toward Shewanella Oneidensis MR-1: Redesigning for Reduced Biological Impact. Environ. Sci. Nano 2017, 4 (3), 636–646.
- (229) Szeinbaum, N.; Lin, H.; Brandes, J. A.; Taillefert, M.; Glass, J. B.; DiChristina, T. J. Microbial Manganese(III) Reduction Fuelled by Anaerobic Acetate Oxidation. *Environ. Microbiol.* 2017, 19 (9), 3475–3486. https://doi.org/10.1111/1462-2920.13829.
- (230) Szeinbaum, N.; Burns, J. L.; DiChristina, T. J. Electron Transport and Protein

- Secretion Pathways Involved in Mn(III) Reduction by *Shewanella Oneidensis*. *Environ. Microbiol. Rep.* **2014**, *6* (5), 490–500. https://doi.org/10.1111/1758-2229.12173.
- (231) Obraztsova, A.; Mackey, M. R.; Ellisman, M. H. Toxicity of Cr (III) to *Shewanella* Sp. Strain MR-4 during Cr (VI) Reduction. *Environ. Sci. Technol.* **2007**, *41* (1), 214–220.
- (232) Waldron, K. J.; Robinson, N. J. How Do Bacterial Cells Ensure That Metalloproteins Get the Correct Metal? *Nat. Rev. Microbiol.* **2009**, *7* (1), 25–35. https://doi.org/10.1038/nrmicro2057.
- (233) Irving J. P., H. and W.; Irving, H. and Williams, J. P. Order of Stability of Metal Complexes. *Nature* **1948**, *162*, 746–747.
- (234) Viamajala, S.; Peyton, B. M.; Sani, R. K.; Apel, W. A.; Petersen, J. N. Toxic Effects of Chromium(VI) on Anaerobic and Aerobic Growth of *Shewanella Oneidensis* MR-1. *Biocatal. Bioreact. Des.* **2004**, *20*, 87–95.
- (235) Elmeihy, R.; Shi, X. C.; Tremblay, P. L.; Zhang, T. Fast Removal of Toxic Hexavalent Chromium from an Aqueous Solution by High-Density *Geobacter Sulfurreducens*. *Chemosphere* **2021**, 263, 128281–128289. https://doi.org/10.1016/j.chemosphere.2020.128281.
- (236) Qin, J.; Qian, L.; Zhang, J.; Zheng, Y.; Shi, J.; Shen, J.; Ou, C. Accelerated Anaerobic Biodecolorization of Sulfonated Azo Dyes by Magnetite Nanoparticles

- as Potential Electron Transfer Mediators. *Chemosphere* **2021**, *263*, 128048–128057. https://doi.org/10.1016/j.chemosphere.2020.128048.
- (237) Glasauer, S.; Langley, S.; Beveridge, T. J. Sorption of Fe (Hydr)Oxides to the Surface of *Shewanella Putrefaciens*: Cell-Bound Fine-Grained Minerals Are Not Always Formed de Novo. *Appl. Environ. Microbiol.* **2001**, *67* (12), 5544–5550. https://doi.org/10.1128/AEM.67.12.5544-5550.2001.
- (238) Grantham, M. C.; Dove, P. M.; DiChristina, T. J. Microbially Catalyzed Dissolution of Iron and Aluminum Oxyhydroxide Mineral Surface Coatings. *Geochim. Cosmochim. Acta* **1997**, *61* (21), 4467–4477. https://doi.org/10.1016/S0016-7037(97)00265-2.
- (239) Zou, Dexun, Jingjing Tong, Chenyu Feng, Yang Wang, Xinxin Li, Xusheng Zheng, Xuebo Wang, and Y. L. Synthesis of Biochar@α-Fe₂O₃ Shewanella Loihica Complex for Remediation of Soil Contaminated by Hexavalent Chromium Optimization of Conditions and Mechanism. Chemosphere 2022, 134858–134868.
- (240) Yu, C.; Yu, L.; Mohamed, A.; Fang, J.; Wu, Y.; Dai, K.; Cai, P.; Huang, Q. Size-Dependent Visible-Light-Enhanced Cr(VI) Bioreduction by Hematite Nanoparticles. *Chemosphere* **2022**, 295 (October 2021), 133633–133643. https://doi.org/10.1016/j.chemosphere.2022.133633.
- (241) Ren, G.; Wang, X.; Huang, P.; Zhong, B.; Zhang, Z.; Yang, L.; Yang, X.

 Chromium (VI) Adsorption from Wastewater Using Porous Magnetite

 Nanoparticles Prepared from Titanium Residue by a Novel Solid-Phase Reduction

- Method. Sci. Total Environ. 2017, 607, 900–910.
- (242) Lemaire, O. N.; Vincent, M.; Iobbi-nivol, C. The *Shewanella* Genus: Ubiquitous Organisms Sustaining and Preserving Aquatic Ecosystems. *FEMS Microbiol. Rev.* **2020**, *44* (2), 155–170. https://doi.org/10.1093/femsre/fuz031.
- (243) Barer, M. R. *Bacterial Growth, Culturability and Viability*; Academic Press, 2014. https://doi.org/10.1016/B978-0-12-397169-2.00010-X.
- (244) Chowdhury, M.; Mostafa, M. G.; Biswas, T. K.; Mandal, A.; Saha, A. K. Characterization of the Effluents from Leather Processing Industries. *Environ. Process.* **2015**, 2 (1), 173–187. https://doi.org/10.1007/s40710-015-0065-7.
- (245) Lejri, R.; Ben Younes, S.; Ellafi, A.; Bouallegue, A.; Moussaoui, Y.; Chaieb, M.; Mekki, A. Physico-Chemical, Microbial and Toxicity Assessment of Industrial Effluents from the Southern Tunisian Tannery. J. Water Process Eng. 2022, 47 (February), 102686–102696. https://doi.org/10.1016/j.jwpe.2022.102686.
- (246) Bencheikh-Latmani, R.; Obraztsova, A.; Mackey, M. R.; Ellisman, M. H.; Tebo,
 B. M. Toxicity of Cr(III) to *Shewanella* Sp. Strain MR-4 during Cr(VI) Reduction. *Environ. Sci. Technol.* 2007, 41 (1), 214–220. https://doi.org/10.1021/es0622655.
- (247) Dichiara, A. B.; Weinstein, S. J.; Rogers, R. E. On the Choice of Batch or Fixed Bed Adsorption Processes for Wastewater Treatment. *Ind. Eng. Chem. Res.* **2015**, 54 (34), 8579–8586. https://doi.org/10.1021/acs.iecr.5b02350.

- (248) Vilardi, G.; Rodriguez-Rodriguez, J.; Miguel Ochando-Pulido, J.; Di Palma, L.; Verdone, N. Fixed-Bed Reactor Scale-up and Modelling for Cr(VI) Removal Using Nano Iron-Based Coated Biomass as Packing Material. *Chem. Eng. J.* **2019**, *361* (November 2018), 990–998. https://doi.org/10.1016/j.cej.2018.12.166.
- (249) Chatterjee, S.; Mondal, S.; De, S. Design and Scaling up of Fixed Bed Adsorption Columns for Lead Removal by Treated Laterite. *J. Clean. Prod.* **2018**, *177*, 760–774. https://doi.org/10.1016/j.jclepro.2017.12.249.
- (250) Díaz-Blancas, V.; Aguilar-Madera, C. G.; Flores-Cano, J. V.; Leyva-Ramos, R.; Padilla-Ortega, E.; Ocampo-Pérez, R. Evaluation of Mass Transfer Mechanisms Involved during the Adsorption of Metronidazole on Granular Activated Carbon in Fixed Bed Column. *J. Water Process Eng.* 2020, 36 (October 2019), 101303–101314. https://doi.org/10.1016/j.jwpe.2020.101303.
- (251) Belchik, S. M.; Kennedy, D. W.; Dohnalkova, A. C.; Wang, Y.; Sevinc, P. C.; Wu, H.; Lin, Y.; Lu, H. P.; Fredrickson, J. K.; Shi, L. Extracellular Reduction of Hexavalent Chromium by Cytochromes MtrC and OmcA of Shewanella Oneidensis MR-1. Appl. Environ. Microbiol. 2011, 77 (12), 4035–4041. https://doi.org/10.1128/AEM.02463-10.
- (252) Ma, H.; Guo, L.; Zhang, H.; Wang, Y.; Miao, Y.; Liu, X.; Peng, M.; Deng, X.; Peng, Y.; Fan, H. The Metal Ion Release of Manganese Ferrite Nanoparticles: Kinetics, Effects on Magnetic Resonance Relaxivities, and Toxicity. ACS Appl. Bio Mater. 2022, 5 (6), 3067–3074. https://doi.org/10.1021/acsabm.2c00338.

- (253) Uddin, M. J.; Jeong, Y. K.; Lee, W. Microbial Fuel Cells for Bioelectricity Generation through Reduction of Hexavalent Chromium in Wastewater: A Review. *Int. J. Hydrogen Energy* **2021**, *46* (20), 11458–11481. https://doi.org/10.1016/j.ijhydene.2020.06.134.
- (254) Rajput, V. D.; Minkina, T.; Kimber, R. L.; Singh, V. K.; Shende, S.; Behal, A.; Sushkova, S.; Mandzhieva, S.; Lloyd, J. R. Insights into the Biosynthesis of Nanoparticles by the Genus *Shewanella*. *Appl. Environ. Microbiol.* **2021**, 87 (22), e0139021. https://doi.org/10.1128/AEM.01390-21.
- (255) Byrne, J. M.; Coker, V. S.; Moise, S.; Wincott, P. L.; Vaughan, D. J.; Tuna, F.; Arenholz, E.; Van Der Laan, G.; Pattrick, R. A. D.; Lloyd, J. R.; Telling, N. D. Controlled Cobalt Doping in Biogenic Magnetite Nanoparticles. *J. R. Soc. Interface* 2013, 10 (83). https://doi.org/10.1098/rsif.2013.0134.
- (256) Coker, V. S.; van der Laan, G.; Telling, N. D.; Lloyd, J. R.; Byrne, J. M.; Arenholz,
 E.; Pattrick, R. A. D. Bacterial Production of Vanadium Ferrite Spinel (Fe, V)₃O₄
 Nanoparticles. *Mineral. Mag.* 2020, 84 (4), 554–562.
- (257) Mohammadinejad, R.; Shavandi, A.; Raie, D. S.; Sangeetha, J.; Soleimani, M.; Shokrian Hajibehzad, S.; Thangadurai, D.; Hospet, R.; Popoola, J. O.; Arzani, A.; Gómez-Lim, M. A.; Iravani, S.; Varma, R. S. Plant Molecular Farming: Production of Metallic Nanoparticles and Therapeutic Proteins Using Green Factories. *Green Chem.* 2019, 21 (8), 1845–1865. https://doi.org/10.1039/c9gc00335e.
- (258) Jadoun, S.; Chauhan, N. P. S.; Zarrintaj, P.; Barani, M.; Varma, R. S.; Chinnam,

- S.; Rahdar, A. Synthesis of Nanoparticles Using Microorganisms and Their Applications: A Review. *Environ. Chem. Lett.* **2022**, 20 (5), 3153–3197. https://doi.org/10.1007/s10311-022-01444-7.
- (259) Moon, J. W.; Yeary, L. W.; Rondinone, A. J.; Rawn, C. J.; Kirkham, M. J.; Roh, Y.; Love, L. J.; Phelps, T. J. Magnetic Response of Microbially Synthesized Transition Metal- and Lanthanide-Substituted Nano-Sized Magnetites. *J. Magn. Magn. Mater.* 2007, 313 (2), 283–292. https://doi.org/10.1016/j.jmmm.2007.01.011.
- (260) Blanco-Andujar, C.; Ortega, D.; Southern, P.; Pankhurst, Q. A.; Thanh, N. T. K. High Performance Multi-Core Iron Oxide Nanoparticles for Magnetic Hyperthermia: Microwave Synthesis, and the Role of Core-to-Core Interactions.

 Nanoscale 2015, 7 (5), 1768–1775. https://doi.org/10.1039/c4nr06239f.
- (261) Socoliuc, V.; Avdeev, M. V.; Kuncser, V.; Turcu, R.; Tombácz, E.; Vékás, L. Ferrofluids and Bio-Ferrofluids: Looking Back and Stepping Forward. *Nanoscale* **2022**, *14* (13), 4786–4886. https://doi.org/10.1039/d1nr05841j.